Recherche de nouvelle physique dans le canal B0s –> J/psi phi auprès de l'expérience LHCb

Basem Khanji

CPPM-T-2011-03

UNIVERSITÉ DE LA MÉDITERRANÉE AIX-MARSEILLE II
FACULTÉ DES SCIENCES DE LUMINY
163 avenue de Luminy
13288 MARSEILLE Cedex 09

THESE DE DOCTORAT

Spécialité : *Physique et Sciences de la Matière*

Mention : *Physique des Particules et Astroparticules*

présentée par

Basem KHANJI

en vue d'obtenir le grade de docteur de l'Université de la Méditerranée

Recherche de nouvelle physique dans le canal $B_s^0 \to J/\psi\phi$ auprès de l'expérience LHCb

soutenue le 16 septembre 2011 devant le jury composé de

Prof.	Joseph Boudreau	Rapporteur
Dr.	Michal Kreps	Rapporteur
Dr.	Eric Kajfasz	Président du jury
Dr.	Renaud Le Gac	Directeur de thèse
Dr.	Olivier Leroy	Directeur de thèse
Dr.	Patrick Koppenburg	Examinateur

Thanks

I am not very good at expressing emotions, but I will try for all of you my dear colleagues friends and brothers.

First, I would like to thank all my colleagues and friends at CPPM. Many thanks for our director, Eric Kajfasz, for his dedication and fine management. I spent wonderful years at CPPM and Marseille, it will warm my heart to come back here in the future.

Great thanks for Renaud Le Gac, my thesis supervisor. Thank you for welcoming me in your group. You gave the chance to "make" the physics I was reading about in Weinberg books when I was in Aleppo (my home city). Thanks for your encouragement and continuous help during the thesis. People with high caliber like Renaud can teach us a lot through small gestures.

Thanks to Olivier Leroy, my thesis supervisor and "encadrant". This thesis belongs to him as it belongs to me. Thank you for choosing this interesting and challenging subject. I learned a lot from your love for physics, your precision and your quest for perfection. During these years, we shared great moments together: we discovered the first B candidate at LHCb, the first $B_s^0 \to J/\psi\phi$ candidate at LHCb and made our contributions to the ϕ_s analysis at LHCb. Thank you for always motivating me through difficult times. I will miss our "bagarres" every Monday before the group meeting. By the way, great thanks for you and Julie for the nice dinner in your château bourgeois at the Roucas Blanc.

Many thanks for Stephane Poss for helping me at debugging my codes and explaining more about B physics and LHCb. stephane is a guy who "a le coeur dans la main". Thanks to you and to your mother Madame Caroline, I have today the nicest memories of the French countryside. I spent my first Christmas at her guest house "le pied de la falaise", and received from her my first Christmas gift. Thank you Caroline for your generous hospitality and exquisite French cuisine.

Thanks for Julien Cogan for his support and help in physics and programming. Great thanks to Arnaud Duperrin; my supervisor during my

"projet" at D0 for his kindness. Thanks for Emilie my first student (kidding!) and Cosme for their friendship and lovely times. I wish you both an excellent career. Thanks for Justine and Giampiero for their support and help.

Thanks for all members in LHCb collaboration, special thanks for the colleagues in β_s working group: Gaia, Marta, Tristan, Greig. Working with you in the ϕ_s measurement was an enriching experience.

Big thanks for my family, Mohssen my father and my friend. Fatima, the only source of pure love is the mother heart. Reem my beloved and hard working sister.

Thanks to: Abdo, Hassan, Firas, Moataz and Moustafa my brothers in aleppo. Thanks to Tammam, Bader, Hany and Wassim for the nice evenings at the "cité universitaire".

Aleppo, my home city and the bride of the silk way. Its cuisine is second to non. She still sleeps through oriental nights.

If Paris was a girl, I would have proposed to her!. Her beauty brings out the possessive child in me. Is she the women in Delacroix's painting?.

Syria, my country, is the Chapter one in the book of civilization. It is the land of saints and the cradle of the first alphabet.

Contents

Introduction

Le Modèle Standard est une théorie quantique des champs qui décrit les plus petits constituants de la matière ainsi que leurs interactions. Ce modèle a passé avec succès de nombreux tests expérimentaux au cours des 50 dernières années. Cependant, le modèle ne répond pas à certaines questions fondamentales telles que l'origine de la masse des particules et la différence de comportement entre les particules et anti-particules. Ces points, entre autres, laissent la porte ouverte à des processus au delà du Modèle Standard habituellement appelé la "Nouvelle Physique".

Les recherches directes de la Nouvelle Physique sont effectuées en tentant de créer de nouvelles particules à la frontière de l'énergie. La chasse du boson de Higgs est une exemple célèbre de ce type de recherche. Les recherches indirectes de la Nouvelle Physique exploitent la frontière de la luminosité. Les mesures des observables de la violation de la symmetrie CP appartiennent à ce second type de recherche.

L'expérience LHCb est situé à Genève auprès de l'accélérateur LHC et exploite l'approche indirecte. Elle est dédiée à la recherche de nouveaux phénomènes à travers des études de la violation de la symmetrie CP et des désintégrations rares dans les secteurs de la beauté et du charme.

Les désintégrations des mésons neutres B_d^0 et B_s^0 fournissent un ensemble d'observables de violaants CP dont les valeurs sont précisément prédites par le Modèle Standard. Dans le canal $B_s^0 \to J/\psi\phi$, l'interférence entre un B_s^0 se désintègrant dans l'état final, soit directement ou via l'oscillation B_s^0-$\overline{B}_s^0$ donne lieu à une phase appelée ϕ_s. Elle est l'une des observables violant CP où le Modèle Standard fait la prédiction la plus précise. De plus, la Nouvelle Physique peut modifier sensiblement cette prédiction, si des nouvelles particules entrent dans le diagramme en boucles decrivant l'oscillation B_s^0-$\overline{B}_s^0$.

Les étapes expérimentales de la mesure de ϕ_s en LHCb sont: le déclenchement et la sélection des événements $B_s^0 \to J/\psi\phi$, le calcul de leurs temps de vie propre et des variables angulaires, l'étiquetage de la saveur initiale du meson B_s^0 et, enfin, effectuer l'ajustement du taux de désinté-

grations différentielles aux données pour en extraire la phase ϕ_s. Des contraints sur ϕ_s ont été obtenus par CDF [1] et D0 [2]. Bien qu'en accords avec le Modèle Standard, la taille des incertitudes laisse beacoup de place à de potentielles contributions de Nouvelle Physique.

Avec l'arrivée de la première collision proton-proton au LHC en 2009, une nouvelle ère de la physique des particules a commencé. L'année 2010 a apporté les premières collisions à 7 TeV, et consacré le LHC comme le collisionneur hadronique le plus puissant dans le monde. La collaboration LHCb à prèsente sa première détermination de la phase ϕ_s en Avril 2010.

Après l'introduction des aspects théoriques du canal $B_s^0 \to J/\psi\phi$ dans le chapitre 1, le détecteur LHCb et ses performances sont décrites dans le chapitre 2. Dans le chapitre 3, nous présentons la sélection des événements $B_s^0 \to J/\psi\phi$. Cette sélection est conçue pour éviter les déformations de la distribution de temps propre au détriment de l'incertitude statistique. Nous décrivons les coupures de sélection et effectuons une étude détaillée des propriétés du signal et des bruits du fond avec une simulation Mont-Carlo. Les résultats de la sélection avec les données le 2010 sont donnés à la fin de ce chapitre. Nous développons également une sélection alternative qui vise à accroître la sensibilité statistique sur ϕ_s en autorisant des coupures qui biaise la distribution en temps propre.

Dans le chapitre 4, nous présentons la procédure d'étiquetage des saveurs dans LHCb et nous détaillons deux de nos contributions: la portabilité du taux de mauvais étiquetage à partir des canaux de contrôle $B^+ \to J/\psi K^+$ et $B_d^0 \to J/\psi K^{*0}$ au canal $B_s^0 \to J/\psi\phi$, et l'étude des performances d'étiquetage avec un taux élevés d'empilement proton-proton.

Le chapitre 5 contient nos études sur la sensibilité du détecteur LHCb à la phase ϕ_s en utilisant les sélections développées dans le chapitre 3. Les tests de notre programme d'ajustement sont effectues à l'aide des simulations Monte-Carle rapide et complète. Le comportement de l'ajustement en fonction de la luminosité intégrée est exploré. La première détermination de la phase ϕ_s effectuées sur la données de 2010 prèsenté ainsi qu'une discussion sur les sources d'incertitudes systématiques. Enfin, nous donnons les perspectives de la mesure de ϕ_s dans LHCb dans les années à venir.

Introduction

The Standard Model is a quantum field theory that describes the smallest constituents of the matter and the interactions amongst them. This model successfully passed many experimental tests to which it was subjected during the last 50 years. However, the model does not answer some fundamental questions such as the origin of the mass of the particles and the different behavior between particles and anti-particles. These points, among others, leave the door open to processes beyond the Standard Model usually called New Physics.

Direct search for New Physics is performed by looking for new particles at the energy frontier. The Higgs particle is a famous example of this search. Indirect searches for New Physics exploits the luminosity frontier, typically CP violation and rare decays measurements belong to this type. The LHCb experiment is located in Geneva at the LHC accelerator and exploits the indirect approach. It is dedicated to the search of new phenomena in CP violation and rare decays in the beauty and charm sectors.

B_d^0 and B_s^0 neutral mesons decays provide a set of CP violation observables whose values are precisely predicted in the Standard Model. In the $B_s^0 \to J/\psi\phi$ channel, the interference between B_s^0 decays to the final states either directly or via B_s^0-$\overline{B}_s^0$ oscillation gives rise to a CP violating phase called ϕ_s. It is one of the CP observables where the Standard Model makes the most precise prediction. In addition, New Physics can significantly modify this prediction if new particles enter the B_s^0-$\overline{B}_s^0$ loop diagram.

Experimental steps of the ϕ_s analysis at LHCb are: triggering and selection of $B_s^0 \to J/\psi\phi$ events, calculation of proper time decay and the angular variables, tagging the initial flavor of the B_s^0 meson, and finally performing the fit of the theoretical decay rate to the data to extract the phase ϕ_s. Constrints on ϕ_s have been obtained by CDF [1] and D0 [2]. They do not exibit any disagreement with the Standard Model.

With the advent of the first proton-proton collision at the LHC in 2009, a new era of the particle physics begins. The year 2010 brought the first collisions at 7 TeV, earning the new LHC collider the distinction of being

the most powerful hadron collider in the world. The LHCb collaboration provided the first determination of the ϕ_s phase at LHCb.

After the introduction of the theoretical aspects of the the $B_s^0 \to J/\psi\phi$ channel in Chapter 1, the LHCb detector and its performance are described in Chapter 2. In Chapter 3 we present the selection of $B_s^0 \to J/\psi\phi$ events. Which is designed to avoid sculpting of the proper time distributions at the expense of statistical uncertainty. We describe the selection cuts and perform a detailed study of the signal and background properties using the most recent Monte Carlo samples. Results of the selection with 2010 data are given at the end of this chapter. We also develop an alternative selection that focuses on increasing the statistical sensitivity in ϕ_s while allowing cuts which bias proper time distribution.

In Chapter 4, We present the flavour tagging procedure in LHCb and detail two of our contributions: the portability of the mistag rate from the control channels $B^+ \to J/\psi K^+$ and $B_d^0 \to J/\psi K^{*0}$ to the $B_s^0 \to J/\psi\phi$ channel, and the tagging performance study with high proton-proton pile-up.

Chapter 5 contains our studies about the sensitivity of the LHCb detector to the ϕ_s phase using the selections developed in Chapter 3. Tests of our fitter program are provided using fast and full Monte Carlo simulations. The behavior of the likelihood fit as a function of integrated luminosity is explored. The first determination of the ϕ_s phase performed on the 2010 data is given, with a discussion on sources of systematic uncertainties. We close this work with a review of the prospects of the ϕ_s measurement at LHCb in the coming years.

Chapter 1

Theory

This Chapter presents the theoretical framework of this thesis.It introduces CP violation in the Standard Model, the formalism of the $B_s^0 - \overline{B}_s^0$ mixing and decay, as well as a detailed description of the $B_s^0 \to J/\psi\phi$ differential decay rates. The Standard Model describes the elementary particles and their interactions. Its predictions were found to be compatible with experimental data. However, the model leaves essential questions unanswered, one of which is the origin of the matter-antimatter imbalance in the univers. CP violation plays an important role in the latter puzzle.

CP violation phenomena arises from in the electro-weak sector of the Standard Model. Decays of B mesons provide a set of clean measurements sensitive to CP violation. Studying these decays puts the Standard Model predictions to the test and could reveal evidence of indirect New Physics contributions.

In Section 1.1 we define the C, P and CP symmetries in quantum mechanics, and explain on the historical advent of the discovery of CP violation. Section 1.2 presents CP violation within the Standard Model. The $B_s^0 - \overline{B}_s^0$ mixing formalism is described in Section 1.3. The rates governing the decay of the neutral B_s^0 are developed in Section 1.4 where we also develop an equation for the asymmetry arising from different types of CP. Section 1.5 is divided into two subsections. In Subsection 1.5.1, we describe the phenomenology of the $B_s^0 \to J/\psi\phi$ and its phase ϕ_s in Standard Model and New Physics Models. In Subsection 1.5.2, we write in detail the differential decay rates for the $B_s^0 \to J/\psi\phi$ channel using the angular analysis method. In Section 1.6 we show the experimental state of the art of the ϕ_s measurement at CDF an D0. Finally in Section 1.7 we outline the of strategy adopted at LHCb to perform the ϕ_s measurement in the $B_s^0 \to J/\psi\phi$ channel.

CP violation subject is treated in many books. We use [3] and [4] as main references for this Chapter. We use the LHCb notations and conventions [5] throughout the thesis.

1.1 Symmetries and CP violation

Charge symmetry is related to the invariance of physical laws under the charge conjugation operator $\mathcal{C}$. The $\mathcal{C}$ operator conjugates all internal quantum numbers (for example it reverses the electromagnetic charge) leaving quantities like energy momentum and the spin intact. The mathematical definition of this operator is:

$$\mathcal{C}|\psi(\vec{p},h)\rangle = \eta_{\mathcal{C}}|\overline{\psi}(\vec{p},h)\rangle, \tag{1.1}$$

where $|\psi(\vec{p},h)\rangle$ is the quantum state of a given system with momentum $\vec{p}$ and helicity h, $\eta_{\mathcal{C}}$ is the eigenvalue of the $\mathcal{C}$ operator.

Parity symmetry is related to an invariance of physics laws under a transformation that changes the sign of the space coordinates x, y and z. Mathematically it is defined as:

$$\mathcal{P}|\psi(\vec{p},h)\rangle = \eta_{\mathcal{P}}|\psi(-\vec{p},-h)\rangle, \tag{1.2}$$

where $\eta_{\mathcal{P}}$ is the eigenvalue of the $\mathcal{P}$ operator. Under parity transformation, the spatial coordinates of the particles are reversed.

The product of the operators $\mathcal{C}$ and $\mathcal{P}$ transforms the quantum state as follows:

$$\mathcal{CP}|\psi(\vec{p},h)\rangle = \eta_{\mathcal{CP}}|\overline{\psi}(-\vec{p},-h)\rangle, \tag{1.3}$$

where $\eta_{\mathcal{CP}}$ is the eigenvalue of the operator $\mathcal{CP}$. Under CP transformation, a left-handed electron e^-_L is transformed under CP into right-handed positron e^+_R. CP symmetry postulates that particle and its antiparticles experiance the same law of physics, meaning that nature does not discriminate between the two components. CP *violation* means that the laws of physics are seen differently by particles and their own anti-particles, i.e., nature can distinguish a particles from ite antiparticles. CP violation is of great importance for our understanding of the universe. It was believed first that C, P, and CP were exact symmetries, but in 1957 Wu [7] showed that the weak interaction violates the P symmetry, by observing that the β decay for the ^{60}CO nuclei produced electrons preferentially aligned to the direction of nuclear spin. Later on 1964, it was found [8] that the CP symmetry is violated in the neutral kaon system. Kobayashi and Maskawa, in 1973, proposed a mechanism [9] which could accounts for CP violation

within the Standard Model. This mechanism extends the Cabbibo [10] and GIM [11] rotating quark matrix to include a new quark generation, and postulate that this matrix have a complex element that accommodates the CP violation. In 2000 The BaBar [13] and Belle [14] experiments observed the CP violation in the weak decays of B_d^0 neutral mesons. In 2008 Kobayashi and Maskawa received Nobel prize for their work. Since the CKM proposition, experimental efforts in the CP violation sector focuses on testing the self-consistency of the CKM matrix, in addition to measuring its elements or quantities related to them. In the following section, we will present how the CP violation arises in the Standard Model and discuss the CKM matrix.

1.2 CP violation in Standard Model

The Standard Model of particles is a quantum field theory. It describes the fundamental interactions of elementary particles (quarks and leptons) via intermediates called gauge bosons (γ, Z, $W^{\pm}$ and g). Those interactions are the electromagnetic, strong and the weak interactions. The interactions are governed by local gauge invariance, with gauge group $SU(3) \times SU(2)_L \times U(1)_Y$.

One term of the Standard Model Langrangian is relevant for CP violation; it is called Yukawa Langrangian. It describes the interaction between fermions and a scalar field called Higgs. The Yukawa couplings between this field and the fermions give these particles their masses. Due to the fact that this Higgs field has a non-zero vacuum expectation value, Yukawa couplings g give rise to 3×3 mass matrix: $M_i = v g_i / \sqrt{2}$. Where $i = u(d)$ for up(down) -type quarks. The Lagrangian density of the electroweak interaction is based on the gauge symmetry group $SU(2)_L \times U(1)_Y$. The term describing the interaction between the gauge boson and the fermion can be written:

$$\mathcal{L}^{EM} + \mathcal{L}^{NC} + \mathcal{L}^{CC} \tag{1.4}$$

The three terms are respectively designated the electromagnetic interaction, interaction by neutral current and the interaction mediated by the $W^{\pm}$ boson, called the charged current interaction. The electroweak interaction is based on the gauge group $SU_L(2)$. Consequently, only left handed particles couple to $\mathbf{W}^{\pm}$. To move from the mass basis to the electroweak basis, also called flavor basis, one should diagonalize the mass matrix M_i. The latter process only affect the non-leptonic charged-current interaction

Lagrangian:

$$\mathcal{L}_{\text{int}}^{W^{\pm}} = -\frac{g}{\sqrt{2}}(\overline{u}_L, \overline{c}_L, \overline{t}_L)\gamma^{\mu} V_{CKM} \begin{pmatrix} d_L \\ s_L \\ b_L \end{pmatrix} \mathbf{W}^{+} + h.c \tag{1.5}$$

where g is the gauge coupling, $\mathbf{W}^{+}$ is the scalar field corresponds to the intermediate W boson, L is the suffix of Left-handed quarks, V_{CKM} is the Cabbibo-Kobayashi-Maskawa rotation matrix:

$$\begin{pmatrix} \mathrm{d} \\ \mathrm{s} \\ \mathrm{b} \end{pmatrix}^{\text{flavour}} = \begin{pmatrix} V_{ud} & V_{us} & V_{ub} \\ V_{cd} & V_{cs} & V_{cb} \\ V_{td} & V_{ts} & V_{tb} \end{pmatrix} \begin{pmatrix} \mathrm{d} \\ \mathrm{s} \\ \mathrm{b} \end{pmatrix}^{\text{mass}} \tag{1.6}$$

where the elements V_{ij} of this matrix are proportional to coupling strength in transition between the quarks i, j. The condition for the CKM matrix to have a non-zero CP violation is formulated as:

$$J \equiv \mathfrak{Im}(V_{i\alpha} V_{j\beta} V_{j\alpha}^{*} V_{i\beta}^{*}) \neq 0\,, \tag{1.7}$$

where J is the Jarlskog invariant [15, 16]. The J represents the strength of the CP violation in the Standard Model. The value of J is small [17]: $\mathcal{O}(10^{-5})$. This implies that CP violating effects in the Standard Model are small.

The CKM matrix is unitary $V_{CKM}^{\dagger} V_{CKM} = 1$; its elements are complex numbers. The orthogonality of columns (or rows) of the unitary CKM matrix imply:

$$\begin{aligned}
V_{\mathrm{ud}} V_{\mathrm{us}}^{*} + V_{\mathrm{cd}} V_{\mathrm{cs}}^{*} + V_{\mathrm{td}} V_{\mathrm{ts}}^{*} &= 0 \\
V_{\mathrm{ud}} V_{\mathrm{ub}}^{*} + V_{\mathrm{cd}} V_{\mathrm{cb}}^{*} + V_{\mathrm{td}} V_{\mathrm{tb}}^{*} &= 0 \qquad (1.8) \\
V_{\mathrm{us}} V_{\mathrm{ub}}^{*} + V_{\mathrm{cs}} V_{\mathrm{cb}}^{*} + V_{\mathrm{ts}} V_{\mathrm{tb}}^{*} &= 0 \qquad (1.9) \\
V_{\mathrm{ud}} V_{\mathrm{cd}}^{*} + V_{\mathrm{us}} V_{\mathrm{cs}}^{*} + V_{\mathrm{ub}} V_{\mathrm{cb}}^{*} &= 0 \\
V_{\mathrm{ud}} V_{\mathrm{td}}^{*} + V_{\mathrm{us}} V_{\mathrm{ts}}^{*} + V_{\mathrm{ub}} V_{\mathrm{tb}}^{*} &= 0 \\
V_{\mathrm{cd}} V_{\mathrm{td}}^{*} + V_{\mathrm{cs}} V_{\mathrm{ts}}^{*} + V_{\mathrm{cb}} V_{\mathrm{tb}}^{*} &= 0
\end{aligned}$$

We can represent the first six equations as triangles in the complex plane, for example, b−s triangles is presented in Figure 1.2

A useful parameterization of the CKM matrix was suggested by Wolfenstein [18]. Four real parameters A, λ, ρ and η are used in the parameterization, the expansion parameter is $\lambda = sin(\theta_c)$, where θ_c is the Cabbibo angle [10]:

$$V_{\mathrm{CKM}} = \begin{pmatrix} 1 - \lambda^2/2 & \lambda & A\lambda^3(\rho - i\eta) \\ -\lambda & 1 - \lambda^2/2 & A\lambda^2 \\ A\lambda^3(1 - \rho - i\eta) & -A\lambda^2 & 1 \end{pmatrix} + \mathcal{O}(\lambda^4). \tag{1.10}$$

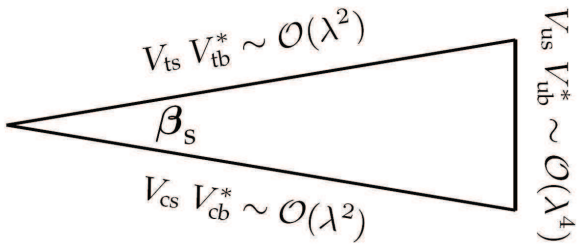

Figure 1.1: The b−s unitarity triangle, corresponding to the relation 1.9. where λ is the sine of the Cabbibo angle.

This parameterization reflects the fact that the off-diagonal transitions (e.g. $t \to d$) are *suppressed* compared to the diagonal ones (e.g. $c \to s$). Unitarity of this parameterization is assured to the $\mathcal{O}(\lambda^4)$. One can define the angle β_s to be the (positive) smallest angle of the b−s unitarity triangle, corresponding to:

$$\beta_s = \arg\left(-\frac{V_{ts}V_{tb}^{*}}{V_{cs}V_{cb}^{*}}\right). \tag{1.11}$$

This phase is a physical quantity. Using Wolfenstien parameterization, the angle β_s can as:

$$\beta_s = \eta\lambda^2 + \mathcal{O}(\lambda^4) \tag{1.12}$$

The fit of the CKM parameters on experimental data provide the following value [17] for this parameter:

$$\beta_s = 0.01818^{+0.00087}_{-0.00083}\,\text{rad}.$$

The precision on this prediction is at the level of $\sim$ 5%. This makes β_s one of the best known CP observables. In addition, this phase appears in $\bar{b} \to \bar{c}c\bar{s}$ transition in the B_s^0 decays where loop process is involved. For those two reasons this phase is considered a powerful probe for New Physics in the CP violating sector.

CKM matrix elements are related to physical obsrvables. Those can be measured in various experiments. A global fit to the experimental measurements of CKM elements provide a valuable test for the Standard Model predictions.

The current status of CKM fit of the Standard Model is presented in the

$\bar{\rho} - \bar{\eta}$ plane in Figure 1.2., where:

$$\bar{\rho} = \rho \left(1 - \frac{1}{2}\lambda^2\right) \tag{1.13}$$

$$\bar{\eta} = \eta \left(1 - \frac{1}{2}\lambda^2\right) \tag{1.14}$$

The parameters $\bar{\rho}$ and $\bar{\eta}$ are determined using the measurements of sides

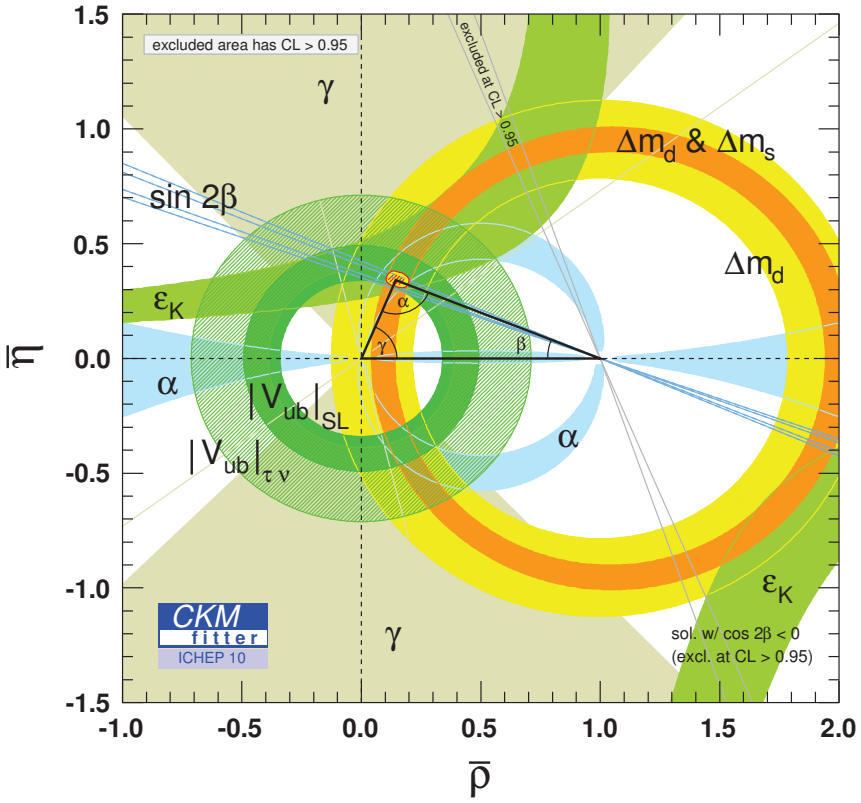

Figure 1.2: Constrains on the CKM $(\bar{\rho}, \bar{\eta})$ coordinates from global Standard Model CKM-fit [22]. Regions outside colored areas have CL$>$ 95.45%. For the combined fit the yellow area represents points with CL$<$ 95.45%, the shaded areas represent points with CL$<$ 68.3%

and the angles of the unitarity triangle 1.8. The left side of the triangle is determined by the oscillation frequencies Δm_d and Δm_s, the right side is

determined by the measurement of $|V_{ub}/V_{uc}|$ which is limited by the theoretical extraction of V_{ub} from inclusive and exclusive semi-leptonic channels. As for the angles: α is extracted from the modes $B_d^0 \to \pi^+\pi^-$ or $B_d^0 \to \rho\pi$ and $B_d^0 \to \rho\rho$. The angle β is extracted from time-dependent CP asymmetry the $\bar{b} \to \bar{c}c\bar{s}$ transitions of the B^0 meson. Finally the angle γ is measured in B→Dπ and B→D K decays.

An overall agreement is observed between the Standard Model fit prediction of the parameters and their experimental values. However, a 2.9σ deviation of the measurement of the $\mathcal{B}(B \to \tau\nu)$ from its prediction in the Standard Model fit is spotted. This could be a sign of New Physics in $\sin 2\beta$ or/and $\mathcal{B}(B \to \tau\nu)$ [22].

1.3 Neutral B_s^0 mesons mixing

In this Section, we introduce the oscillation phenomenon between B_s^0 and $\overline{B}_s^0$ along with its formalism within quantum mechanics. In the Standard Model, B_s^0 mesons oscillate, at the lowest order, through box diagrams represented in Figure 1.3. Our convention is the following: Flavour eigenstates $|B_s^0\rangle$ and $|\overline{B}_s^0\rangle$ are associated with the particles $B_s^0 \sim \bar{b}s$ and $\overline{B}_s^0 \sim b\bar{s}$. B_s^0 mesons are created by the hadronization of the b quark. The electroweak interaction does not conserve the beauty quantum number. This causes the B meson to decay through a phenomena where a transition between the $|B_s^0\rangle(|\overline{B}_s^0\rangle)$ into $|\overline{B}_s^0\rangle(|B_s^0\rangle)$ can take place; this phenomena is called "the mixing". The flavour states $|B_s^0\rangle$ and $|\overline{B}_s^0\rangle$ are related when introduc-

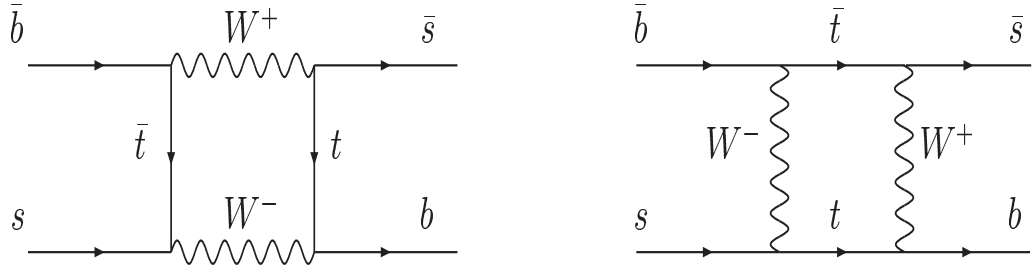

Figure 1.3: Feynman diagrams responsible for B_s^0–$\overline{B}_s^0$ mixing, within the Standard Model.

ing the CP transformation:

$$\mathcal{CP}|B_s^0\rangle = e^{-i\xi_{cp}}|\overline{B}_s^0\rangle,\ \mathcal{CP}|\overline{B}_s^0\rangle = e^{-i\xi_{cp}}|B_s^0\rangle \tag{1.15}$$

where ξ_{cp} is an arbitrary phase. In the framework of quantum mechanics, the B_s^0-$\overline{B}_s^0$ system is described by a linear combination of its flavour eigenstates:

$$a|B_s^0\rangle + b|\overline{B}_s^0\rangle, \tag{1.16}$$

this combination has a time evolution described by an effective Schrödinger equation:

$$i\frac{\partial}{\partial t}\begin{pmatrix} a(t) \\ b(t) \end{pmatrix} = \mathcal{H}\begin{pmatrix} a(t) \\ b(t) \end{pmatrix}, \tag{1.17}$$

where $\mathcal{H}$ is the effective Hamiltonian describing the system. Using the Wissekopf-Wigner [19] approximation, this Hamiltonian can be written as the sum of two matrices:

$$\mathcal{H} = \mathbf{M} - i\frac{\mathbf{\Gamma}}{2} = \begin{pmatrix} M_{11} & M_{12} \\ M_{21}^* & M_{22} \end{pmatrix} - \frac{i}{2}\begin{pmatrix} \Gamma_{11} & \Gamma_{12} \\ \Gamma_{21}^* & \Gamma_{22} \end{pmatrix}, \tag{1.18}$$

where $\mathbf{M}$ and $\mathbf{\Gamma}$ are 2×2 Hermitian matrices. The sum of the two matrices is not Hermitian, otherwise the two-meson system would not decay. Diagonal element of $\mathbf{M}$ and $\mathbf{\Gamma}$ are associated with flavor conserving transitions: $B_s^0 \to B_s^0$, off diagonal elements of $\mathbf{M}$ and $\mathbf{\Gamma}$ are associated with flavor changing transitions: $B_s^0 \to \overline{B}_s^0$. Hermiticity of the $\mathbf{M}$ and $\mathbf{\Gamma}$ matrices implies that their off-diagonal elements are related: $M_{21}^* = M_{12}$, $\Gamma_{21}^* = \Gamma_{12}$. Due to the CPT theorem [20], their diagonal elements are equal: $M_{11} = M_{22} = M_s$ and $\Gamma_{11} = \Gamma_{22} = \Gamma_s$, this represents the fact that both B_s^0 and $\overline{B}_s^0$ have the same lifetime and mass. The eigenstates of the Hamiltonian are:

$$|B_L\rangle = p|B_s^0\rangle + q|\overline{B}_s^0\rangle, \tag{1.19}$$

$$|B_H\rangle = p|B_s^0\rangle - q|\overline{B}_s^0\rangle. \tag{1.20}$$

those are called the mass eigenstate. They are designated by "heavy" (H) and "light" (L), The complex coefficients p and q obey the normalization condition:

$$|p|^2 + |q|^2 = 1. \tag{1.21}$$

The corresponding eigenvalues are:

$$\lambda_{L,H} = (M_s - \frac{i}{2}\Gamma_s) \pm \frac{q}{p}(M_{12} - \frac{i}{2}\Gamma_{12}) \tag{1.22}$$

with:

$$\left(\frac{p}{q}\right)^2 = \frac{M_{21}^* - \Gamma_{21}^*}{M_{21} - \Gamma_{21}}. \tag{1.23}$$

The general solutions that describes pure B_s^0 or pure $\overline{B}_s^0$ flavour-oscillation at time t:

$$|B_s^0\rangle(t) = g_+(t)|B_s^0\rangle + \frac{q}{p}g_-(t)|\overline{B}_s^0\rangle, \tag{1.24}$$

$$|\overline{B}_s^0\rangle(t) = g_+(t)|\overline{B}_s^0\rangle + \frac{q}{p}g_-(t)|B_s^0\rangle, \tag{1.25}$$

with

$$g_\pm(t) = \frac{1}{2}\left(e^{-i\lambda_L} \pm e^{-i\lambda_H}\right), \tag{1.26}$$

$$|g_\pm(t)|^2 = \frac{1}{2}e^{-\Gamma_s t}\left(\cosh(\frac{\Delta\Gamma_s t}{2}) \pm \cos(\Delta m_s t)\right). \tag{1.27}$$

The off diagonal elements M_{12} and Γ_{12} are the dispersive and the absorptive parts of the transition amplitude of $B_s^0 \to \overline{B}_s^0$. The mass difference, Δm_s and the width difference, $\Delta\Gamma_s$, between the mass eigenstates B_L and B_H are defined by:

$$\Delta m_s = M_H - M_L \ , \ \Delta\Gamma_s = \Gamma_L - \Gamma_H, \tag{1.28}$$

$$M_{B_s^0} = \frac{M_H + M_L}{2} \ , \ \Gamma_s = \frac{\Gamma_L + \Gamma_H}{2}. \tag{1.29}$$

where the M_H, M_L and Γ_H, Γ_L are the mass and decay width for the $|B_L\rangle$ and $|B_H\rangle$respectively. By solving the eigenvalues Equation 1.22, we get:

$$(\Delta m_s)^2 - \frac{1}{4}(\Delta\Gamma_s)^2 = 4|M_{12}|^2 - |\Gamma_{12}|^2, \ \Delta m_s\Delta\Gamma_s = 4\mathfrak{Re}(M_{12}^*\Gamma_{12}^*) \tag{1.30}$$

The calculation of the absorptive part [21] of the $B_s^0 - \overline{B}_s^0$ mixing diagram, Figure 1.3, gives the following constraint:

$$\frac{\Gamma_{12}}{M_{12}} \sim \mathcal{O}(\frac{m_b^2}{m_t^2}) << 1. \tag{1.31}$$

then we can write:

$$\Delta m_s = 2|M_{12}|, \ \Delta\Gamma_s = 2|\Gamma_{12}|\cos(\phi_{M/\Gamma}), \ \phi_{M/\Gamma} = arg(-\frac{M_{12}^s}{\Gamma_{12}^s}). \tag{1.32}$$

$\phi_{M/\Gamma}$ is the phase difference between M_{12} and Γ_{12}. In the Standard Model, $\phi_{s,SM}^{M/\Gamma} = (7.4^{+0.8}_{-3.2}) \times 10^{-3}$ rad [22]. Δm_s, $\Delta\Gamma_s$ and $\phi_{M/\Gamma}$ are the mixing parameters. These are related to the CP asymmetry in flavour-specific decays a_{fs}:

$$a_{fs} = Im\frac{\Gamma_{12}}{M_{12}} = \frac{\Delta\Gamma_s}{\Delta m_s}\tan\phi_{M/\Gamma}. \tag{1.33}$$

The semi-leptonic decays are ideal to extract this quantity. Within the Standard Model the CP violation in the B_s^0 mixing system is expected to be small: $a_{fs} = (1.9 \pm 0.3)10^{-5}$.

1.4 Neutral B_s^0 mesons decays

In this section we tackle the question of B_s^0-$\overline{B}_s^0$ system decaying into a final state f, we extract the general equations for these decay rates. The amplitudes of the instantaneous B_s^0-$\overline{B}_s^0$ decay to a final state f are defined as:

$$A_f = \langle f|\mathcal{H}|B_s^0\rangle, \quad \overline{A}_{\overline{f}} = \langle \overline{f}|\mathcal{H}|\overline{B}_s^0\rangle, \tag{1.34}$$

$$A_{\overline{f}} = \langle \overline{f}|\mathcal{H}|B_s^0\rangle, \quad \overline{A}_f = \langle f|\mathcal{H}|\overline{B}_s^0\rangle. \tag{1.35}$$

The decay rates of B_s^0 or $\overline{B}_s^0$ to a final state f or its CP conjugate $\overline{f}$, as a function of its proper time t, can be written:

$$\Gamma(B_s^0(t) \to f) = |A_f|^2\Big[|g_+(t)|^2 + |\lambda_f|^2|g_-(t)|^2 + 2\mathfrak{Re}\{\lambda_f g_-^*(t)g_-(t)\}\Big], \tag{1.36}$$

$$\Gamma(B_s^0(t) \to \overline{f}) = |\overline{A}_{\overline{f}}|^2\Big|\frac{q}{p}\Big|^2\Big[|g_-(t)|^2 + \Big|\frac{1}{\lambda_{\overline{f}}}\Big|^2|g_+(t)|^2 + \mathfrak{Re}[\frac{1}{\lambda_{\overline{f}}}g_+(t)g_-^*(t)]\Big], \tag{1.37}$$

$$\Gamma(\overline{B}_s^0(t) \to f) = |A_f|^2\Big|\frac{p}{q}\Big|^2\Big[|g_-(t)|^2 + |\lambda_f|^2|g_+(t)|^2 + 2\mathfrak{Re}\{\lambda_f g_+(t)g_-^*(t)\}\Big], \tag{1.38}$$

$$\Gamma(\overline{B}_s^0(t) \to \overline{f}) = |\overline{A}_{\overline{f}}|^2\Big[|g_+(t)|^2 + \Big|\frac{1}{\lambda_{\overline{f}}}\Big|^2|g_-(t)|^2 + \mathfrak{Re}\{\frac{1}{\lambda_{\overline{f}}}g_+^*(t)g_-(t)\}\Big]. \tag{1.39}$$

Using the set of Equations 1.28 and the constraint 1.31, the decay rates are then expressed as:

$$\begin{aligned}
\Gamma(B_s^0(t)\to f) &= |A_f|^2 e^{-\Gamma_s t}\Big[\frac{1+|\lambda_f|^2}{2}\cosh(\frac{\Delta\Gamma_s t}{2})+\frac{1-|\lambda_f|^2}{2}\cos(\Delta m_s t)\\
&\quad -\mathfrak{Re}(\lambda_f)\sinh(\frac{\Delta\Gamma_s t}{2})-\mathfrak{Im}(\lambda_f)\sin(\Delta m_s t)\Big], \qquad (1.40)\\
\Gamma(B_s^0(t)\to \overline{f}) &= |\overline{A}_{\overline{f}}|^2\Big|\frac{q}{p}\Big|^2\Big[\frac{1+1/|\lambda_f|^2}{2}\cosh(\frac{\Delta\Gamma_s t}{2})-\frac{1-1/|\lambda_f|^2}{2}\cos(\Delta m_s t)\\
&\quad -\mathfrak{Re}(\frac{1}{\lambda_f})\sinh(\frac{\Delta\Gamma_s t}{2})+\mathfrak{Im}(\frac{1}{\lambda_f})\sin(\Delta m_s t)\Big], \qquad (1.41)\\
\Gamma(\overline{B}_s^0(t)\to f) &= |A_f|^2\Big|\frac{p}{q}\Big|^2\Big[\frac{1+|\lambda_f|^2}{2}\cosh(\frac{\Delta\Gamma_s t}{2})-\frac{1-|\lambda_f|^2}{2}\cos(\Delta m_s t)\\
&\quad -\mathfrak{Re}(\lambda_f)\sinh(\frac{\Delta\Gamma_s t}{2})+\mathfrak{Im}(\lambda_f)\sin(\Delta m_s t)\Big], \qquad (1.42)\\
\Gamma(\overline{B}_s^0(t)\to \overline{f}) &= |\overline{A}_{\overline{f}}|^2\Big[\frac{1+1/|\lambda_f|^2}{2}\cosh(\frac{\Delta\Gamma_s t}{2})+\frac{1-1/|\lambda_f|^2}{2}\cos(\Delta m_s t)\\
&\quad -\mathfrak{Re}(\frac{1}{\lambda_f})\sinh(\frac{\Delta\Gamma_s t}{2})-\mathfrak{Im}(\frac{1}{\lambda_f})\sin(\Delta m_s t)\Big]. \qquad (1.43)
\end{aligned}$$

where we have defined the complex quantities:

$$\lambda_f = \frac{q}{p}\frac{\overline{A}_f}{A_f} \text{ and } \overline{\lambda}_f = \frac{p}{q}\frac{A_{\overline{f}}}{\overline{A}_{\overline{f}}}. \qquad (1.44)$$

In the special case where the B_s^0-$\overline{B}_s^0$ decays into final state f which is a CP eigenstate, we have:

$$\mathcal{CP}|f\rangle = \pm|f\rangle \quad , \quad \lambda_f = \lambda_{\overline{f}} \qquad (1.45)$$

From the three complex quantities: $A_f, \overline{A}_f, q/p$, one can construct the phase-convention independent quantities, three real amplitude:

$$|A_f| \ , \ |\overline{A}_f| \ , \ |q/p| \qquad (1.46)$$

and one complex phase:

$$\lambda_f = \frac{q}{p}\frac{\overline{A}_f}{A_f} \text{ and} \qquad (1.47)$$

All CP violation observables can be expressed by phase-convention independent If CP is a good symmetry then it there exist some phases ξ_{CP} and ξ where the Lagrangian is invariant under 1.15. From this condition we distinguish three forms of CP violation

- CP violation in the decay: this type occurs when the $B_s^0 \to f$ and $\overline{B}_s^0 \to \bar{f}$ decay amplitudes are different:

$$\left|\frac{\overline{A}_f}{A_f}\right| \neq 1. \tag{1.48}$$

- CP violation in the mixing: This type occurs when B_L and B_H mass eigenstates can not be chose to be the CP eigenstates:

$$\left|\frac{q}{p}\right| \neq 1; \tag{1.49}$$

- CP violation in the interference between a decay without mixing $M^0 \to f$ and a decay with mixing $M^0 \to \bar{M}^0 \to f$. This type occurs decays into a final that are common to B_s^0 and $\overline{B}_s^0$:

$$\Im(\lambda_f) \neq 0 \quad \text{and} \quad \lambda_f = \frac{q}{p}\frac{\overline{A}_f}{A_f} \neq 1. \tag{1.50}$$

The time-dependent CP asymmetry into CP eigenstates is defined as:

$$\mathcal{A}_{CP} = \frac{\Gamma[\overline{B}_s^0(t) \to f] - \Gamma[B_s^0(t) \to f]}{\Gamma[\overline{B}_s^0(t) \to f] + \Gamma[B_s^0(t) \to f]} \tag{1.51}$$

Using the decay rates in Equations 1.40-1.43, the time-dependent CP asymmetry is written as:

$$\mathcal{A}_{CP} = -\frac{(1-|\lambda_f|^2)\cos(\Delta m_s t) - 2\mathfrak{Im}\lambda_f \sin(\Delta m_s t)}{(1+|\lambda_f|^2)\cosh(\Delta\Gamma_s t/2) - 2\mathfrak{Re}\lambda_f \sinh(\Delta\Gamma_s t/2)} + \mathcal{O}(a_{fs}). \tag{1.52}$$

where the latter asymmetry contains all CP violation sources. If any of CP violation types occurs, the asymmetry is non-zero.

1.5 $B_s^0 \to J/\psi\phi$ channel

1.5.1 Phenomenology

In the following we are interested in the $\overline{b} \to \overline{c}c\overline{s}$ transitions for the B_s^0 mesons, which is an example of CP violation in the interference. This transition provides a direct way to measure the β_s parameter in which we are interested in this thesis. Two important considerations should be noted:

- the decays amplitudes of the transitions in hand are dominated by one CKM phase, meaning that the CP violation in the decay is small;
- for the B_s^0 system, the CP violation in the mixing is very small in the Standard Model.

If we neglect the CP violation in the mixing and in the decay for our study, the asymmetry Equation 1.5.1 becomes:

$$\mathcal{A}_{CP} = \frac{\mathfrak{Im}\lambda_f \sin(\Delta m_s t)}{\cosh(\Delta\Gamma_s t/2) - \mathfrak{Re}\lambda_f \sinh(\Delta\Gamma_s t/2)}. \tag{1.53}$$

The CP violation is dominated by the interference between decays with and without the mixing, giving these modes a source of clean theoretical interpretation. One of the most promising examples of $\bar{b} \to \bar{c}c\bar{s}$ transitions is the $B_s^0 \to J/\psi\phi$ channel. This channel has relatively large branching ratio: $(1.4 \pm 0.5) \times 10^{-3}$. Within the Standard Model, the decay $B_s^0 \to J/\psi\phi$ is dominated by tree level transitions, while the penguin transitions are suppressed, these are represented in Figure 1.4. The weak phase of the decay

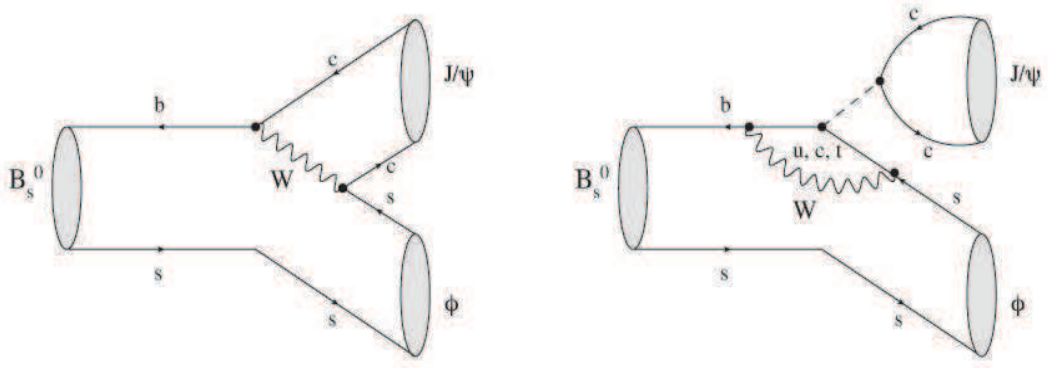

Figure 1.4: Feynman diagrams contributing to the decay $B_s^0 \to J/\psi\phi$, within the Standard Model. Left: tree; right: penguins.

$B_s^0 \to J/\psi\phi$ channel is related to the CP-violating phase β_s. The relation though is not trivial due to problem of penguin pollution. The decay can be mediated via two distinct quark-level transitions with different CKM structure. The $\bar{b} \to \bar{c}c\bar{s}$ decay amplitude can be expressed as a combination of tree (A_T), electroweak and QCD penguin amplitudes [23]:

$$\begin{aligned} A(\bar{b} \to \bar{c}c\bar{s}) &= V_{cs}V_{cb}^*(A_T + P_c) + V_{us}V_{ub}^* P_u + V_{ts}V_{tb}^* P_t \\ &= V_{cs}V_{cb}^*(A_T + P_c - P_t) + V_{us}V_{ub}^*(P_u - P_t), \end{aligned} \tag{1.54}$$

because $V_{ts}V_{tb}^* = -V_{us}V_{ub}^* - V_{cs}V_{cb}^*$, with three generations. P_i denotes the penguin amplitude with internal i-quark, $i \in \{u, c, t\}$. Since:

$$V_{cs}V_{cb}^* \sim A\lambda^2(1 - \lambda^2/2), \tag{1.55}$$

and:

$$V_{us}V_{ub}^* \sim A\lambda^4(\rho + i\eta), \tag{1.56}$$

The contribution of $(P_u - P_t)$ is suppressed by a factor $\sim \lambda^2 \simeq 0.05$ with respect to $(A_T + P_c - P_t)$. The $B_s^0 \to J/\psi\phi$ decay amplitudes are dominated by a single weak phase:

$$\Phi_D = \arg(V_{cs}V_{cb}^*), \tag{1.57}$$

The phase Φ_M dominates the mixing box diagram is sometimes called "the B_s^0 mixing phase", and is equal to $2\arg(V_{ts}V_{tb}^*)$. The phase difference between decay with and without oscillation is then:

$$\phi^{B_s^0 \to J/\psi\phi} \equiv -\arg(\eta_f \lambda_f) = \Phi_M - 2\Phi_D + \delta_s^{peng,SM}. \tag{1.58}$$

Where the $\delta_s^{peng,SM}$ is the phase of the penguin contribution within the Standard Model. The estimation on the penguin pollution ranges from $0.1 - 10^{-4}$ [25, 26]. This contribution though can be controlled experimentally via the transition $\bar{b} \to \bar{d}c\bar{c}$ decay (e.g. $B_s^0 \to J/\psi\bar{K}^{*0}$) where the penguin diagram is not suppressed with respect to the tree diagram. This channel has first been observed at CDF [27] and confirmed by LHCb [28]. The phase $\phi^{B_s^0 \to J/\psi\phi}$ is the observable phase we will measure in the experiment. In the rest of the document, we simply call it ϕ_s to simplify the equations and because there is no ambiguity with other decay modes. Noting that:

$$\Im\lambda_f = -\eta_f \sin\phi_s \text{ and } \Re\lambda_f = \eta_f \cos\phi_s, \tag{1.59}$$

we can re-write the decay rates (1.4):

$$\begin{aligned}
\Gamma(B_s^0 \to f) &= |A_f|^2 e^{-\Gamma_s t}\Big[\cosh\left(\frac{\Delta\Gamma_s t}{2}\right) - \eta_f \cos\phi_s \sinh\left(\frac{\Delta\Gamma_s t}{2}\right) \\
&\quad + \eta_f \sin\phi_s \sin(\Delta m_s t)\Big], \qquad (1.60) \\
\Gamma(\overline{B}_s^0 \to f) &= |A_f|^2 e^{-\Gamma_s t}\Big[\cosh\left(\frac{\Delta\Gamma_s t}{2}\right) - \eta_f \cos\phi_s \sinh\left(\frac{\Delta\Gamma_s t}{2}\right) \\
&\quad - \eta_f \sin\phi_s \sin(\Delta m_s t)\Big]. \qquad (1.61)
\end{aligned}$$

New Physics If we consider that New Physics affects M_{12} and Γ_{12}, its contribution to $\Delta B = 2$ transitions can be parameterized in a model independent manner by introducing the complex parameters Δ_s, $\tilde{\Delta}_s$ [29]:

$$M_{12}^{tot} = M_{12}^{SM}\Delta_s = M_{12}^{SM}|\Delta_s|e^{i\phi_s^{\Delta}}, \tag{1.62}$$

$$\Gamma_{12}^{tot} = \Gamma_{12}^{SM}\tilde{\Delta}_s = \Gamma_{12}^{SM}|\tilde{\Delta}_s|e^{i\phi_s^{\tilde{\Delta}}}. \tag{1.63}$$

The phase ϕ_s can then be expressed as a function of its Standard Model value and the phase ϕ_s^{Δ} of the New Physics parameters Δ_s, $\tilde{\Delta}_s$ and the penguin pollution from both Standard Model and New Physics:

$$\phi_s = -2\beta_s + \phi_s^{\Delta} + \phi_s^{\tilde{\Delta}} + \delta_s^{peng,SM} + \delta_s^{peng,NP}, \tag{1.64}$$

It is important to note that the same New Physics phase, ϕ_s^{Δ}, is expected to modify other independent quantities like a_{fs}. A relation between the mixing parameters ϕ_s and a_{fs} is written as follows:

$$a_{fs} = \left|\frac{\Gamma_{12}^{SM}}{M_{12}^{SM}}\right| \sin(\phi_{s,SM}^{M/\Gamma} + \phi_s^{\Delta}), \tag{1.65}$$

$$a_{fs} = -\frac{\Delta\Gamma_s}{\Delta m_s}\frac{S_{J/\psi\phi}}{\sqrt{1 - S_{J/\psi\phi}^2}}\delta. \tag{1.66}$$

with:

$$\delta = \frac{\tan(\phi_{s,SM}^{M/\Gamma} + \phi_s^{\Delta})}{\tan(-2\beta_s + \phi_s^{\Delta} + \phi_s^{\tilde{\Delta}} + \delta_s^{peng,SM} + \delta_s^{peng,NP})}, \tag{1.67}$$

$$S_{J/\psi\phi} = \sin(-2\beta_s + \phi_s^{\Delta} + \phi_s^{\tilde{\Delta}} + \delta_s^{peng,SM} + \delta_s^{peng,NP}). \tag{1.68}$$

This relation can be used to extract the New Physics ϕ_s^{Δ} and the penguin contributions.

The New Physics contribution from the Γ_{12} term is expected to be small due to different strong constraints from well measured observables, in addition the penguin contributions in this decay is highly suppressed and could be neglected. Finally the Standard Model prediction for β_s is small. So *only* in the case where these contributions vanishes, one can write:

$$\phi_s \sim \phi_s^{\Delta}. \tag{1.69}$$

and:

$$\Delta\Gamma_s = 2|\Gamma_{12}^{SM}|\cos(\phi_{s,SM}^{M/\Gamma} + \phi_s^{\Delta}), \tag{1.70}$$

This is can be reflected on a_{fs} as:

$$a_{\rm fs} = \frac{|\Gamma_{12}^{\rm SM}|}{|M_{12}^{\rm SM}|}\frac{\sin(\phi_{\rm s,SM}^{\rm M/\Gamma} + \phi_{\rm s}^{\Delta})}{|\Delta_{\rm s}|}. \tag{1.71}$$

In the above equations, $a_{\rm fs}$ is the flavour specific asymmetry [30]. The latest measurement of the like-sign dimuon charge asymmetry A_{sl}^{b} by D0 collaboration [31] implies a significant deviation of a_{fs} from the Standard Model expectation. If this is true, one expect that the $\phi_{\rm s}$ is also affected without excluding, however, the possibility of sizable penguin contributions.

1.5.2 $\mathbf{B_s^0 \to J/\psi\phi}$ differential decay rates

The decay $\rm B_s^0 \to J/\psi\phi$ is a pseudo-scalar ($\rm B_s^0$) decaying into a final states composed of two vectors: $\rm J/\psi$ and ϕ. This type of decay is called $P \to VV$ decay. The $\rm B_s^0$ particle has a spin of 0 while the spin of $\rm J/\psi$ and ϕ vectors is equal to 1. Total spin conservation in quantum mechanics infer three possible values of the relative angular momentum of the vector particles ($l = 0, 1$ and 2). Each one of these values has a unique decay amplitude. The CP eigenvalue (η_f) of the final state is given by:

$$\begin{aligned} {\rm CP}|{\rm J/\psi\phi}\rangle_\ell &= \eta_f |{\rm J/\psi\phi}\rangle_\ell \\ &= (-1)^\ell |{\rm J/\psi\phi}\rangle_\ell \,. \end{aligned} \tag{1.72}$$

The final state is then an admixture of CP-even ($l = 0$, 2) and CP-odd ($l = 1$) states. To disentangle statistically these states, an angular analysis for the decay product is required. The final state has four particle, so the direction of the momentum of each one of them can define the polarization angles. The three decay angles are: θ, ψ and ϕ, these are shown in Figure 1.5 in the transversity basis. Where in the coordinate system of the $\rm J/\psi$ rest frame (where the ϕ and $\rm B_s^0$ meson move in the x direction, the z axis is perpendicular to the decay plane of $\phi \to K^+K^-$, and $p_y(\rm K^+) \geq 0$), the transversity polar and azimuthal angles (θ, φ) describe the direction of the μ^+. In the rest frame of the ϕ meson, the angle ψ is the angle between $\vec{p}(\rm K^+)$ and $-\vec{p}(\rm J/\psi)$. In this basis [37], the amplitudes at $t = 0$, $A_0(0)$ and $A_{\|}(0)$ the amplitude of the transition to the CP-even final state with $l = 0, 2$, while $A_{\perp}(0)$ is the amplitude to a transition to the CP-odd final state with $l = 1$. δ_0, $\delta_{||}$ and $\delta_{\perp}$ are the corresponding argument for the amplitudes. The K^+K^- meson at the final state of the decay is an orbital

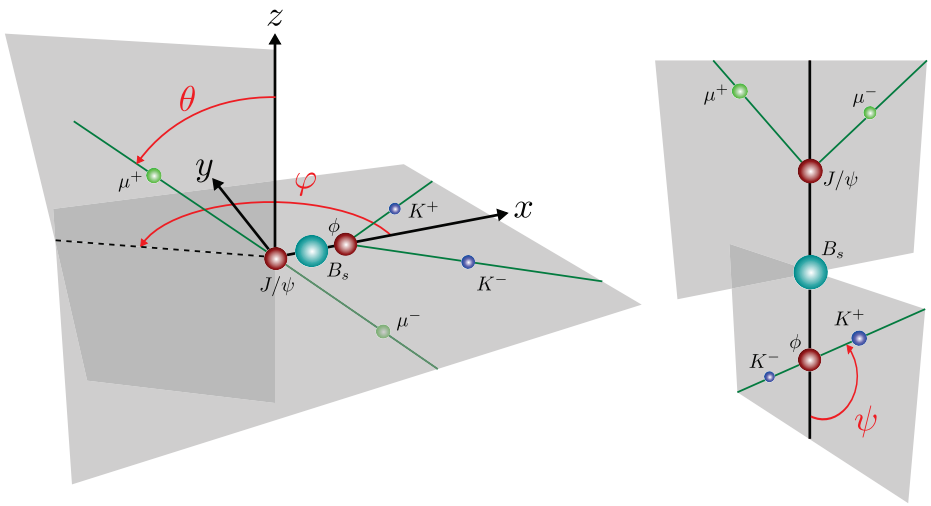

Figure 1.5: Angle definition: θ is the angle formed by the positive lepton (ℓ^+) and the z axis, in the J/ψ rest frame. The angle φ is the azimuthal angle of ℓ^+ in the same frame. In the ϕ meson rest frame, ψ is the angle between $\vec{p}(\mathrm{K}^+)$ and $-\vec{p}(\mathrm{J}/\psi)$. The definition is the same whether a B_s^0 or a $\overline{\mathrm{B}}_s^0$ decays.

P-wave amplitude. But in the range of the ϕ mass, other partial waves both resonant $f_0(980)$ and non-resonant contribute to the K^+K^- system.

For the amplitude of the P-wave contributions we can write :

$$|A_\perp(0)|^2 + |A_0(0)|^2 + |A_\parallel(0)|^2 = A_P^2, \tag{1.73}$$

where A_P^2 is the total P-wave strength.

The S-wave has an CP eigenstate of -1, and its angular distribution is different from the three P-wave components. The S-wave fraction of the amplitudes is $R_S = A_S^2/(A_P^2 + |A_S|^2)$ and the corresponding strong phase for this contribution is δ_S. We put $\delta_0 = 0$ where only the differences between the strong phases are observables. It was estimated in [38] that this contribution could be as large as 10% under the ϕ mass peak. This is for decay modes arises from a $s\bar{s}$ quark pair.

The CP-even and CP-odd states are now separated not only by their

k	$h_k(t)$	$\bar{h_k}(t)$	$f_k(\theta,\psi,\varphi)$
1	$\lvert A_0(t)\rvert^2$	$\lvert\bar{A}_0(t)\rvert^2$	$2\cos^2\psi(1-\sin^2\theta\cos^2\varphi)$
2	$\lvert A_{\lvert\lvert}(t)\rvert^2$	$\lvert\bar{A}_{\lvert\lvert}(t)\rvert^2$	$\sin^2\psi(1-\sin^2\theta\sin^2\varphi)$
3	$\lvert A_\perp(t)\rvert^2$	$\lvert\bar{A}_\perp(t)\rvert^2$	$\sin^2\psi\sin^2\theta$
4	$\Im\{A^*_{\lvert\lvert}(t)A_\perp(t)\}$	$\Im\{\bar{A}^*_{\lvert\lvert}(t)\bar{A}_\perp(t)\}$	$-\sin^2\psi\sin 2\theta\sin\varphi$
5	$\Re\{A^*_0(t)A_{\lvert\lvert}(t)\}$	$\Re\{\bar{A}^*_0(t)\bar{A}_{\lvert\lvert}(t)\}$	$\frac{1}{\sqrt{2}}\sin 2\psi\sin^2\theta\sin 2\varphi$
6	$\Im\{A^*_0(t)A_\perp(t)\}$	$\Im\{\bar{A}^*_0(t)\bar{A}_\perp(t)\}$	$\frac{1}{\sqrt{2}}\sin 2\psi\sin 2\theta\cos\varphi$
7	$\lvert A_S(t)\rvert^2$	$\lvert\overline{A_S}(t)\rvert^2$	$2(1-\sin^2\theta\cos^2\varphi)$
8	$\Re\{A^*_S(t)A_{\lvert\lvert}(t)\}$	$\Re\{\overline{A^*_S}(t)\overline{A_{\lvert\lvert}}(t)\}$	$\sqrt{6}\sin\psi\sin^2\theta\sin 2\varphi$
9	$\Im\{A^*_S(t)A_\perp(t)\}$	$\Im\{\bar{A}^*_S(t)\bar{A_\perp}(t)\}$	$\sqrt{6}\sin\psi\sin 2\theta\cos\varphi$
10	$\Re\{A^*_S(t)A_0(t)\}$	$\Re\{\bar{A}^*_S(t)\bar{A}_0(t)\}$	$4\sqrt{3}\cos\ \psi(1-\sin^2\theta\cos^2\varphi)$

Table 1.1: Definition of the functions $h_k(t)$, $\bar{h_k}(t)$ and $f_k(\theta,\psi,\varphi)$ of Eq. 1.74 and 1.75.

different lifetimes, but by their decay angles too. The differential decay rates for B^0_s and $\overline{B}^0_s$ decays are given by the following general expressions:

$$\frac{d^4\Gamma(B^0_s\to J/\psi\phi)}{dt\,d\cos\theta\,d\varphi\,d\cos\psi}\equiv\frac{d^4\Gamma}{dt\,d\Omega}\propto\sum_{k=1}^{10}h_k(t)f_k(\Omega), \tag{1.74}$$

and:

$$\frac{d^4\Gamma(\overline{B}^0_s\to J/\psi\phi)}{dt\,d\cos\theta\,d\varphi\,d\cos\psi}\equiv\frac{d^4\overline{\Gamma}}{dt\,d\Omega}\propto\sum_{k=1}^{10}\bar{h_k}(t)f_k(\Omega). \tag{1.75}$$

Where k is 1,2,...10, where we have three terms for purely P-wave contributions, one for purely the S-wave contribution an six terms of interference among these four contributions. The functions $h_k(t)$, $,\bar{h_k}(t)$ and $f_k(\Omega)$ are defined in Table 1.1. The detailed formulas for the time-dependent functions $h_k(t)$, $,\bar{h_k}(t)$ are:

$$|A_0(t)|^2 = |A_0(0)|^2 e^{-\Gamma_s t}\Big[\cosh\left(\frac{\Delta\Gamma_s t}{2}\right) - \cos\phi_s \sinh\left(\frac{\Delta\Gamma_s t}{2}\right) + \sin\phi_s \sin(\Delta m_s t)\Big], \quad (1.76)$$

$$|A_\parallel(t)|^2 = |A_\parallel(0)|^2 e^{-\Gamma_s t}\Big[\cosh\left(\frac{\Delta\Gamma_s t}{2}\right) - \cos\phi_s \sinh\left(\frac{\Delta\Gamma_s t}{2}\right) + \sin\phi_s \sin(\Delta m_s t)\Big], \quad (1.77)$$

$$|A_\perp(t)|^2 = |A_\perp(0)|^2 e^{-\Gamma_s t}\Big[\cosh\left(\frac{\Delta\Gamma_s t}{2}\right) + \cos\phi_s \sinh\left(\frac{\Delta\Gamma_s t}{2}\right) - \sin\phi_s \sin(\Delta m_s t)\Big], \quad (1.78)$$

$$\Im\{A_\parallel^*(t)A_\perp(t)\} = |A_\parallel(0)||A_\perp(0)| e^{-\Gamma_s t}\Big[-\cos(\delta_\perp - \delta_\parallel)\sin\phi_s \sinh\left(\frac{\Delta\Gamma_s t}{2}\right) + \sin(\delta_\perp - \delta_\parallel)\cos(\Delta m_s t) - \cos(\delta_\perp - \delta_\parallel)\cos\phi_s \sin(\Delta m_s t)\Big], \quad (1.79)$$

$$\Re\{A_0^*(t)A_\parallel(t)\} = |A_0(0)||A_\parallel(0)| e^{-\Gamma_s t}\cos\delta_\parallel\Big[\cosh\left(\frac{\Delta\Gamma_s t}{2}\right) - \cos\phi_s \sinh\left(\frac{\Delta\Gamma_s t}{2}\right) + \sin\phi_s \sin(\Delta m_s t)\Big], \quad (1.80)$$

$$\Im\{A_0^*(t)A_\perp(t)\} = |A_0(0)||A_\perp(0)| e^{-\Gamma_s t}\Big[-\cos\delta_\perp \sin\phi_s \sinh\left(\frac{\Delta\Gamma_s t}{2}\right) + \sin\delta_\perp \cos(\Delta m_s t) - \cos\delta_\perp \cos\phi_s \sin(\Delta m_s t)\Big], \quad (1.81)$$

$$|A_S(t)|^2 = |A_S(0)|^2 e^{-\Gamma_s t}\Big[\cosh\left(\frac{\Delta\Gamma_s t}{2}\right) + \cos\phi_s \sinh\left(\frac{\Delta\Gamma_s t}{2}\right) - \sin\phi_s \sin(\Delta m_s t)\Big], \quad (1.82)$$

$$\Re\{A_S^*(t)A_\parallel(t)\} = |A_S(0)||A_\parallel(0)| e^{-\Gamma_s t}\Big[-\sin(\delta_{||} - \delta_s)\sin(\phi_s)\sinh\left(\frac{\Delta\Gamma_s t}{2}\right) + \cos(\delta_{||} - \delta_s)\cos(\Delta m_s t) - \sin(\delta_{||} - \delta_s)\cos\phi_s \sin(\Delta m_s t)\Big], \quad (1.83)$$

$$\Im\{A_S^*(t)A_\perp(t)\} = |A_S(0)||A_\perp(0)| e^{-\Gamma_s t}\sin(\delta_\perp - \delta_S)\Big[\cosh\left(\frac{\Delta\Gamma_s t}{2}\right) + \cos\phi_s \sinh\left(\frac{\Delta\Gamma_s t}{2}\right) - \sin\phi_s \sin(\Delta m_s t)\Big],$$

$$\Re\{A_S^*(t)A_0(t)\} = |A_S(0)||A_0(0)| e^{-\Gamma_s t}\Big[-\sin(\delta_0 - \delta_s)\sin(\phi_s)\sinh\left(\frac{\Delta\Gamma_s t}{2}\right) + \cos(\delta_0 - \delta_s)\cos(\Delta m_s t) - \sin(\delta_0 - \delta_s)\cos\phi_s \sin(\Delta m_s t)\Big]. \quad (1.84)$$

we highlighted the sign change in the time-dependent functions for the B_s^0 events:

$$|\bar{A}_0(t)|^2 = |\bar{A}_0(0)|^2 e^{-\Gamma_s t}\left[\cosh\left(\frac{\Delta\Gamma_s t}{2}\right) - \cos\phi_s \sinh\left(\frac{\Delta\Gamma_s t}{2}\right) - \sin\phi_s \sin(\Delta m_s t)\right], \quad (1.85)$$

$$|\bar{A}_\parallel(t)|^2 = |\bar{A}_\parallel(0)|^2 e^{-\Gamma_s t}\left[\cosh\left(\frac{\Delta\Gamma_s t}{2}\right) - \cos\phi_s \sinh\left(\frac{\Delta\Gamma_s t}{2}\right) - \sin\phi_s \sin(\Delta m_s t)\right], \quad (1.86)$$

$$|\bar{A}_\perp(t)|^2 = |\bar{A}_\perp(0)|^2 e^{-\Gamma_s t}\left[\cosh\left(\frac{\Delta\Gamma_s t}{2}\right) + \cos\phi_s \sinh\left(\frac{\Delta\Gamma_s t}{2}\right) + \sin\phi_s \sin(\Delta m_s t)\right], \quad (1.87)$$

$$\Im\{\bar{A}_\parallel^*(t)\bar{A}_\perp(t)\} = |\bar{A}_\parallel(0)||\bar{A}_\perp(0)| e^{-\Gamma_s t}\left[-\cos(\delta_\perp - \delta_\parallel)\sin\phi_s \sinh\left(\frac{\Delta\Gamma_s t}{2}\right) - \sin(\delta_\perp - \delta_\parallel)\cos(\Delta m_s t) + \cos(\delta_\perp - \delta_\parallel)\cos\phi_s \sin(\Delta m_s t)\right], \quad (1.88)$$

$$\Re\{\bar{A}_0^*(t)\bar{A}_\parallel(t)\} = |\bar{A}_0(0)||\bar{A}_\parallel(0)| e^{-\Gamma_s t}\cos\delta_\parallel\left[\cosh\left(\frac{\Delta\Gamma_s t}{2}\right) - \cos\phi_s \sinh\left(\frac{\Delta\Gamma_s t}{2}\right) - \sin\phi_s \sin(\Delta m_s t)\right], \quad (1.89)$$

$$\Im\{\bar{A}_0^*(t)\bar{A}_\perp(t)\} = |\bar{A}_0(0)||\bar{A}_\perp(0)| e^{-\Gamma_s t}\left[-\cos\delta_\perp \sin\phi_s \sinh\left(\frac{\Delta\Gamma_s t}{2}\right) - \sin\delta_\perp \cos(\Delta m_s t) + \cos\delta_\perp \cos\phi_s \sin(\Delta m_s t)\right], \quad (1.90)$$

$$|A_S(t)|^2 = |A_S(0)|^2 e^{-\Gamma_s t}\left[\cosh\left(\frac{\Delta\Gamma_s t}{2}\right) + \cos\phi_s \sinh\left(\frac{\Delta\Gamma_s t}{2}\right) + \sin\phi_s \sin(\Delta m_s t)\right], \quad (1.91)$$

$$\Re\{A_S^*(t)A_\parallel(t)\} = |A_S(0)||A_\parallel(0)| e^{-\Gamma_s t}\left[+\sin(\delta_{||} - \delta_s)\sin(\phi_s)\sinh\left(\frac{\Delta\Gamma_s t}{2}\right) + \cos(\delta_{||} - \delta_s)\cos(\Delta m_s t) - \sin(\delta_{||} - \delta_s)\cos\phi_s \sin(\Delta m_s t)\right], \quad (1.92)$$

$$\Im\{A_S^*(t)A_\perp(t)\} = |A_S(0)||A_\perp(0)| e^{-\Gamma_s t}\sin(\delta_\perp - \delta_S)\left[\cosh\left(\frac{\Delta\Gamma_s t}{2}\right) + \cos\phi_s \sinh\left(\frac{\Delta\Gamma_s t}{2}\right) + \sin\phi_s \sin(\Delta m_s t)\right], \quad (1.93)$$

$$\Re\{A_S^*(t)A_0(t)\} = |A_S(0)||A_0(0)|e^{-\Gamma_s t}\Big[+\sin(\delta_0-\delta_s)\sin(\phi_s)\sinh\left(\frac{\Delta\Gamma_s t}{2}\right) + \cos(\delta_0-\delta_s)\cos(\Delta m_s t) - \sin(\delta_0-\delta_s)\cos\phi_s\sin(\Delta m_s t)\Big]. \quad (1.94)$$

In the case where we only take into account the P-wave in the decay rates, an exact symmetry emerges under the simultaneous transformation:

$$\begin{aligned} \phi_s &\longleftrightarrow \pi-\phi_s\,, \\ \Delta\Gamma_s &\longleftrightarrow -\Delta\Gamma_s\,, \\ \delta_\parallel &\longleftrightarrow -\delta_\parallel\,, \\ \delta_\perp &\longleftrightarrow \pi-\delta_\perp\,. \end{aligned} \quad (1.95)$$

A more complete stuy of the symmetries including the S-wave is presented in [43]. If the interference between the S-wave and P-wave amplitudes is significant, we can resolve the ambiguity on the sign of ϕ_s [41].

ϕ_s can be extracted from several time-dependent functions, nevertheless for the small value predicted by the Standard,the sensitivity of the terms containing $\cos(\phi_s)$ is negligible. In this case, sensitivity comes from terms containing $sin(\phi_s)$. This means that the sensitivity on ϕ_s comes from the observation of the amplitude of the sinusoid in the time distribution $sin(\Delta m_s t)$. These terms have opposite sign between B_s^0 and $\overline{B}_s^0$, so if the events are not tagged a cancellation of the $sin(\phi_s)$ will occur. This shows the importance of the flavour tagging. The untagged decay rates actually provides a small information about ϕ_s through the terms in $\cos(\phi_s)$.

1.6 Experimental status of the ϕ_s measurement

On the contrary of B-factories, TeVatron energy reach enables its experiments CDF and D0 to perform the measurement of ϕ_s phase in the $B_s^0 \to J/\psi\phi$ channel. Latest update on the measurement from both experiments is published in [2] [1]. CDF experiment collected about 6 500 events using Neural Net approach for the selection with 5.2 fb^{-1}, whereas D0 uses a cut based analysis and finds about 3 400 with 6.1 fb^{-1}. In Figure 1.6 we quote the likelihood contours for CDF (left) and D0 (right), the two experiments have different definitions for the CP violating parameter: $\phi_s^{B_s^0\to J/\psi\phi}$ (D0) $= -2\beta_s$ (CDF).

CDF quotes $\beta_s \in [0.02, 0.52] \cup [1.08, 1.55]$ rad at 68%CL with p-value of 44% ($\sim 1\sigma$). D0 reported $\phi_s^{B_s^0\to J/\psi\phi} = -0.76^{+0.38}_{-0.36}(\text{stat}) \pm 0.02(\text{syst})$. The 2D contours from both experiments are compatible with the Standard

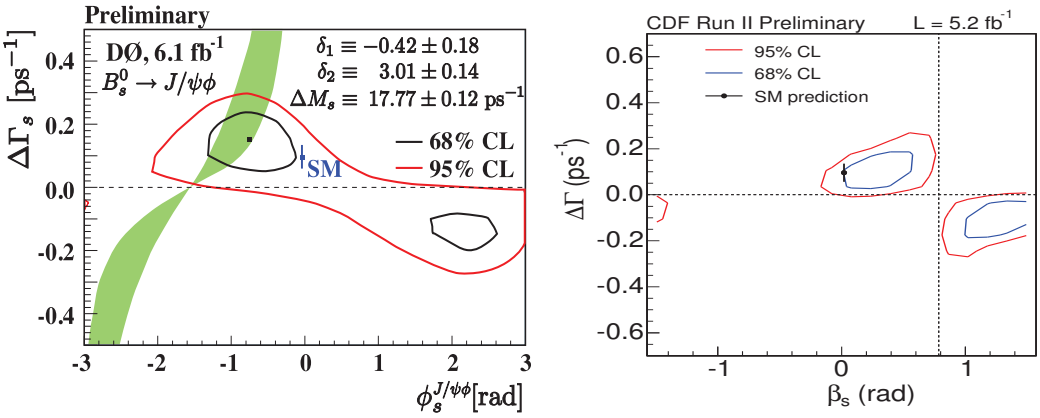

Figure 1.6: Left: Likelihood contours in the $\beta_s - \Delta\Gamma_s$ plane from CDF [1] using 5.2 fb^{-1}. Right: Likelihood contours in the $\phi_s^{B_s^0 \to J/\psi\phi} - \Delta\Gamma_s$ plane from D0 [2] using 6.1 fb^{-1}.

Model point. Furthermore, the two experiments reported an uncertainty of 0.4, 0.5 rad without external constraints on $\Delta\Gamma_s$. Other measurements related to the CP violation in the mixing are performed at D0, those are:

- the extraction of the flavour-specific asymmetry in the B_s^0 semi-leptonic decays a_{sl}^s, this parameter is extracted from the charge asymmetry A_{sl}^b measurement [44] in both B_s^0 and B_d^0 system. The extraction yields: $a_{sl}^s = -0.01 \pm 0.0059$;

- the branching ratio of $B_s^0 \to D^{(*)+}D^{(*)-}$ performed in [45], it is also related to the CP violation in the mixing: $\mathcal{B}(B_s^0 \to D^{(*)+}D^{(*)-}) = 0.035 \pm 0.015$.

The combination between these two measurements and that of $\phi_s^{B_s^0 \to J/\psi\phi}$ at D0 in [2], are combined in [46]. Figure 1.6 shows the confidence contour $\phi_s^{B_s^0 \to J/\psi\phi} - \Delta\Gamma_s$ with the above constraints applied, the p-value at the Standard Model point decrease to 6%. At LHCb, the measurement of ϕ_s with the first data 2010 will be presented in this work. Prospects to measure the flavour-specific asymmetry in the B_s^0 system a_{fs} at LHCb are explained in [30], [47] and [48].

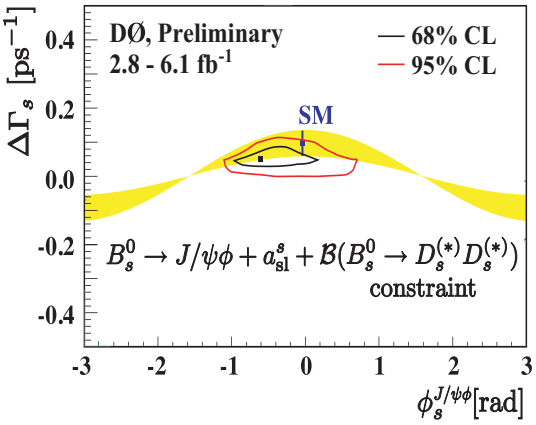

Figure 1.7: Confidence contour in the $\phi_s^{B_s^0 \to J/\psi\phi} - \Delta\Gamma_s$ plane from D0 preliminary results using 6.1 fb^{-1} of data, with strong phases constrained after combining with measurements: a_{sl}^s and $\mathcal{B}(B_s^0 \to D^{(*)+} D^{(*)-})$. The black square is the best-fit value, and the Standard Model expectation and uncertainty is indicated by the blue point with an error bar. The region allowed in new physics models given by $\Delta\Gamma_s = 2|\Gamma_{12}|\cos(\phi_{\Gamma,M})$ is also shown (yellow band). Only one new physics phase affecting M_{12} in the B_s^0 system is assumed.

1.7 ϕ_s analysis strategy

The phase ϕ_s is measured by fitting the differential decay rates in the $B_s^0 \to J/\psi\phi$ channel. To perform such procedure, we need to:

- trigger and select the $B_s^0 \to J/\psi\phi$ candidates;
- measure their proper time;
- measure their transversity (or helicity) angles of their decay products;
- tag their initial flavour;
- fit ϕ_s along with other physical parameters present in the decay rates;

The information on ϕ_s is obtained from the amplitude of the sinusoid term: $sin(\Delta m_s t)$ in the time-dependent distributions. When ϕ_s is large the term: $cos(\Delta m_s t)$ becomes important as well. For this reason a careful treatment is advised when dealing with experimental terms that affects the oscillation amplitude. Such factors are the proper time resolution σ_t, flavour tagging

power ϵ_{tag}, proper time acceptance and background pollution. The ingredients for large sensitivity on the ϕ_s phase is summarized in the following equation is

$$\sigma(\phi_s) \propto \frac{1}{\sqrt{N_{sig}\epsilon_{\text{eff}}}} \times \exp(-0.5 \times (\sigma_t \times \Delta m_s)^2), \tag{1.96}$$

where large signal yield N_{sig} and tagging power are necessary to reduce statistical error, good proper time resolution is important to resolve the fast B_s^0 oscillation.

To reduce the systematic error one should control of the proper time and angular acceptances. Wrong evaluation of these acceptances can lead to systematic biases. To control the angular acceptances. The $P \to VV$ mode $B_d^0 \to J/\psi K^{*0}$ is used to validate and study the angular acceptances in $B_s^0 \to J/\psi\phi$. Its kinematics are similar to those of $B_s^0 \to J/\psi\phi$ channel and the its amplitudes are well known [49, 50]. The flavour tagging performance is controlled using specific-flavour control channels $B_d^0 \to J/\psi K^{*0}$ and $B^+ \to J/\psi K^+$. They are selected in the same way as the signal so the b-hadrons share the same phase space, hence they have comparable tagging performances. The validation of the complex analysis of ϕ_s and its dependence on other channels require the measurements of the Δm_d, which was performed at LHCb [51], the measurement of $\sin(2\beta)$ in the $B_d^0 \to J/\psi K_S^0$ (see [52] decay and the measurement of B_s^0 oscillation Δm_s (see [53]). These measurements are considered as a test to the flavour tagging and the proper time resolution performances at LHCb. Furthermore, the contribution of S-wave from the $B_s^0 \to J/\psi f_0(980)$ decay under the mass peak of the ϕ particle is studied in [54], this is helps asses the size of such contribution in the decay rates of the $B_s^0 \to J/\psi\phi$ channel.

1.8 Summary

In this Chapter we presented the theoretical aspects upon which this thesis is based. The chapter covers CP violation in the $\bar{b} \to \bar{c}c\bar{s}$ transition. Within the Standard Model we saw that the CKM matrix is the main source of CP violation. A global fit to the experimental measurements of CKM elements provide a valuable test for the Standard Model predictions. Although the experimental data are in agreement with Standard Model picture, tensions among couple of measurements does exist making a room for New Physics contributions.

B_s^0 system is an important area where the New Physics is expected. Indeed the mixing takes place via a box diagram, where the New Physics can to intervene. The decay of these systems via $\bar{b} \to \bar{c}c\bar{s}$ transition provide an important test of the Standard Model prediction. One of these transitions is the $B_s^0 \to J/\psi\phi$ decay, where an interference between the decay with and without the mixing occurs. This gives rise to a phase called ϕ_s, which is one of the well-predicted parameters in Standard Model. New Physics contribution is expected to alter this prediction via loop processes. We have show that full understanding of possible New Physics effects need a non trivial studies of both mixing and penguin contributions.

Finally, the $B_s^0 \to J/\psi\phi$ is a $P \to VV$ decays where the final state is a mixture of CP states. An angular analysis is needed to provide a statistical separation between the final states. The interference between the dominated P-wave component and small S-wave component alters the differential decay rates.

CDF and D0 obtained first constrains on ϕ_s, their results are compatible with the Standard Model prediction and not sufficient to exclude New Physics contributions. Disagreement with Standard Model arises from latest measurement of the dimuonic asymmetry performed at D0. It rises the attention about possible New Physics in the ϕ_s since both measurements are related. At LHCb, a simple analysis strategy is adopted for the first data. A good proper time resolution is important to resolve the B_s^0 meson fast oscillation, flavour tagging of the initial B_s^0 meson is essential for ϕ_s sensitivity. The good performance of these parameters depend on the LHCb detector design and performances. This is discussed in the next chapter.

Chapter 2

Detector

In this Chapter, we introduce the Large Hadron Collider Beauty experiment (LHCb). This detector is specially designed for the search for New Physics in the beauty and charm decay sector. We review its detection capabilities along with its main sub-detectors. This experiment is one of four main experiments which is located along on the ring of the large hadron collider (LHC). In Section 2.1, we introduce general aspects about the LHC machine. In Section 2.2, we introduce general aspects of the LHCb detector followed by a brief description of 2010 data taking conditions. In Sections 2.3 we summarize the performance of the tracking system and its subdetectors involved. In Section 2.4 we summarize the particle identification system and its performance. Finally in Section 2.5 we explain the trigger architecture in LHCb and review the trigger lines used for event selection in the 2010 ϕ_s analysis.

2.1 LHC machine

The Large Hadron Collider experiment is a particle accelerator which collides protons and heavy ions at high energies. Figure 2.1 shows a general view of the collider with its main components and experiments. Its main objective is to deliver the world's highest energy collision at a high rate. This is done by exploring high energy and luminosity frontiers. This high energy scale should allow to discover the Higgs particle and the search for new particles predicted by New Physics models (e.g. supersymmetry). The luminosity accumulating now in LHC will enable high-precision measurements in the CP violation and rare decays sectors. The accelerator is installed within a circular tunnel 27 km in circumference. In March 2010, the LHC started colliding two proton beams at four interaction points at

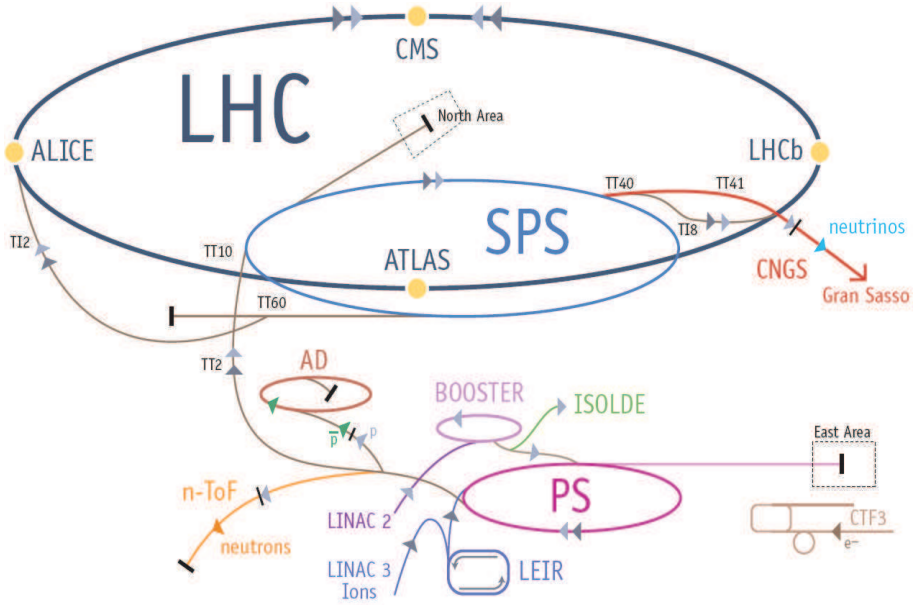

Figure 2.1: LHC accelerator complex, Linac2 protons are accelerated then inject them in the PS, SPS and finally in the LHC main ring.

center-of-mass energy $\sqrt{s} = 7\,\text{TeV}$[1]. This is the highest energy achieved in particle colliders around the world. Beams moving in the LHC ring are maintained on course by means of super-conducting magnets. The beams are stored at high energy for long periods (hours) during which the protons collide in the four experiments. LHC also delivers lead ion collisions to study the quark-gluon plasma soup and nuclear matter under extreme conditions similar to those of the beginning of the universe. The main experiments installed on the LHC ring are:

- ATLAS and CMS: general purpose experiments with full angular coverage. One of their main objectives is the search for the Higgs boson and super-symmetric particles;
- ALICE: a heavy ions detector, its physics program focuses on the study of nuclear matter;
- LHCb.

The four experiments have different coverages in pseudorapidity corresponding to there different physics programs. At LHCb, a unique rapidity range ($1.9 < \eta < 4.9$) to take advantage of the forward $b\bar{b}$ production. The

[1] this energy is expected to become 14 TeV at the next phase of running in 2014.

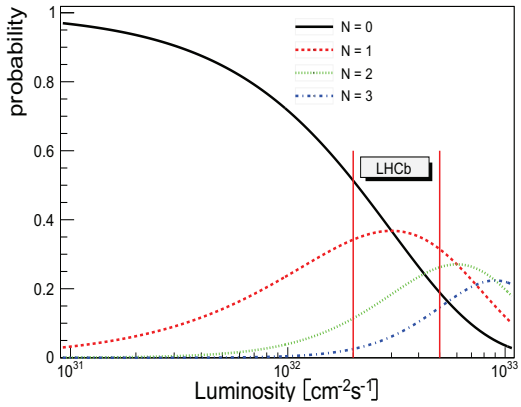

Figure 2.2: Probability of having $N = 0, 1, 2, 4$, or 4 inelastic interaction versus luminosity.

LHCb experiment has a unique luminosity settings. Beam conditions with low number of pp interactions per bunch are preferred, this reduces the detector occupancy and radiation damage level and simplify the physics analysis. Figure 2.2 shows the design luminosity, In order to reduce the LHC nominal luminosity to achieve such luminosity, beams are being locally displaced at LHCb in the vertical direction. The LHCb luminosity is $2 \times 10^{32}\,\mathrm{cm}^{-2}\mathrm{s}^{-1}\mathrm{cm}^{-2}\mathrm{s}^{-1}$ whereas the average luminosity of ATLAS and CMS is $> 10^{33}\,\mathrm{cm}^{-2}\mathrm{s}^{-1}$ and the β_* is higher. We will see later in this chapter that this choice was modified during the 2010 run due to constraints related to LHC machine running conditions.

2.2 LHCb detector

The LHCb experiment is a single-arm spectrometer with forward angular coverage $12 - 300$ mrad in the horizontal plane x, z and $10 - 250$ mrad in the vertical plane y, z; this defines the geometrical acceptance of LHCb detector. Figure 2.4 presents a side view of the experiment, where the z axis is along the beam, and the y axis lies along the vertical. The b quarks production mechanism at LHCb is dominated by the flavour excitation and gluon splitting processes [56].

b quarks are generally produced in pairs. All B-mesons and B-baryons are created at LHCb: B_d, B_u, B_s and B_c, Λ_b and Ξ_b. Figure 2.3 shows the correlation between the polar angles of the two b quarks. The angular distribution peaks at very low values meaning that the $\mathrm{b\bar{b}}$ pair is produced in

either backward or forward direction, this inspired the LHCb unique geometry. The LHCb detector consists of the following main sub-detectors :

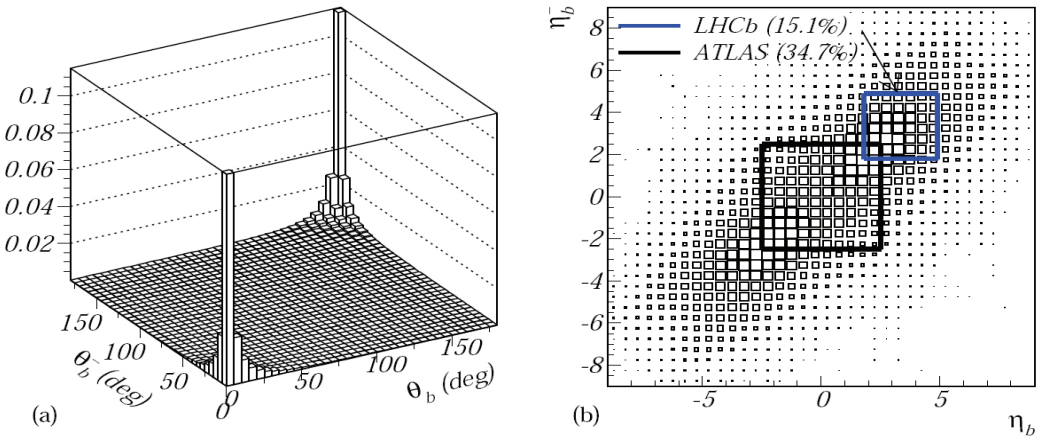

Figure 2.3: The angular correlation between the polar angles of the two b quark produced at LHCb.

- The VELO detector: surroundings the interaction region, it reconstructs the primary and secondary vertexes;
- the tracking system: based on large dipole magnet, with a trigger tracker station and three tracking stations;
- two RICH detectors: identifies the particles with different momentum ranges, separating pions from kaons;
- calorimeter system: identifies electrons, hadrons and neutrals;
- muon detector: uses five stations of detectors for detecting muons.

2010 Luminosity & run conditions The LHC started data taking at a center-of-mass energy 900 GeV late 2009. On 30 march 2010, the first proton proton collision at 7 TeV signaled the arrival of the LHC as the largest hadron collider in the world. The integrated luminosity accumulated at LHCb during 2010 was 37.66 pb^{-1} with an overall efficiency of $\sim$ 90%. Figure 2.5 (left) presents the delivered and recorded integrated luminosity per fill at LHCb.

In 2010, the configuration of the LHC machine was set to maximize the luminosity, the number of bunches in the machine increased to 344 but

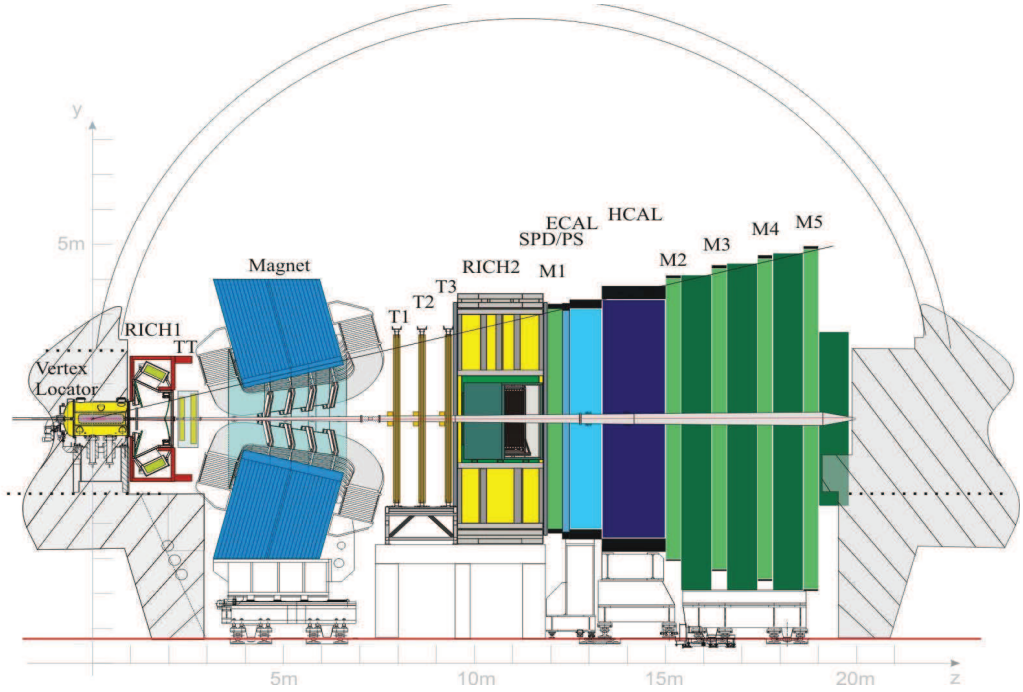

Figure 2.4: Side view of LHCb spectrometer, the beam pipe pass through the detector

with 1.1×10^{11} proton per bunch and $\beta^* = 3.5$m. This setting increased the instantaneous luminosity at LHCb to $1.6 \times 10^{32}\,\mathrm{cm}^{-2}\mathrm{s}^{-1}\mathrm{cm}^{-2}\mathrm{s}^{-1}$. On the other hand, the number of visible pp interactions per bunch (μ) increased. As a consequence the number of tracks and vertices per event increased, creating a challenging environment for the trigger and reconstruction systems. Indeed the rate of "pile-up" events sometimes reached six times the LHCb design value. Figure 2.5 (right) shows the distribution of μ per fill.

New Physics is expected in a wide range of measurements in CP and rare decays sectors. LHCb takes interest in a set of key measurements for which the detector is designed; those measurements are:

- Measurement of the mixing-induced CP violation in the $\mathrm{B}_\mathrm{s}^0 \to \mathrm{J}/\psi\phi$ channel;
- The tree-level determination of the angle γ;
- Charmless charged two-body B decays;
- Analysis of the decay $\mathrm{B}_\mathrm{s}^0 \to \mu^+\mu^-$;
- Analysis of the decay $\mathrm{B}_\mathrm{d}^0 \to K^{*0}\mu^+\mu^-$;

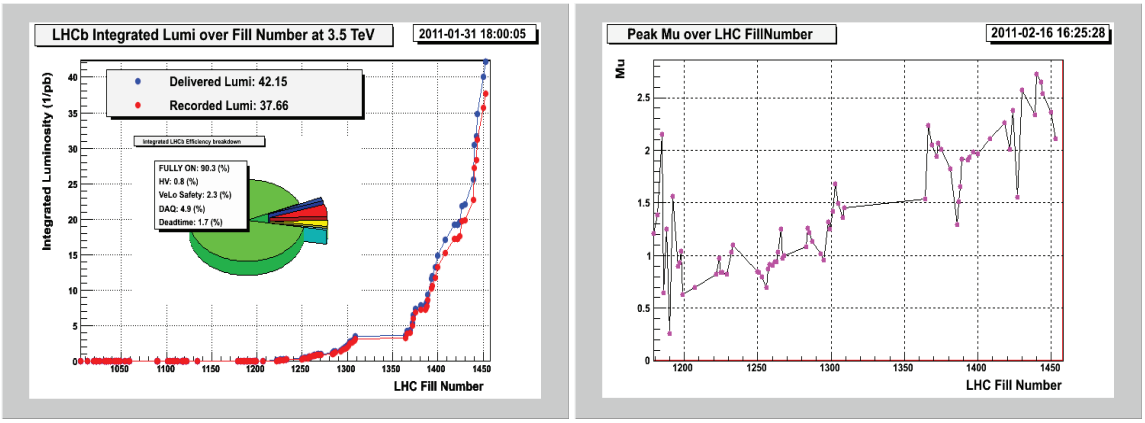

Figure 2.5: Left : The delivered (blue) and recorded (red) integrated luminosity at LHCb per fill, with the data taking inefficiency breakdown. Right : the number of visible interaction per bunch per fill.

- Analysis of radiative decays (e.g $B_s^0 \to \phi\gamma$).

New Physics is most expected in those measurement as they involve loop process where new particles can contribute or highly CKM suppressed modes within the Standard Model. b-hadron reconstruction is essential for these searches, this requires:

- particle identification allows the separation of kaons from pions and electrons from muons;
- tracking and vertexing to measure accurately momentum, energy and achieve an excellent proper time resolution;
- reliable trigger system to cope with the fast data taking rates.

In the following, we describe the LHCb sub-detectors and review their performance.

2.3 Tracking

The study of the boosted B and D mesons in the LHCb requires the measurement of their proper time with good resolution. In the $B_s^0 \to J/\psi\phi$ channel, the B_s^0 mesons oscillate with high frequency; an excellent proper time resolution is necessary to resolve this fast oscillation. The tracking

system in LHCb consists of the vertex locator (VELO), magnet, four tracking stations, one tracking station (TT)[2] before the magnet, and three tracking stations (T1, T2, T3) after the magnet.

2.3.1 VELO

The VErtex LOcator [57], is the closest detector to the beam at LHC ($\sim$ 8 mm), the velo provides a precise measurement of track parameters which are used then to reconstruct the primary and secondary vertices [58]. The VELO consists of 21 silicon modules along the beam axis. Each module is made of two silicon half disks. These modules measure the radial r and azimuthal ϕ coordinates. Figure 2.6 shows an overview of the VELO with its main parts. The construction of the VELO followed a number of require-

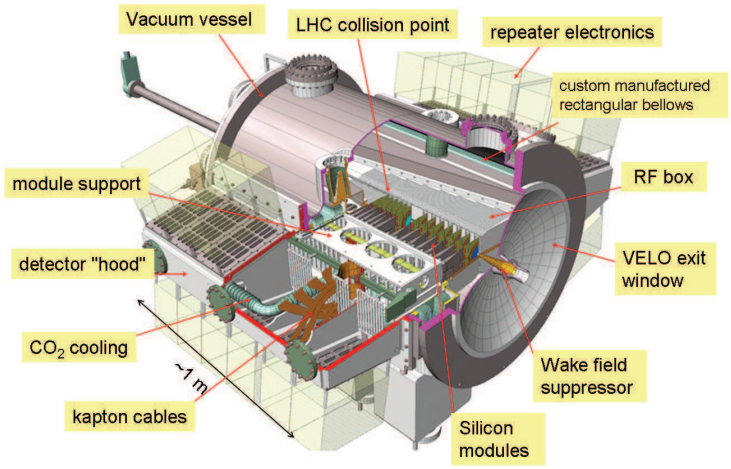

Figure 2.6: Over view of the VELO vacuum vessel.

ments and constraints, these comes from the angular acceptance of the downstream detectors, extreme radiation environment, strongly nonuniform fluences and integration into the LHC machine. The VELO should be as close as possible to the beam with least material in the detector acceptance.The two halves of the VELO move away from the beam axis during the ramping and injection phases and moves close to the beam axis when stable beam conditions are obtained.

[2]Tracker Turicensis.

2.3.2 Magnet

Measuring the momentum of charged particles is performed using the dipole magnet [59]. The integrated field of the magnet is $\sim$ 4Tm; this field is able to bend the tracks of charged particles to measure their momenta with resolution of $\delta p/p \sim 0.4\%$. Figure 2.7, shows an overview of the magnet which is oriented on the y axis. LHCb magnet is a warm dipole magnet, the polarization of the magnet can be inverted. This is particularly important to study right-left asymmetry detection in the magnet and the related systematic error for some CP violation related analysis [47].

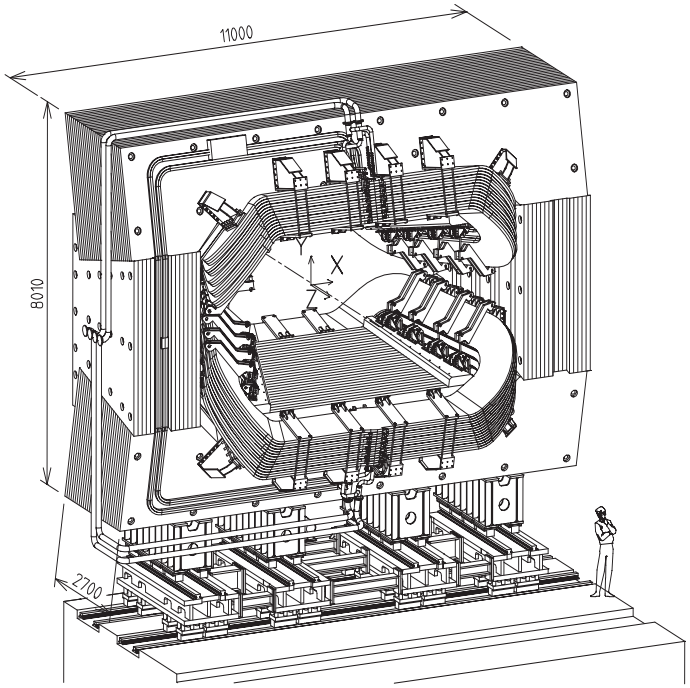

Figure 2.7: Perspective view of the LHCb dipole magnet with its current and water connections (units in mm). The interaction point lies behind the magnet.

2.3.3 Silicon Tracker

The silicon tracker comprises two sub trackers :

- tracker turicensis (TT) [60] is placed between the RICH1 system and the magnet. It consists of four detection layers-see Figure 2.8 (left)-

each one consists of half modules that covers half of the LHCb acceptance; each half consists of a row of seven silicon sensors organized into either two or three readout sectors;

- inner tracker (IT) [61] : placed in the center of T stations after the magnet, it consists of four individual detector boxes that are arranged around the beampipe as seen in Figure 2.8 (right).

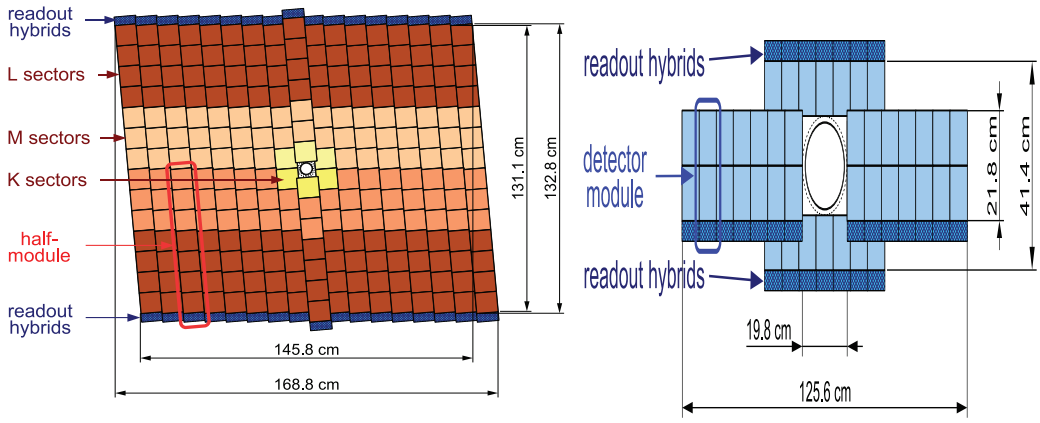

Figure 2.8: Left : Layout of the third TT detection layer. Different readout sectors are indicated by different shadings. Right : Layout of an x detection layer in the second IT station.

The inner tracker used to reconstruct the trajectories of charged particles. The TT main objective is to determine momentum of tracks with high impact parameters.

2.3.4 Outer Tracker

The outer tracker is a drift-time detector [62] that coveres the rest area of the T stations outside the IT. It is used for the tracking and momentum determination of charged particles over large area acceptance. It consists of an array straw tubes modules arranged in three stations (Figure 2.9). Each module contains two layers of drift-tubes. To ensure a fast drift time below the time of two successive bunch crossing at LHC < 50 ns, a gas composition of Argon, CF_4 and CO_2 is used.

2.3.5 Performance

The track reconstruction algorithm at LHCb searches for track candidates [64, 65, 66] in the VELO region and the T stations. Their trajectories are refitted

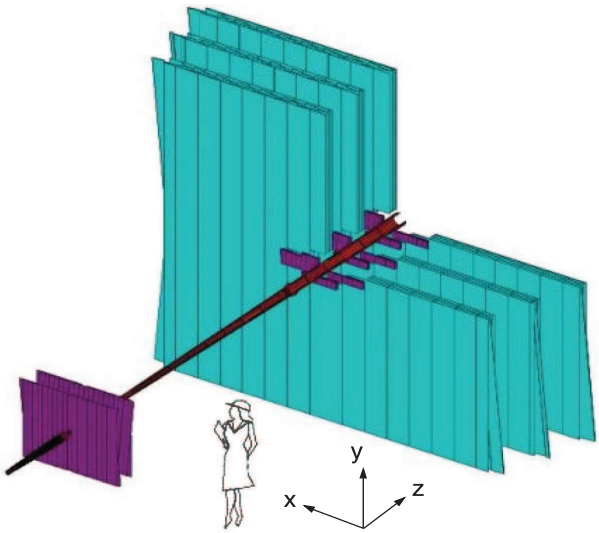

Figure 2.9: Arrangement of the OT modules in layers and stations

using a Kalman filter [67]. The χ^2 of the fit and the pull distribution of the track parameters are calculated to estimate the quality of the fit. Tracks are classified following their trajectories at LHCb (see Figure 2.10):

- *Long tracks* pass through the whole tracking system from the VELO to the T stations. Their momentum are the most precise;
- *Upstream* tracks pass only the VELO and TT stations. They are used to understand the RICH particle identification algorithm and may be used in the flavour tagging;
- *Downstream* tracks traverse only the TT and T stations;
- *VELO tracks* are measured only in the VELO, those are used in the primary vertex reconstruction;
- *T tracks* only measured in the T stations they are produced in the secondary interaction. They may be used for RICH2 studies.

The reconstruction performance is estimated using

- tracking efficiency, defined as the fraction of reconstructible tracks[3] that are successfully reconstructed [4];

[3] tracks which have the minimum number of hits in the relevant subdetector.

[4] track having at least 70% of its associated hits originating from a single Monte Carlo particle.

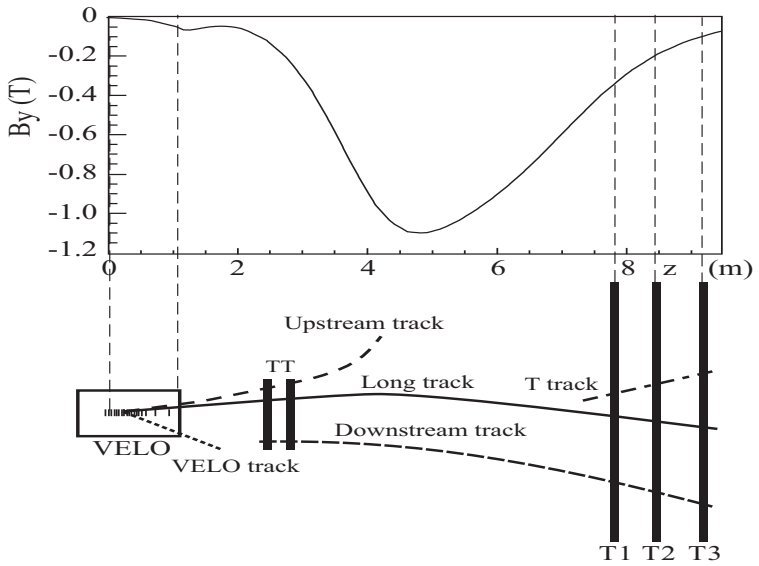

Figure 2.10: long, upstream, downstream, VELO and T tracks visual definition. For reference the main B-field component is plotted above as a function of the z coordinate.

- ghost rates, defined as the fraction of reconstructed tracks that are not matched to a true Monte Carlo particle.

Tracking performance with 2010 data:
The tracking efficiency for long tracks is plotted in Figure 2.11 (left). This plot is obtained using $K_S \to \pi\pi$ decays from 2010 data. We observe an efficiency $> 95\%$ for track momentum higher than 200 MeV/c. In addition the agreement between the Monte Carlo and 2010 data is apparent in the plot. The impact parameter resolution is plotted in the Figure 2.11 (right) as a function of track p_{T}. The behavior in the Figure shows a slight disagreement between 2010 data and Monte Carlo, this is under investigation. But the resolution achieved with data produces an excellent proper time resolution in the $\mathrm{B_s^0} \to \mathrm{J}/\psi\phi$ channel ~ 50 fs.

2.4 Particle identification

Particle identification is fundamental component for the study of CP violation and rare decays in the B decays. For the selection of $\mathrm{B_s^0} \to \mathrm{J}/\psi\phi$ channel, it is essential to separate kaons from pions and muons from pions to reduce the background contamination. The kaon identification is

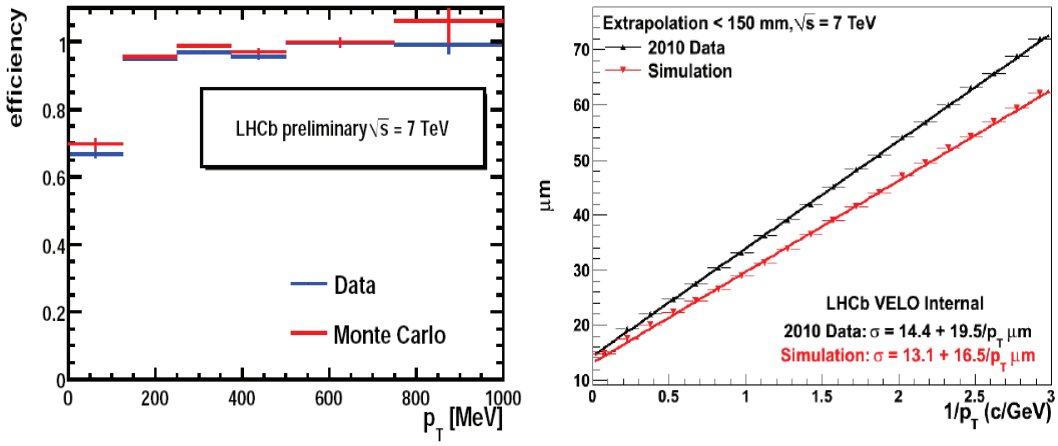

Figure 2.11: Left: The tracking efficiency for long tracks, $K_S \rightarrow \pi\pi$ candidates are used. (data in blue and Monte Carlo in red). Right: resolution of impact parameter of a track as a function of its inverse momentum (2010 data in black and Monte Carlo in red) [68].

important for the flavour tagging performance. The particle identification system consist of :

- Two RICH systems
- The calorimeter system
- The muon system

In the following, we describe briefly these systems.

2.4.1 RICH system

RICH technology relies on measuring the Čerenkov angle [69]. The Čerenkov angle of a moving charged particle a dielectric medium. If the charged particle's velocity exceeds the speed of light in the medium, it emits a cone of electromagnetic radiation at an angle θ_c to the particle's velocity.

$$\cos\theta_c = \frac{1}{n\beta} \tag{2.1}$$

where n is the refractive index of the medium. The particle's speed β is calculated by measuring angle θ_c. By measuring the momentum one can calculate the mass of the particle and hence identify it.

At large polar angles the particle momentum is softer than the momentum at small angles, two RICH [70] systems are used to cover a large momentum range $1 - 100\,\text{GeV}$ needed for the LHCb physics program. Both RICH detectors use an set of spherical and flat mirrors to project the light cones out of the acceptance. Hybrid Photon Detectors are used to detect Čerenkov photons in the rings of projected light. The radius of the ring measures the corresponding Čerenkov angle θ_c.

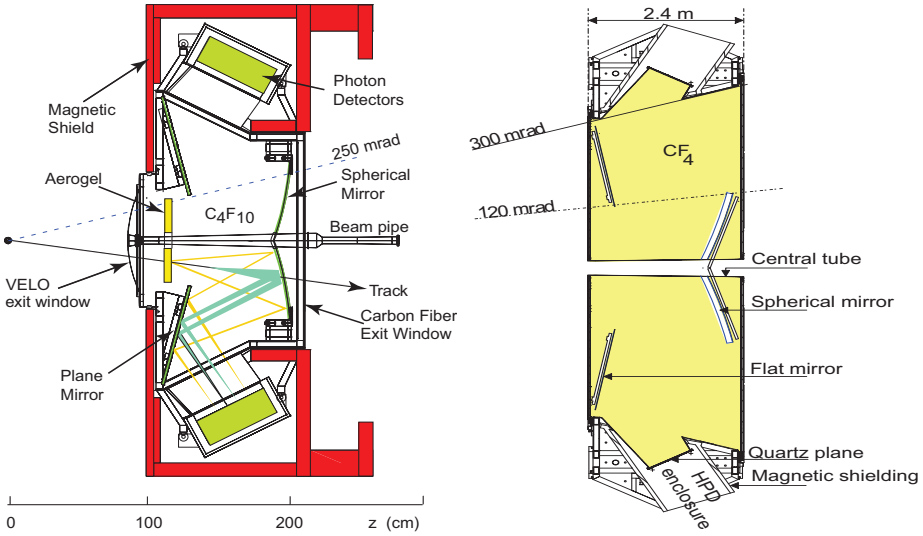

Figure 2.12: Side view of the RICH1 system (left), and RICH2 system (right)

The RICH system, seen in Figure 2.12, is composed of RICH1 located before the magnet and after the VELO; it identifies the low momentum $(1 - 60\,\text{GeV}/c)$ particles and covers the LHCb geometrical acceptance. The RICH1 contains aerogel and Fluorobutane gas (C_4F_{10}). The second RICH system (RICH2) is located between the last tracking station and the first muon station. It contains a CF_4 gas, and covers a reduced polar angle acceptance of $\pm 120\,\text{mrad}$ on the horizontal plane and $\pm 100\,\text{mrad}$ in the vertical plane.

2.4.2 Calorimeter system

Calorimeters in LHCb [71] are designed to identify electron and photon candidates for the trigger (L0). They provide a measurement of the energy and position of hadrons and photons and permit reconstruction of π^0. The calorimeter subdetector consists of :

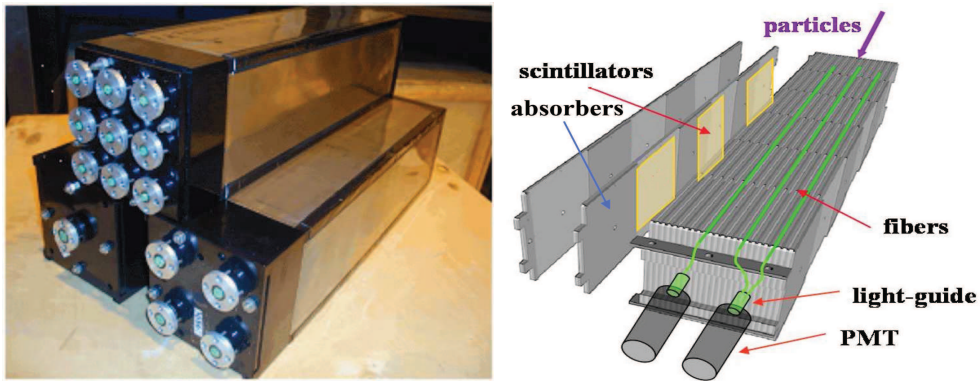

Figure 2.13: Left: Outer, middle and inner type ECAL modules. Right: Exploded view of scintillator-absorber layers illustrates the elementary periodic structure of a HCAL module.

- The Scintillating Pad Detector (SPD) consists of scintillating tiles. Its objective is to select charged particles, in order to improve the rejection of π^0 background with high E_T. The SPD is essential for the trigger Level-0 where it is used to reject events with high detector occupancy;

- The preshower detector (PS) consists of a 15 mm lead wall sandwiched between two scintillator pads. It helps detect electrons and hadrons. This is useful to reject background of charged pions;

- The electromagnetic calorimeter (ECAL) uses a sampling scintillator-lead structure, its designed resolution is $\sigma_E/E = 10\%/\sqrt{E} \oplus 1\%$ (E is in GeV). The ECAL detects electron and photons via the electromagnetic shower, Figure 2.13 (left) shows one of the HCAL modules.

- The hadronic calorimeter (HCAL) located after the (ECAL), it is made from iron and scintillating tiles as absorber and active material. The HCAL purpose is to detect hadrons interacting with tile material. The energy resolution of the HCAL is $\sigma_E/E = (69 \pm 5)\%/\sqrt{E} \oplus (9 \pm 2)\%$ (E is in GeV). Figure 2.13 (left) shows one of the ECAL modules.

2.4.3 Muon system

Muon identification is crucial for LHCb physics. Indeed, several key measurements at LHCb contain muons in its final state, such as the $B_s^0 \rightarrow J/\psi(\rightarrow \mu^+\mu^-)\phi(\rightarrow K^+K^-)$, $B_s^0 \rightarrow \mu^+\mu^-$. In addition muons coming from

semi-leptonic b decays are used for the flavor tagging process. Finally muons object are essential for the L0 online trigger where high p_T muons are used. The muon system at LHCb [72] is composed of five stations, see

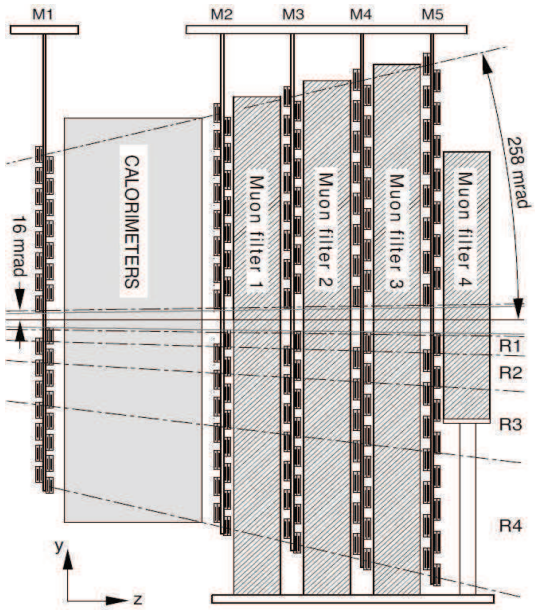

Figure 2.14: Side view of the muon system.

Figure 2.14, Four of them after the calorimeter (M2-M5) and one (M1) is located before the SPD. Each muon station is divided into four regions with different granularity. The minimum momentum required from a muon to cross the five station is $\sim$ 6 GeV. Multi-wire proportional chambers (MWPCs) are used for all regions except the inner region of M1, where a gaseous electron multiplier detectors (triple-GEM detectors) are used.

2.4.4 Performance

Information from the two RICH systems, calorimeters, and muon stations are combined to achieve the best charged and neutral particles identification. The ϕ_s analysis requires the identification of kaons and muons objects in the detector.

The particle identification algorithm for hadrons is based on the log-likelihood method. The method matches the hit pattern in the RICH to the expected behavior of the tracks under a given hypothesis [73]. The likelihood is maximized by varying the particle hypotheses (electron, muon, pion, kaon and proton) of the tracks in the event. This variation for the

kaon hypothesis is $\ln \mathcal{L}_K - \ln \mathcal{L}_\pi = \Delta \ln \mathcal{L}_{K\pi}$. The result is then the best hypothesis for each track and the likelihood decreases when changing from this solution to another hypothesis.

Muons with $p > 3\,\text{GeV}/c$ are reconstructed in the muon stations. Hits left by muons within a field of interest (FOI) around the extrapolation point of the track in each muon station are considered. The track in question is identified as muon when it leaves hits in a minimum number of muon stations [5]. For each track the difference in log-likelihood between the muon and pion hypothesis is determined and summed with the values of the RICH and calorimeter. This reduces the pion misidentification rate.

PID performance with 2010 data:

The Figure 2.15 presents the muons identification efficiency for both data and Monte Carlo as a function of their momentum. We observe a compatibility between the two efficiencies within the available statistics. The identification plot is made with muons from J/ψ. The performance

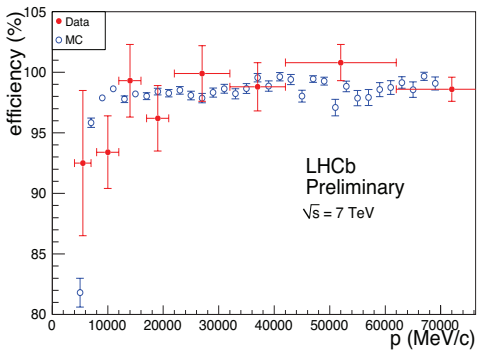

Figure 2.15: Left: J/$\psi \to \mu^+\mu^-$ mass distribution, the resolution obtained is $\sim$ 13 MeV/c^2. Right: comparison of the muon identification between data (in red) and Monte Carlo (in blue) [68]

of the PID on kaons is measured on data using tag and probe methode. $D^* \to D(K\pi)\pi$ sample are obtained by applying a cut on the mass difference: $m_{D^*} - m_{D\to K\pi}$. To measure the kaon mis-identification rate on data, the decay $K_S \to \pi\pi$ is used where kinematic cuts are applied to construct the signal. When the cut $\Delta \ln \mathcal{L}_{K\pi} > 0$ is applied to the sample, we observe a mis-identification Kaon-pion rate of 18%. A cut $\Delta \ln \mathcal{L}_{K\pi} > 5$ reduces the mis-identification rate to $\sim$ 7%.

[5] number of stations depend on the track momentum.

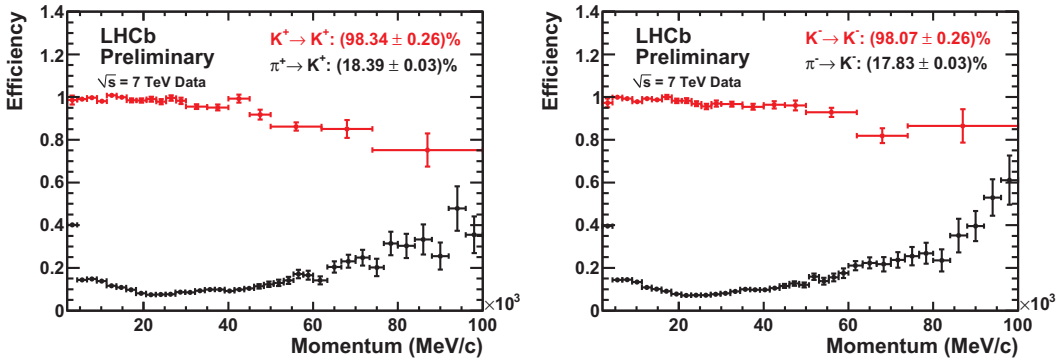

Figure 2.16: probability to identifies K^+ in red (left K^+, π^+ right K^-, π^-) and the probability to mis-identify a pion as a kaon in black [68].

2.5 Trigger

LHCb was initially designed to operate at a luminosity of $2 \times 10^{32} \mathrm{cm}^{-2}\mathrm{s}^{-1}$ at 14 TeV center-of-mass energy, where the number of interaction per bunch crossing is dominated by a single interaction. This choice of running scheme is to facilitate analysis and reduce the radiation damage. In 2010 the beam configuration was changed progressively, as a result, increasing the number of interaction per crossing achieved higher values of μ than those of the LHCb design. Figure 2.17 shows the architecture of the trigger system [74]; it is composed of two main levels:

- level-0 trigger is implemented in the hardware;
- High Level Trigger consists of two sub levels Hlt1 and Hlt2, both are implemented in the software.

In the following, we will describe each one of these components and its performance. At the design luminosity and energy. The bunch crossing with visible interactions are expected to contain a rate of 100 kHz of $b\bar{b}$ pairs; 15% of them include include a B decay chain contained completely inside the detector geometrical acceptance. Less than 1% of all inelastic events contain b quarks. This imposes a serious challenge on the trigger to select the interesting events for the LHCb physics program.

2.5.1 Level-0 trigger

The trigger is optimized to achieve the highest signal efficiency while rejecting at the same time background events. The purpose of the L0 trigger

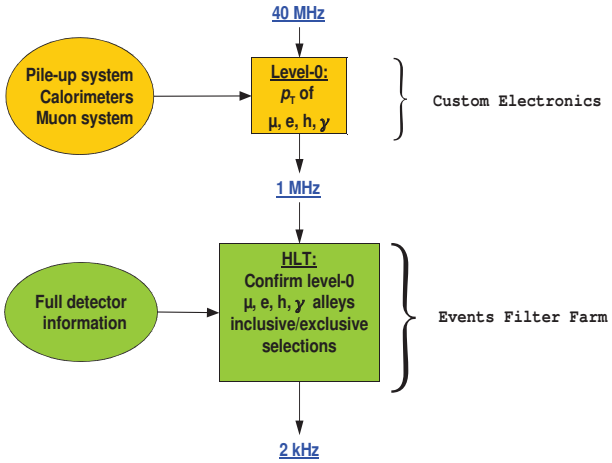

Figure 2.17: Scheme of the LHCb trigger system.

is to reduce the LHC beam crossing rate of 40MHz to the rate of 1MHz. The L0 trigger is divided into three components: the pile-up system, the L0 calorimeter trigger and the L0 muon trigger. Each one of these is connected to the corresponding sub-detector and to the L0 decision unit (DU). The latter collects all information calculated by the trigger systems to evaluate the final decision. The pile-up system distinguishes between cross-

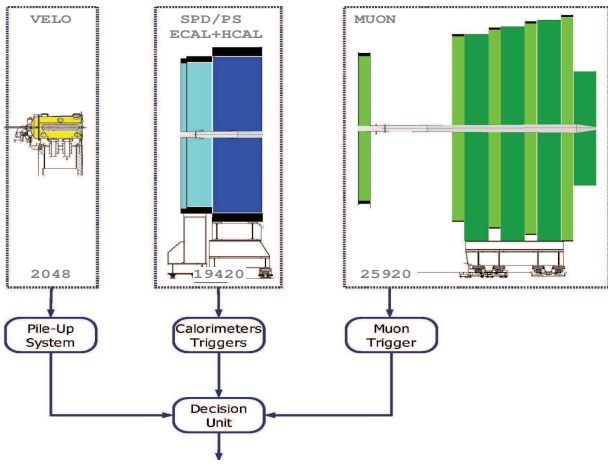

Figure 2.18: Overview of the L0 trigger.

ings with single and multiple visible interactions. It provides the position of the primary vertex candidates and a measurement of the total backward charged track multiplicity. The Calorimeter Trigger system looks for high E_T particles: electrons, γ, π^0 or hadrons, where all the SPD, PS, ECAL

and HCAL Calorimeter are implicated in identifying the particles. The E_T of all HCAL cells is summed to reject crossings without visible interactions. The muon chambers allow stand-alone muon reconstruction with a p_T resolution of $\sim$ 20%. The L0 muon trigger selects the two muons with the highest p_T for each quadrant of the muon detector. Track finding, at this trigger level, is performed by processing elements which combine the strip and pad data from the five muon stations to form towers which are pointing towards the interaction region. The L0 DU combines all signatures into one decision per crossing which is transmitted to the front-end electronics. Data selected by a specific L0 and HLT configuration is stored in a trigger configuration key "TCK", and every event contains an identifier to give the lines responsible of triggering it.

2.5.2 High level trigger

A software trigger runs on the CPU of the event filter farm, it executes selection algorithms on the data coming from the L0 level. The Hlt is divided into two phases: Hlt1, Hlt2. We present briefly these two stages.

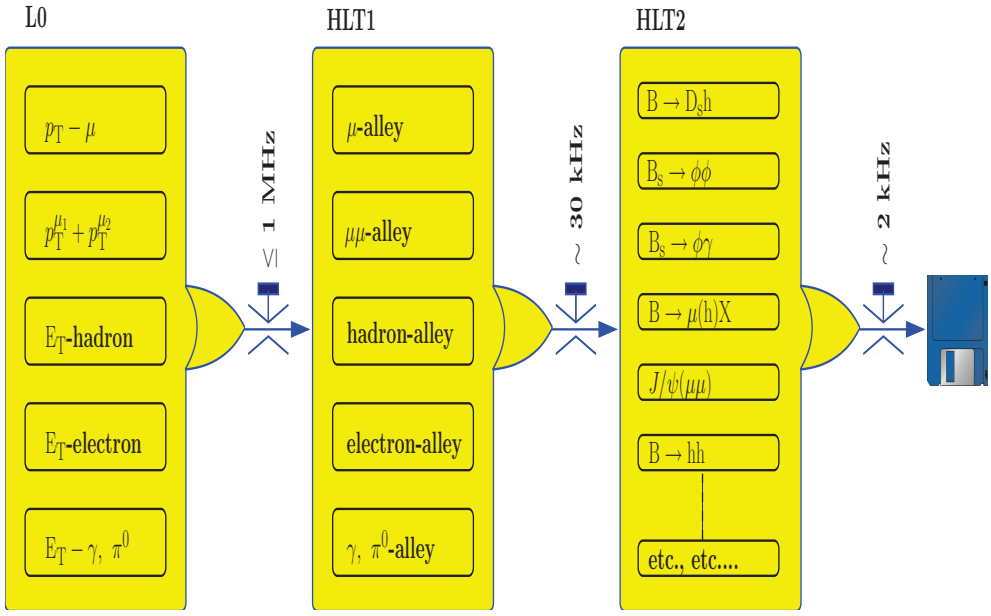

Figure 2.19: Flow-diagram of the different trigger sequences.

Hlt1 Hlt1 is designed to reconstruct particles in VELO and T-stations corresponding to L0 objects, or to confirm L0 γ and π^0 by the absence of

charged particles. Due to time and CPU limitations, a partial reconstruction of the event takes place at this level. Hlt1 uses alleys that address one of L0 trigger types. The alleys use sequence of algorithms involving information about the L0 object from VELO and/or tracking stations to confirm L0 findings. Basic information about tracks and primary vertex is calculated and then used to reduce the rate to $\sim$ 30kHz.

Hlt2 Hlt2 is a set of selection algorithms which uses information from off-line track reconstruction. One distinguishes between inclusive selections where the B candidate is partially reconstructed and exclusive selections where the B candidate is reconstructed as in the offline analysis. At this level, tracks are selected with loose cuts on their impact parameter and momentum. Those tracks are then used to form composite particles (e.g. ϕ and J/ψ). Finally those particles are used to for all selections. Hlt2 cuts on the invariant mass of the B or on the variables of pointing angle. The final trigger decision is a logical OR of the inclusive and exclusive selections. The trigger rate is reduced after Hlt2 to $\sim$ 2kHz.

For the $B_s^0 \to J/\psi\phi$ analysis, the analysis strategy is to avoid biases on the proper time distribution. This approache requires a dedicated trigger selections (lines) that do not apply any proper time biasing cuts at Hlt1 and Hlt2.

2.5.3 Trigger settings in 2010

In 2010 the trigger system underwent a challenging running condition. Indeed, the number of high pile-up events was increased. To cope with these conditions, A Global Event Cut on the hit multiplicities of the SPD (< 900) was introduced to reject these events. About 1kHz of trigger bandwidth was dedicated to muon trigger lines.

We describe here the muonic trigger lines relevant to our analysis in 2010 data. The final state of the $B_s^0 \to J/\psi\phi$ decay involves muons so we use the muon trigger lines for our analysis. There are two muon trigger lines designed for channels with μ in the final state:

- single-muon L0 (L0Muon) looks for one muon candidate requires its p_T to be greater than 1.4 GeV/c;
- dimuon L0 line (L0DiMuon) looks for the two muons candidates and requires the first to have $pT_1 > 0.46\,\text{GeV}/c$ and $pT_2 > 0.56\,\text{GeV}/c$;

Events that passed these two lines are processed then by the Hlt1 and Hlt2 that includes two different set of lines. The first set is Hlt1 and Hlt2 lines,

	Hlt1SingleMuonNoIP	Hlt1DiMuonNoIPL0	Hlt2UnbiasedJPsi
L0	L0-Muon	L0-DiMuon	-
p_T	$> 1.8\,\text{GeV}/c$	-	$> 500\,\text{MeV}/c$
p	$> 10\,\text{GeV}/c$	$> 10\,\text{GeV}/c$	-
Track χ^2/ndof	< 10	< 10	-
χ^2 of muon hits	< 16	< 16	-
Sum p_T of dimuon	-	$> 1\,\text{GeV}/c$	-
Dimuon DOCA	-	$< 0.5\,\text{mm}$	-
Dimuon mass	-	$> 2.5\,\text{GeV}/c^2$	$> 2977\,\text{MeV}/c^2$ $< 3211\,\text{MeV}/c^2$
Dimuon vertex χ^2	-	-	< 25

Table 2.1: Trigger cuts for the lifetime *unbiased* trigger lines used in trigger configuration key (TCK) 0x002e002a.

which do not bias the proper time. The "unbiased"Hlt1 lines use the momentum p and p_T cuts to reduce the rates, as follows:

- lines using the L0Muon candidates, the seeds matching the muon candidate are used to reconstruct the VELO tracks. In addition, an cut on the p_T is applied;
- lines using L0DiMuon candidates, seeds are used in the same as the previous line. In addition, a cut on the sum of two muons p_T is applied.

Only one line is used for the unbiased analysis of ϕ_s; This is the unbiased J/ψ line (Hlt2DiMuonUnbiasedJpsi). Once an event passed Hlt1, tracks are fitted and then identified as muons using the offline algorithms. Muon candidates are then selected by applying a cut on their invariant mass and the χ^2 of the vertex they form. Table 2.1 presents the cuts used for the unbiased lines at the Hlt1 and Hlt2.

In the ϕ_s analysis, two Hlt1 and Hlt2 lines which biases the proper time distribution of the B are used:

- Hlt1TrackAllL0 search for a single track starting from L0Muon or L0DiMuon candidate and uses isMuon criterion;
- Hlt1TrackMuon searches single track from candidates passed throughout L0 physics line.

These lines uses cuts on the impact parameter IP, the significance of the impact parameter IPS, p_T and P of the L0 muon track and the number of

hits in the VELO. Table 2.2 presents the cuts values for the two biased lines. Those lines represent 30% of the sample and they add to the ϕ_s sensitivity.

	Hlt1TrackAllL0	Hlt1TrackMuon
L0	L0-Physics	L0-Muon OR L0-DiMuon
IP	> 0.11mm	> 0.11mm
# Velo hits	> 9	> 9
# Missed Velo hits	< 3	< 3
p_T	$> 1.85\,\text{GeV}/c$	$> 0.8\,\text{GeV}/c$
p	$> 13.3\,\text{GeV}/c$	$> 8\,\text{GeV}/c$
$IP\chi^2$	> 34	> 25
IsMuon	-	True

Table 2.2: Trigger cuts for the lifetime *biased* trigger lines used in trigger configuration key (TCK) 0x002e002a.

Events are categorized as Trigger On Signal (TOS) on lifetime unbiased lines, where the signal tracks are those which responsible of firing the trigger lines, more details are given in Chapter 3. We restrict ourselves in the ϕ_s analysis to the use of only the TOS events.

2.6 Summary

In this Chapter we described the LHCb experiment physics motivation along with the detector main components. We also presented a review of the event reconstruction and particle identification performances on 2010 data.

The LHCb detector was designed to fulfill the physics program of the experiment. The ϕ_s analysis exploits the LHCb excellent performance with the 2010 data to deliver the first determination of the CP violating phase ϕ_s at LHCb. The excellent proper time resolution calculated with the tracking system is sufficient to resolve the B_s^0-$\overline{B}_s^0$ fast oscillation. High momentum resolution provides a very good B_s^0 mass resolution and enables the calculation of the angular variables with high precision. Particle identification systems provides an excellent $K - \pi$ separation. This is employed in both tagging and signal selection. In addition, the LHCb trigger architecture efficiently reduces the pp retention rates. Offline analysis is then applied

to the samples provided by the trigger lines. In the next Chapter, we will provide a detailed study about the offline selection process.

Chapter 3

Selection

In this chapter, two different selections for the $B_s^0 \to J/\psi\phi$ channel are presented. We first discuss the pivotal B_s^0 proper time unbiased selection. It is the one applied on first data taken in 2010. It is based on a collection of criteria, chosen to optimize the ϕ_s determination with preliminary data. These criteria are:

- to maximize the signal yield and reduce the background levels;
- to minimize the biases on the B_s^0 proper time and the angular distributions. This simplifies the analysis at early stage and reduces the induced systematic errors on the physical parameters.

The selection, designed for the $B_s^0 \to J/\psi\phi$ channel, is applied with minimal changes on two control channels[1]; $B_d^0 \to J/\psi K^{*0}$ and $B^+ \to J/\psi K^+$. Indeed selecting the B mesons, in those three channels, in the same way will assure similarity among their opposite-side tagging properties. In 2010, LHC machine was taking data at $\sqrt{s} = 7\,\text{TeV}$. We present a summary on B_s^0 effective lifetime [2] determination performed in the $B_s^0 \to J/\psi\phi$ channel using data taken during the 2010 run.

In the second part of this chapter, we present an alternative selection, where we remove all unbiased constraints. Notably we allow cuts that bias the proper time and angular distributions, hence we call it the "biased" selection.

[1] channels who are statistically abundant and kenimatically signal-like.

[2] In this chapter, we call the $\tau_{B_s}^{\text{single}}$ the quantity measured by fitting a single exponential to the B_s^0 proper time distribution defined in Equation 3.11. This is not the B_s^0 lifetime defined by $1/\Gamma_s$ which is determined by the full angular analysis presented in Chapter 5.

Compared to the unbiased selection, the proper time biased selection enhances the signal yield by removing the tight kinematic cuts. In addition, the biased cuts reduces the prompt background considerably. On the other hand, it creates a non-trivial proper time distortion. We present a method to determine this distortion, avoiding any reliance on Monte Carlo information.

In Section 3.1, we describe the Monte Carlo samples used in the development of the unbiased selection. In Section 3.2, we present the preselection cuts applied. Section 3.3 is divided into three parts. The first present the details of the unbiased selection optimization process. The second part shows the signal and background properties using the unbiased selection cuts on the Monte Carlo samples. Yields as well as distributions and acceptance functions for the proper time and angular variables are studied. The third and final part treats the impact of high pile-up on the selection performance. In Section 3.4, the unbiased selection results obtained with the 2010 data are reviewed along with the first measurement of the B_s^0 effective lifetime using a single exponential in the $B_s^0 \to J/\psi\phi$ channel. Finally, in Section 3.5 we develop a biased selection cuts based on Monte Carlo samples. We then present a data driven method to extract the proper time acceptance emerging from the biased cuts of this selection.

3.1 Monte Carlo simulation used

The selection is studied using "MC2010" [75] samples[3], a Monte Carlo simulation produced at 7 TeV with $\nu = 1$ where ν is the average number of pp interactions per bunch crossing, including elastic and diffractive processes. Tables 3.1, 3.2 and 3.3 summarize the relevant parameters in the production of these samples. The detector response available in the Gaudi framework is generated by several external simulation programs: the Pythia program generates events from a pp collision, the EvtGen program simulates the B-hadron decays. Both programs are steered by a Gaudi application named Gauss.

Background samples used to perform this study are:

- minimum bias: contains all expected physics generated from pp collisions;
- inclusive $b\bar{b}$: contains $b\bar{b}$ pair produced within the LHCb geometrical acceptance (i.e. $10 < \theta < 400$ mrad). Events in this sample are

[3] MC/2010/Beam3500GeV-VeloClosed-MagDown-Nu1/2010-Sim01Reco01-withTruth/

Channel	Eff. generator (%)	Stat.	$\mathcal{L}_{\text{int}}(\text{fb}^{-1})$
Signal			
$B_s^0 \to J/\psi\phi$	16.46 ± 0.31	955 072	0.38
Background samples			
$b\bar{b}$ inclusive	43.22 ± 0.31	20 422 580	5.2×10^{-6}
$J/\psi(\mu\mu)$ inclusive	20.78 ± 0.12	8 001 713	5.6×10^{-6}
$B_s^0 \to J/\psi(\mu\mu)X$	18.78 ± 0.14	1 600 000	0.012
$B^+ \to J/\psi(\mu\mu)X$	18.94 ± 0.15	6 400 000	0.033
$B_d^0 \to J/\psi(\mu\mu)X$	18.55 ± 0.15	6 400 000	0.031
Minimum bias	100	77 593 772	8.5×10^{-7}

Table 3.1: MC2010 samples used in this analysis with their generator level cut efficiency (The fraction of all generated events which in the LHCb acceptance region), number of events used in the analysis and corresponding integrated luminosity.

often called "long-lived", this is due to the fact that b-hadrons fly for long period before they decay;

- inclusive J/ψ: contains $J/\psi \to \mu\mu$ events, where the two muons are forced in the geometrical acceptance of the detector. This sample could be split into two categories:
  - prompt J/ψ: $J/\psi \to \mu\mu$ coming directly form the pp collision ($\sim$ 93%). They do not contain any b quarks;
  - non-prompt J/ψ: $J/\psi \to \mu\mu$ coming from the decay chain: pp $\to$ b $\Rightarrow J/\psi$. Those are a long-lived decays.
- $B_{u,d,s} \to J/\psi X$: contains modes involving a B meson decaying into J/ψ and something else. All decay products are forced in the LHCb geometrical acceptance. Those are a long-lived events.

The L0 trigger is applied to the minimum bias sample in order to reduce the CPU time required to analyze the sample, as well as reduce its size on disk. All samples are fully reconstructed using the reconstruction algorithm [63], where all tracks as well as primary and secondary vertexes, in event, are reconstructed. After passing the full reconstruction, the data sample is filtered in order to reduce its size and facilitate the data access. This filtering stage is called "Stripping". It contains a collection of streams where each stream contains output of selection algorithms that are specially designed for each analysis in LHCb. Using Monte Carlo informa-

Cross section	value (μb^{-1})
σ_{pp}	91.05
$\sigma_{b\bar{b}}$	0.457
$\sigma_{pp \Rightarrow J/\psi X}$	0.115
$\sigma_{pp \rightarrow b \Rightarrow J/\psi X}$	0.013
$\sigma_{pp \rightarrow b \Rightarrow J/\psi_{prompt} X}$	0.102

Table 3.2: MC2010 production cross sections at 7 TeV predicated by PYTHIA[56] and EvtGen[77].

tion, it is easy to separate the true signal candidates from false ones in the signal sample. In this study we make use of the "Background Category Tool" [76] in order to achieve this. This tool is designed to classify the composition of a sample using the Monte Carlo truth. Using this tool we:

- select only the true signal candidate in signal sample;
- remove any signal candidate that might exist in background samples;
- we have combined contributions from prompt component and long-lived ones in the same Monte Carlo sample. The tool categorizes background events according to their origin, hence facilitating the study. In the following section, we describe the preselction cuts applied to the Monte Carlo samples involved in the selection optimization.

3.2 Preselection

At this level, we apply loose cuts to reduce Ntuple sizes. The cuts used in the preselections are listed in Table 3.4 Typical event in LHCb contains many tracks, on average ~ 100 tracks at $\nu = 0.4$. Many tracks in each event fulfill the preselection cuts criterion as those cuts are loose, so it happens that more than one $B_s^0 \rightarrow J/\psi\phi$ candidate per event passes the selection creating what we call a "multiple-candidates" event. We choose to keep the candidate with the smallest χ^2/nDoF of the B_s^0 vertex[4]. This criterion is applied at the final stage of the analysis where all offline cuts are applied. In the J/ψ preselection, we select two long tracks [80] identified as

[4]several other possibilities are discussed in [79].

Branching fraction	PDG [78]	MC 2010
$BR(J/\psi \to \mu\mu)$	$(5.93 \pm 0.06) \times 10^{-2}$	5.933×10^{-2}
$BR(B_s^0 \to J/\psi\phi)$	$(1.3 \pm 0.4) \times 10^{-4}$	1.35×10^{-4}
$BR_{vis}(B_s^0 \to J/\psi\phi)$	$(3.77 \pm 1.16) \times 10^{-5}$	3.93×10^{-5}
$BR(B_s^0 \to J/\psi(\mu\mu)X)$	–	0.8×10^{-4}
$BR(B^+ \to J/\psi(\mu\mu)X)$	–	2.8×10^{-4}
$BR(B_d^0 \to J/\psi(\mu\mu)X)$	–	3.0×10^{-4}
$f_u(\%)$	$40 \pm 1.$	41
$f_d(\%)$	$40 \pm 1.$	41
$f_s(\%)$	11.1 ± 1.2	10.5

Table 3.3: Branching fraction for different channels used in this analysis. first column holds the PDG values, the second stands for MC2010 Monte Carlo simulation ones. Where f_u, f_d and f_s are the weakly decaying B^+, B_d^0 and B_s^0 fractions.

Decay mode	Cut
$J/\psi \to \mu^+\mu^-$	VeryLooseMuons muons $\chi^2_{track}/nDoF < 15$ $\chi^2_{vtx}/nDoF(J/\psi) < 25$ $\lvert M(\mu\mu) - M(J/\psi)\rvert < \pm 80\,MeV/c^2$
$\phi \to K^+K^-$	NoPIDsKaons kaons $\chi^2_{track}/nDoF < 10$ $\chi^2_{vtx}/nDoF(\phi) < 25$ $\lvert M(K^+K^-) - M(\phi)\rvert < \pm 50\,MeV/c^2$
$B_s^0 \to J/\psi\phi$	$\lvert M(B_s^0) - M(J/\psi\phi)\rvert < \pm 300\,MeV/c^2$

Table 3.4: $B_s^0 \to J/\psi\phi$ preselection cuts, those are applied to all samples used in this study.

muons using the so-called "VeryLooseMuons" criterion [81]. It requires at least one hit in number of muon stations depending on the track momentum. The two tracks are then combined into a vertex. This is the processes where the position of the decay point is determined along with the momentum and the mass of the resulting particle. Loose constraints are then applied on the invariant $\mu^+\mu^-$ and on the $\chi^2_{\text{vtx}}/\text{nDoF}$ of the J/ψ particle. The ϕ preselection starts with two long tracks, with loose $\chi^2_{\text{track}}/\text{nDoF}$ cuts. The surviving candidates are combined into a loose vertex, their invariant mass is required to be within 50 MeV/c^2 of the nominal mass of the ϕ particle. To reconstruct the B^0_s particle, we combine J/ψ and ϕ, into one vertex. We apply a loose constraint on the $\mu^+\mu^-K^+K^-$ invariant mass. Table 3.4 prsent the value of the cuts applied for the preselection. The overall efficiency of the reconstruction and preselection step is: $(41.89 \pm 0.05)\%$.

3.3 Offline unbiased selection

The selection is based on the analysis presented in [82] and [83], where a cut-based selection was developed using an old version of simulation "DC06" and the minimum bias sample was used as reference for background.

In this work, we optimize the cuts using the Monte Carlo simulation MC2010, generated with mean number of generated pile-up interaction of $\nu = 1$ at 7 TeV. The criterion used for the selection is to maximize:

$$\frac{S}{\sqrt{S+B}} \tag{3.1}$$

where S stands for the signal yield, B is yield of the background. We additionally imposes a constraint on the signal efficiency loss per cut, where it does not exceed 10%. In this study we use the $b\bar{b}$ sample as a reference for the background instead of minimum bias. Indeed this type of background has an exponential proper time distribution, which makes it more dangerous than prompt background when fitting for the phase ϕ_s [5]. Although inclusive $b\bar{b}$ is the targeted background in the optimization procedure, other sources of background are shown and the impact of the cuts are calculated on them for more information. For this analysis, we avoid any proper time biasing cuts such as impact parameter, vetex separation etc.... Obviously the contribution of the prompt background component is expected to be high. The cuts are applied consecutively during the optimization.

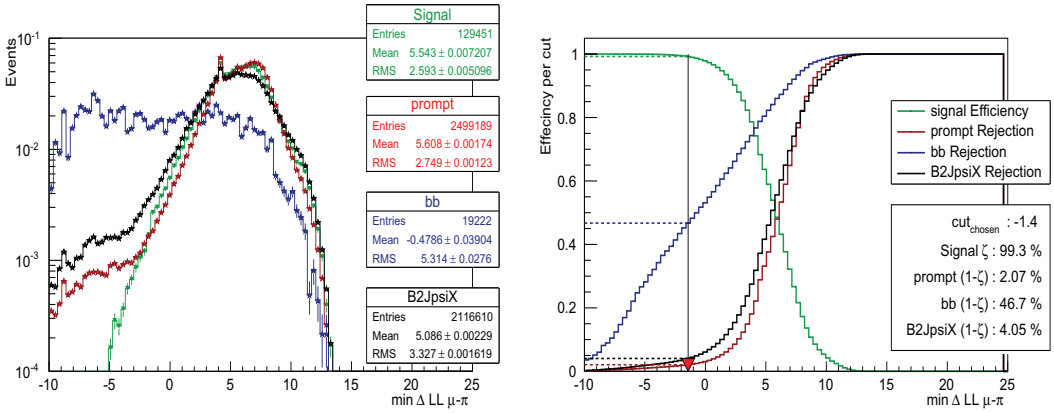

Figure 3.1: Left: minimum of $\Delta \ln \mathcal{L}_{\mu\pi}$ distribution for the muons, $B_s^0 \rightarrow J/\psi\phi$ signal candidates (green), $b\bar{b}$ inclusive candidates (blue), $B_{u,d,s} \rightarrow J/\psi X$ candidates (black), and prompt inclusive J/ψ candidates(red). Right: signal efficiency and individual background rejection rates per cut.

3.3.1 J/ψ selection

Some hadrons are misidentified as muons due to random combinations of false hits in the Muon Chambers. Discrimination between muons and those hadrons is best achieved by using the global $\Delta \ln \mathcal{L}_{\mu\pi}$. In Figure 3.1 we show the minimum $\Delta \ln \mathcal{L}_{\mu\pi}$ distribution for signal and background samples, the best cut lies around -1 with $\sim 50\%$ $b\bar{b}$ background rejection.

The $\Delta \ln \mathcal{L}_{\mu\pi}$ is not efficient against decays in flight, where some hadrons decay to μ before the muon station, consequently those particles are misidentified as muons by the muon stations. To reject those decays we make use of their $\chi^2_{\text{track}}/\text{nDoF}$ (track quality), Figure 3.2, because this quantity is expected to be much worse in case of decays in flight. This cut also helps reduce the ghost [5] rate in the signal sample [84].

Figure 3.2 shows the distributions of this cut for different background samples. The $b\bar{b}$ background has a significant portion of those decays. The cut chosen by the optimization is rather tight $\chi^2_{\text{track}}/\text{nDoF} > 3.2$, as we expect worse performance with real data, a more conservative cut on 5 is adopted.

Figure 3.3 shows the distribution of minimum p_T of the two muons. The cut on this quantity at 350 MeV/c reduces $b\bar{b}$ background by 9%. This

[5] tracks reconstructed with no Monte Carlo-truth due to random hits combinations during pattern recognition step in the reconstruction process.

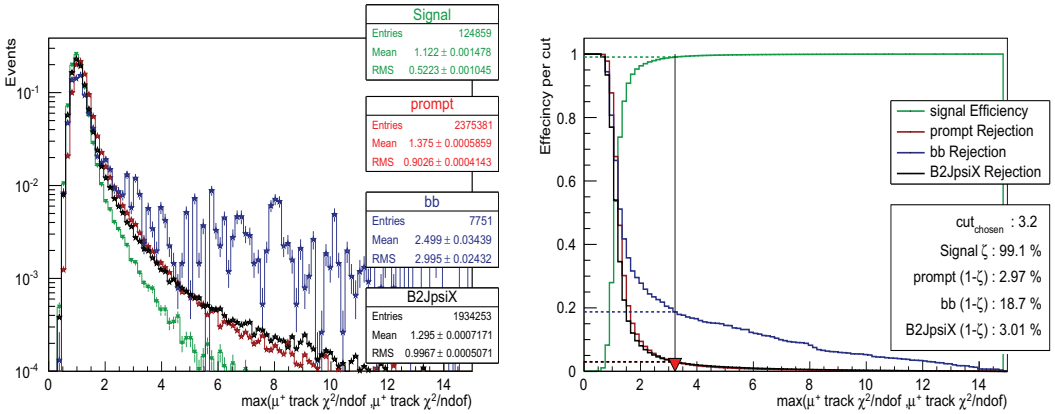

Figure 3.2: Left: maximum of muons' $\chi^2_{\text{track}}/\text{nDoF}$ distribution for $B^0_s \rightarrow J/\psi\phi$ signal candidates (green), $b\bar{b}$ inclusive candidates (blue), $B_{u,d,s} \rightarrow J/\psi X$ candidates (black), and prompt inclusive J/ψ candidates . Right: signal efficiency and individual background rejection ratios per cut.

cut does not discriminate between signal and background sources involving J/ψ. Careful usage of daughters p_T is advised, those cuts are known to create additional distortion on the angular variables [85].

Muons which passed the cuts are then vertex-ed. Cuts on the vertex quality (χ^2/nDoF) of the J/ψ particle are applied at 11 rejecting 18% of $b\bar{b}$ background with high signal efficiency as shown in Figure 3.4.

Figure 3.5 shows the mass distribution for signal and background samples (left) as well as the J/ψ mass distribution in the signal sample fitted with two Gaussians. The mass cut, $|M(\mu\mu) - M(J/\psi)|/\sigma_{m_{J/\psi}} < 1.4 \times 3$, takes in consideration the fact that J/ψ mass resolution changes with its momentum. More details are given in [86]. The overall efficiency of J/ψ selection cuts is : $\varepsilon_{\text{sel}} = (94.7 \pm 0.06)\%$, where the input number of events is those passing the preselection cuts.

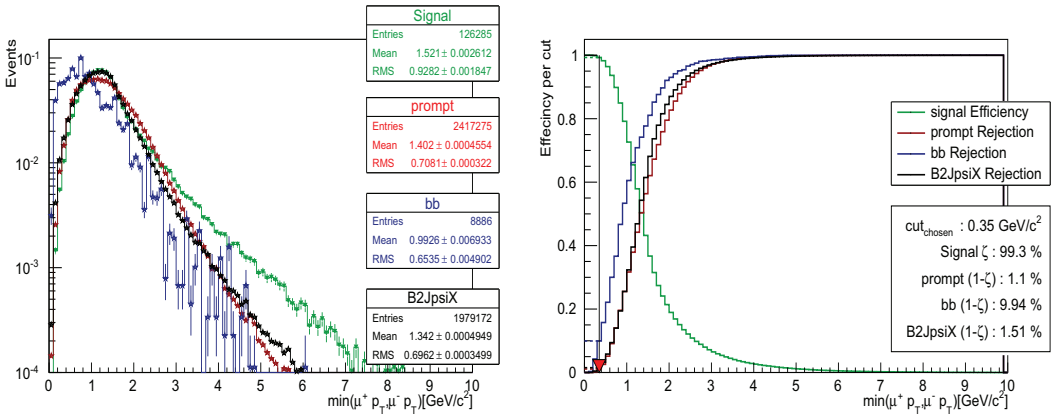

Figure 3.3: Left: minimum of muons' p_T distribution for $B_s^0 \to J/\psi\phi$ signal candidates (green), $b\bar{b}$ inclusive candidates (blue), $B_{u,d,s} \to J/\psi X$ candidates (black), and prompt inclusive J/ψ candidates. Right: signal efficiency and individual background rejection ratios per cut.

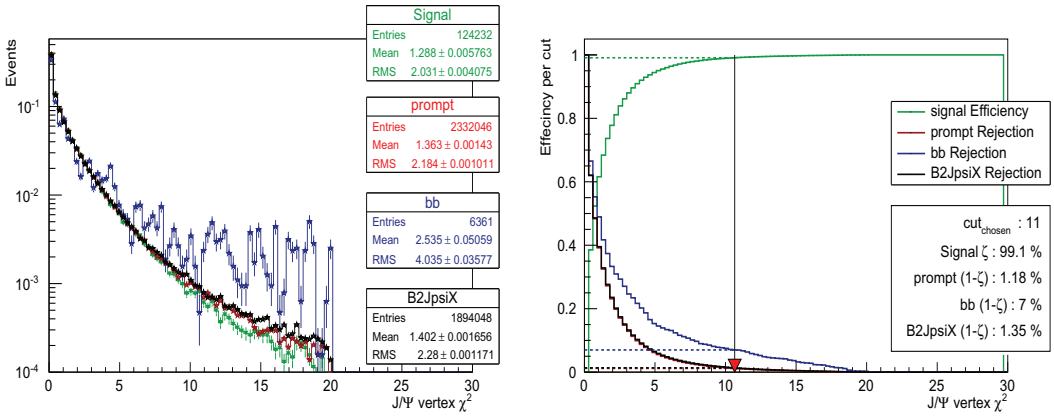

Figure 3.4: Left:J/ψ vertex χ^2/nDoF distribution for $B_s^0 \to J/\psi\phi$ signal candidates (green), $b\bar{b}$ inclusive candidates (blue), $B_{u,d,s} \to J/\psi X$ candidates (black), and prompt inclusive J/ψ candidates. Right: signal efficiency and individual background rejection ratios per cut. the best cut chosen is, $\chi^2_{\text{vertex}}/\text{nDoF} < 11$.

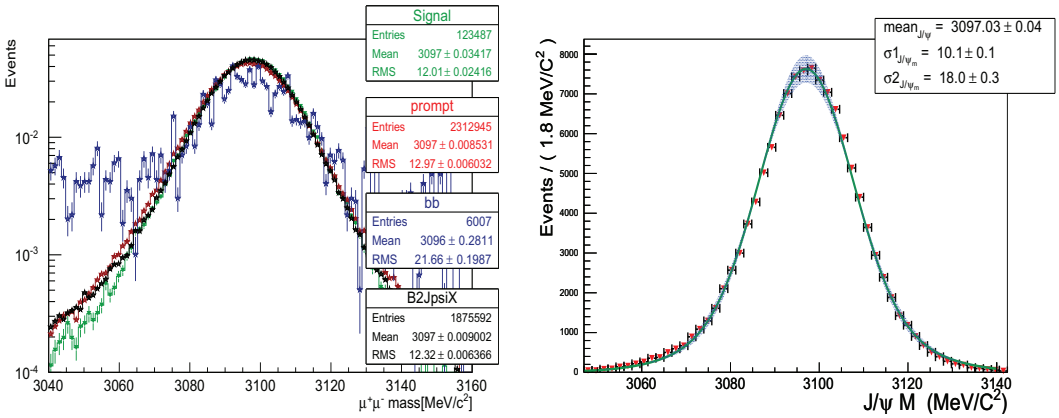

Figure 3.5: Left: J/ψ mass distribution for $B_s^0 \rightarrow J/\psi\phi$ signal events (green), $b\bar{b}$ inclusive candidates (blue), $B_{u,d,s} \rightarrow J/\psi X$ candidates (black). Right: mass distribution for signal events fitted with two Gaussian.

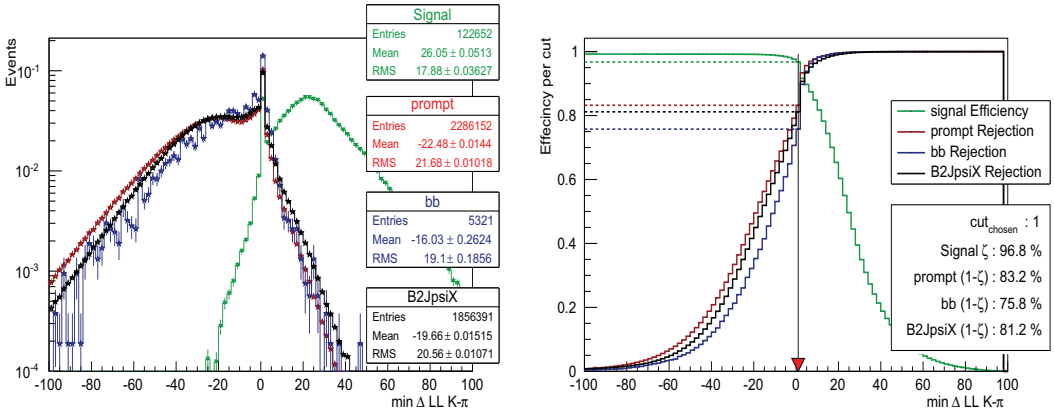

Figure 3.6: Left: minimum of kaons $\Delta \ln \mathcal{L}_{K\pi}$ distribution for $B_s^0 \to J/\psi\phi$ signal candidates (green), $b\bar{b}$ inclusive candidates (blue), $B_{u,d,s} \to J/\psi X$ candidates (black), and prompt inclusive J/ψ candidates. Right: signal efficiency and individual background rejection ratios per cut (peak at zero is due to the particle momentum being below the RICH threshold).

3.3.2 ϕ selection

Reconstruction of ϕ candidates is carried out using two kaons tracks, for events passing the J/ψ selection.To select the kaons, we use the global $\Delta \ln \mathcal{L}_{K\pi}$ using the RICH information. LHCb has an excellent kaon-pion separation. Using this nice advantage, the $b\bar{b}$ background is reduced by 75% with 3% signal loss at $\Delta \ln \mathcal{L}_{\mu\pi} > 0$, see Figure 3.6.

The $\chi^2_{\text{track}}/\text{nDoF}$ distribution is shown in Figure 3.7. The cut chosen by the selection criterion is too tight $\chi^2_{\text{track}}/\text{nDoF} > 1.6$. We choose a looser one $\chi^2_{\text{track}}/\text{nDoF} > 4$, since lower performance is expected with first data. We observe that this cut is efficient against the ghost rate in signal sample. The ghost reduction for this cut alone is $(43.6 \pm 0.6)\%$.

After passing these cuts, the kaons are being vertexed to form the ϕ particle. A cut on the ϕ vertex quality is applied requring it to be less than 11, as shown in Figure 3.9. The cut on its transverse momentum, $p_T > 1\,\text{GeV}/c^2$, is most powerful against the $b\bar{b}$ background, as shown in the Figure 3.8. This removes the contribution from low p_T background coming from primary vertex.

The invariant mass of the two kaons should be within 3σ of the nominal ϕ mass. This mass is shown in Figure 3.10 (right), fitted with a Voigtian distribution (a Breit-Wigner convoluted with a Gaussian) which takes into account the theoretical mass width and the detector resolution of a reso-

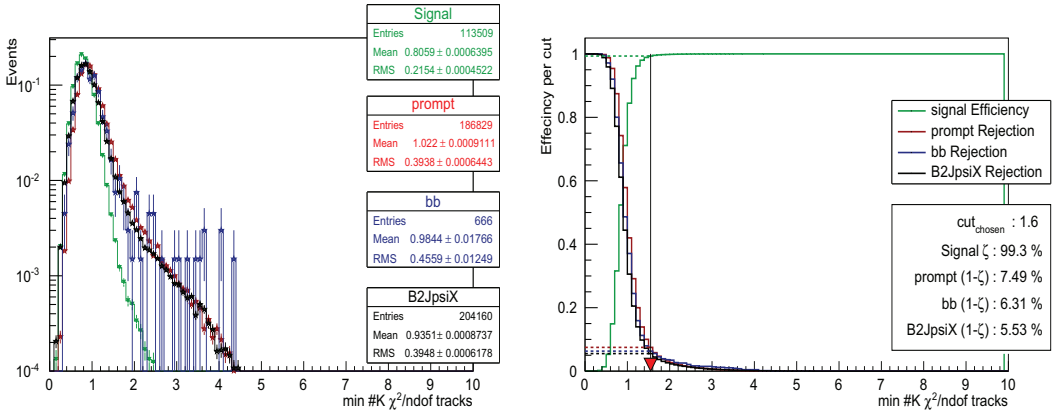

Figure 3.7: maximum of Kaons' tracks' χ^2_{track}/nDoF distribution for $B^0_s \rightarrow J/\psi\phi$ signal candidates (green), $b\bar{b}$ inclusive candidates (blue), $B_{u,d,s} \rightarrow J/\psi X$ candidates (black), and prompt inclusive J/ψ candidates. Right: signal efficiency and individual background rejection ratios per cut.

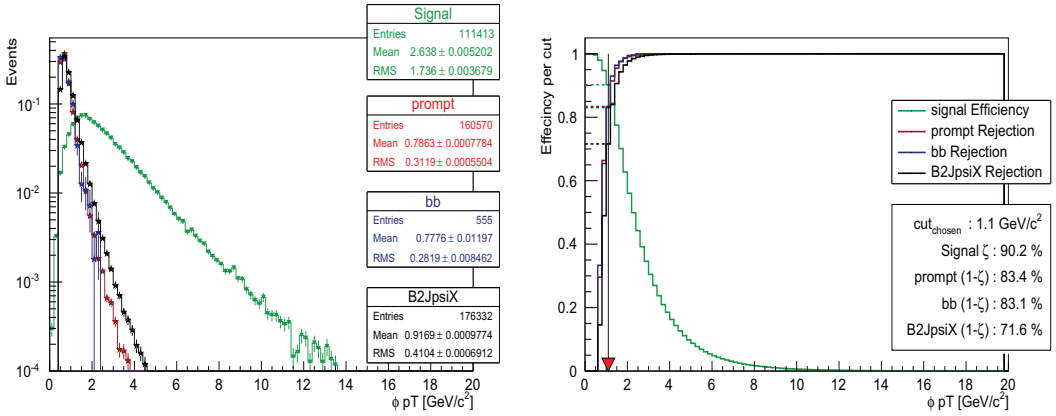

Figure 3.8: Left:ϕ p_{T} distribution for $B^0_s \rightarrow J/\psi\phi$ signal candidates (green), $b\bar{b}$ inclusive candidates (blue), $B_{u,d,s} \rightarrow J/\psi X$ candidates (black), and prompt inclusive J/ψ candidates. Right: signal efficiency and individual background rejection ratios per cut.

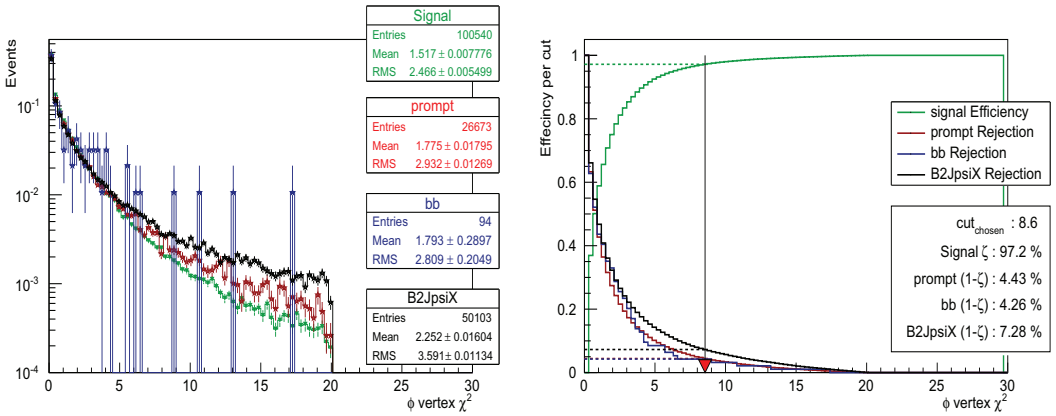

Figure 3.9: Left: ϕ vertex χ^2/nDoF distribution for $B_s^0 \to J/\psi\phi$ signal candidates (green), $b\bar{b}$ inclusive candidates (blue), $B_{u,d,s} \to J/\psi X$ candidates (black), and prompt inclusive J/ψ candidates. Right: signal efficiency and individual background rejection ratios per cut.

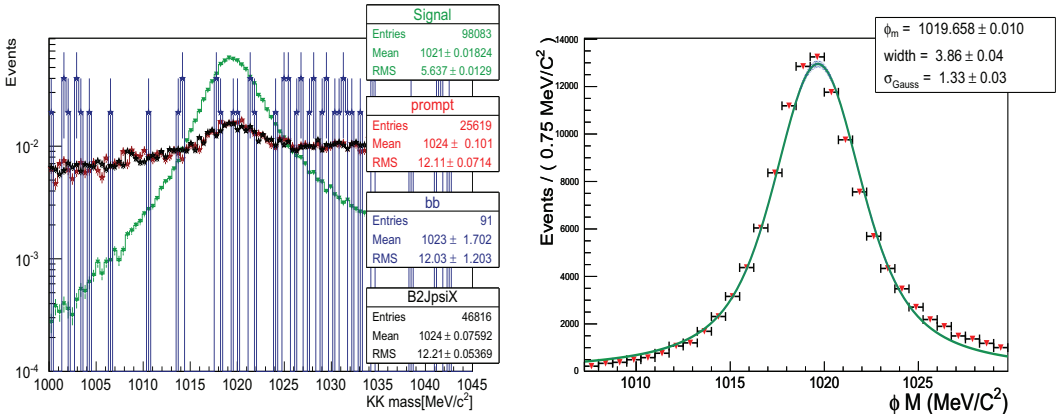

Figure 3.10: Left: ϕ mass distribution for signal sample (green), $b\bar{b}$ inclusive candidates (blue), $B_{u,d,s} \to J/\psi X$ candidates (black), and prompt inclusive J/ψ candidates. Right: ϕ mass distribution in the signal sample fitted with a Voigitian.

nance:

$$\frac{1}{(m - M_\phi)^2 + \frac{1}{4}\Gamma^2} \otimes \text{Gauss}(m, \sigma, M_\phi). \quad (3.2)$$

in this equation Γ is the resonance width, σ the detector resolution, M_ϕ is the mass of the resonance. The resolution used for the cut is the effective resolution of the Gaussian and the naturral particle width which is $\sim 4\,\text{MeV}/c^2$.

The efficiency of the ϕ cuts combined, defined as the ratio of the events passing all cuts to those passing the preselection cuts, is : $\varepsilon_{\text{sel}} = (69.1 \pm 0.1)\%$. where the input number of events is those passing the preselection cuts and the J/ψ selection.

3.3.3 B_s^0 selection

The J/ψ and ϕ candidates, which pass the previous sets of cuts, are being vertexed creating the B_s^0 particle. $\chi^2_{\text{vtx}}/\text{nDoF} < 5$, the cut is applied on B_s^0 vertex reducing by 12.3% the remaining $b\bar{b}$ background. Figure 3.11 shows the B_s^0 vertex χ^2/nDoF distributions for signal and background samples.

In the absence of p_T cuts, background with low momentum tracks with large multiple-scattering angle is present in the sample. This background can be removed using the criterion on the significance of minimal impact parameter of the B_s^0 particle with respect to the primary vertex. Figure 3.3.3 shows the distributions of this cut for signal and background samples. The efficiency of the B_s^0 cuts combined, defined as the ratio of events passing all cuts to those passing the preselection cuts, is: $\varepsilon_{\text{sel}} = (97.1 \pm 0.05)\%$, where the input number of events is those passing the preselection, J/ψ selection and ϕ selection.

It is worth mentioning that, before applying these two primary vertexes related cuts, the primary vertex position is recalculated in a process called primary vertex re-fitting [87], where the primary vertex is refitted after removing selected signal tracks (muons and kaons). This procedure is important for the analysis, because the primary vertex position would lean toward the secondary vertex if such re-fitting is not applied. This would create a bias on the proper time distribution. The B_s^0 invariant mass cut is within $3\sigma_{\text{av}}$ from the PDG value of the B_s^0 mass, where σ_{av} is the average mass resolution for the B_s^0 particle. In Figure 3.13 the B_s^0 mass distribution is fitted with two Gaussains. When a J/ψ mass constraint is applied in the kinematic fit of the decay, the average mass resolution is $14.2\,\text{MeV}/c^2$.

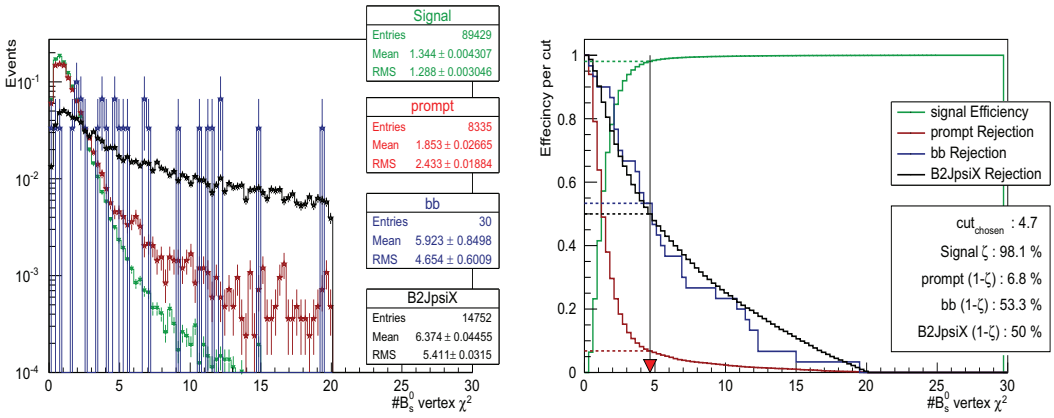

Figure 3.11: Left: B_s^0 vertex χ^2/nDoF distribution for $B_s^0 \to J/\psi\phi$ signal candidates (green), $b\bar{b}$ inclusive candidates (blue), $B_{u,d,s} \to J/\psi X$ candidates (black), and prompt inclusive J/ψ candidates. Right: signal efficiency and individual background rejection ratios per cut.

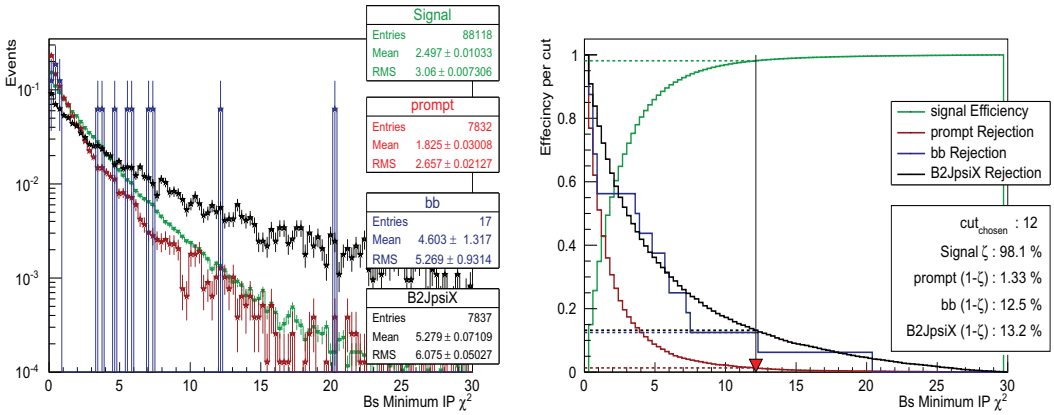

Figure 3.12: B_s^0 min IP χ^2 wrt primary vertex distribution for $B_s^0 \to J/\psi\phi$ signal candidates (green), $b\bar{b}$ inclusive candidates (blue), $B_{u,d,s} \to J/\psi X$ candidates (black), and prompt inclusive J/ψ candidates. Right: signal efficiency and individual background rejection ratios per cut. the best cut chosen is, min IP χ^2 wrt primary vertex > 12.

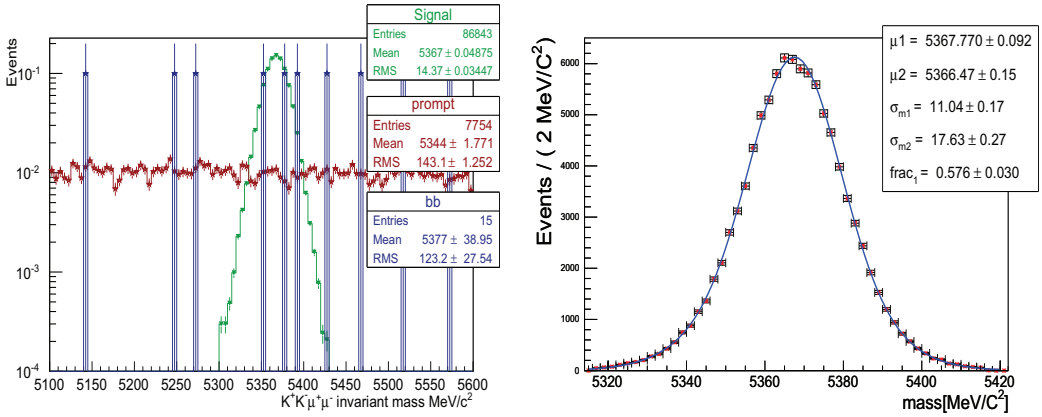

Figure 3.13: Left: mass distribution for $B_s^0 \to J/\psi\phi$ signal candidates (green), $b\bar{b}$ inclusive candidates (blue), $B_{u,d,s} \to J/\psi X$ candidates (black), and prompt inclusive J/ψ candidates. Right: mass resolution for signal events after, the average resolution is $\sim 15\,\mathrm{MeV}/c^2$, no constraint on the J/ψ mass was applied for this plot

Some events have more than one selected candidate. In such events, the candidate with the smallest $\chi^2_{\mathrm{vtx}}/\mathrm{nDoF}(B_s^0)$ is kept. Figure 3.14 shows the distribution of the number of candidates per event. The average is 1.1 which is 10 times smaller than the number before any selection (same Figure left). Table 3.5 summarizes all the cuts applied to the $B_s^0 \to J/\psi\phi$ channel. The detailed performance of this set of cuts is studied in the following section. This concludes the first part of this Chapter, the optimization procedure using the Monte Carlo samples.

3.3.4 Signal studies

In this section, the signal yield, proper time and angular resolution models and acceptance functions are reviewed using the sets of cuts shown in the Table 3.5. The Monte Carlo sample passes a trigger and stripping scenario applied to the data during the real data taking in 2010. This is to assure a minimal discrepancies between data and Monte Carlo samples, and to facilitate the comparison between the two.

Yield

The equation used to calculate the yield is:

$$\mathcal{Y} = \mathcal{L}_{\mathrm{int}} \times \sigma_{b\bar{b}} \times 2 \times f_s \times \mathrm{BR}_{\mathrm{vis}} \times \varepsilon_{\mathrm{tot}}\,, \tag{3.3}$$

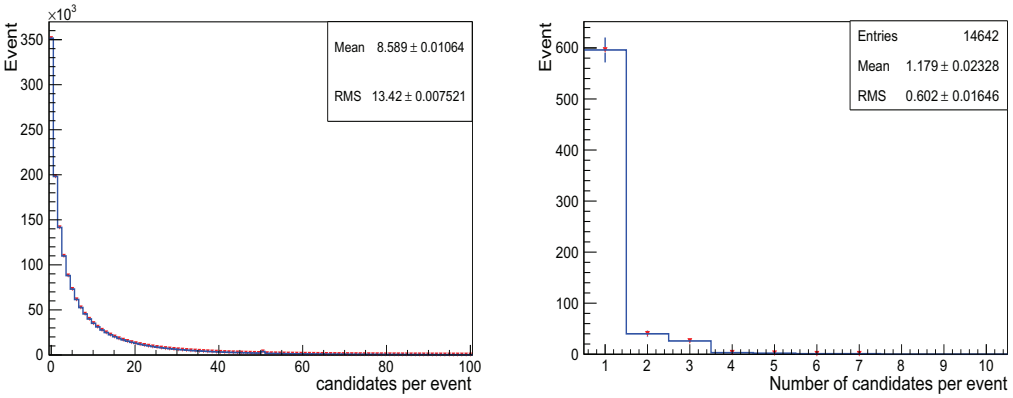

Figure 3.14: Left: number of candidates per event in the signal sample, after the *preselection* cuts (left) and event after applying *offline selection* cuts (right).

Decay mode	Cuts
$J/\psi \to \mu^+\mu^-$	$\Delta \ln \mathcal{L}_{\mu\pi} > 0$ muons $\chi^2_{\text{track}}/\text{nDoF} < 4$ $p_T(\mu^+)$ and $p_T(\mu^-) > 350\,\text{MeV}/c$ $\chi^2_{\text{vtx}}/\text{nDoF}(J/\psi) < 11$
	$\lvert M(\mu\mu) - M(J/\psi)\rvert/\sigma_{m_{J/\psi}} < 1.4 \times 3$
$\phi \to K^+K^-$	$\Delta \ln \mathcal{L}_{K\pi} > 0$ kaons $\chi^2_{\text{track}}/\text{nDoF} < 4$ $\chi^2_{\text{vtx}}/\text{nDoF}(\phi) < 9$ $p_T(\phi)$ 1 GeV/c $\lvert M(K^+K^-) - M(\phi)\rvert < \pm 12\,\text{MeV}/c^2$
$B_s^0 \to J/\psi\phi$	$\chi^2_{\text{vtx}}/\text{nDoF} < 5$ B_s^0 min IP χ^2 wrt primary vertex < 20
	$\lvert M(B_s^0) - M(J/\psi\phi)\rvert < \pm 50\,\text{MeV}/c^2$

Table 3.5: Summary of the cuts developed in the unbiased analysis, applied to the $B_s^0 \to J/\psi\phi$ channel.

where $\mathcal{L}_{\rm int}$ is the integrated luminosity, $\sigma_{b\bar{b}}$ is the cross section of $pp \to b\bar{b}X$, f_s is the fragmentatio fraction to B_s^0, BR_{vis} the visible branching ratio of the $B_s^0 \to J/\psi\phi$ channel, and ε_{tot} the total selection efficiency. The latter is given by:

$$\varepsilon_{tot} = \varepsilon_{gen} \times \varepsilon_{reco+presel} \times \varepsilon_{sel} \times \varepsilon_{trig} \,. \tag{3.4}$$

where ε_{gen}, $\varepsilon_{reco+presel}$, ε_{sel} are generator level efficiency, reconstruction and preselction combined efficiency and offline efficiency. ε_{trig} is the trigger efficiency and is composed of sub-efficiencies itself due to the trigger architecture explained in Chapter 2. As stated there, the set of proper time unbiased triggers applied on 2010 data are:

- Hlt1SingleMuonNoIP confirmed by L0Muon, and Hlt1DiMuonNoIP confirmed by L0DiMuon;
- Hlt2UnbiasedJPsi.

The trigger in LHCb could be fired by signal-related elements (tracks, composite particles), this is called TOS (Trigger On Signal). Alternately, the trigger could be fired by elements which are not signal-related that passed the trigger lines cut (some track from primary vertex, a muon from the other B in the event, etc ...). For the unbiased analysis, we limit ourselves to the unbiased TOS triggers, that will guarantee that the signal tracks are selected in lifetime-unbiased way. Combining these information all together gives a trigger efficiency of:

$$\varepsilon_{trigger} = \varepsilon_{HLT1} \times \varepsilon_{HLT2} = (57.3 \pm 0.1)\% \,. \tag{3.5}$$

With $\mathcal{L}_{\rm int} = 2\,fb^{-1}$, $\sigma_{b\bar{b}} = (284 \pm 20 \pm 49)\mu b^{-1}$ measured in LHCb at 7 TeV [88], and replacing the rest by their values from Tables 3.1, 3.2, 3.3 in the yield:

$$\mathcal{Y} \simeq 60\,000 \text{ events} \,. \tag{3.6}$$

Scaled to $36\,pb^{-1}$, one finds: $\mathcal{Y} \simeq 1\,100$ events[6], In Section 3.4, we will see that this yield is compatible with that measured in 2010 data. The uncertainty on the yield is large ($\sim 4 \times 10^4$). This is due to the large uncertainty on the cross section of the $b\bar{b}$ quarks.

Mass, proper time resolution and proper time acceptance distributions

The distribution of the B_s^0 mass is given in Figure 3.15 (bottom). It is fit

[6] which is the luminosity collected in 2010.

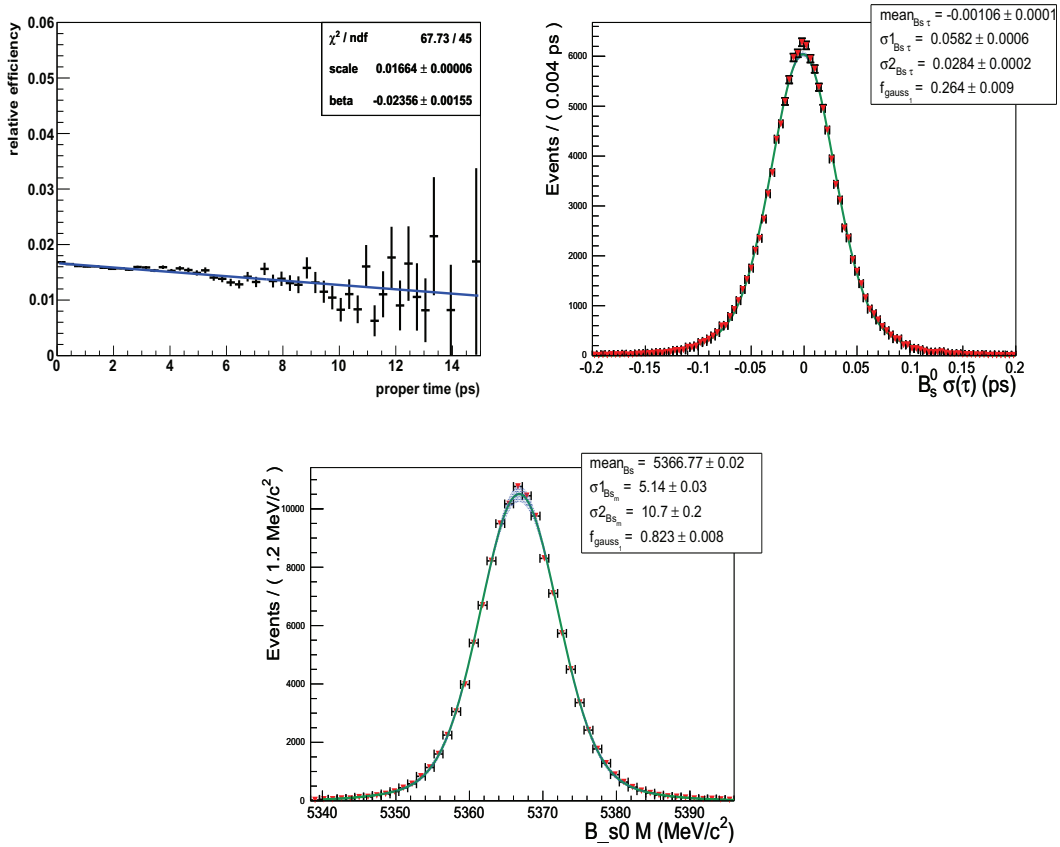

Figure 3.15: Left: reconstructed B_s^0 proper time acceptance. Right: B_s^0 proper time resolution calculated using the truth information $(t_{\text{rec}} - t_{\text{true}})$. Bottom: B_s^0 mass resolution after constraining the J/ψ mass to its PDG value (MC10).

using two Gaussian. The average mass resolution is calculated using the equation:

$$\begin{aligned} &\langle \sigma_m \rangle = \sqrt{f_{m,1} \times \sigma^2_{m,1} + (1 - f_{m,1}) \times \sigma^2_{m,2}} \\ &\text{where} \quad G_i = \frac{1}{\sqrt{2\pi}\sigma_{m,i}} \exp\left(-\frac{1}{2} \left(\frac{m - \mu_{m,i}}{\sigma_{m,i}} \right)^2 \right) \quad i = 1, 2 \end{aligned} \tag{3.7}$$

When applying the J/ψ mass constraint [89], the B_s^0 mass resolution decrease to 6.5 MeV/c^2, improving it by a factor 2. In the following we will consider the J/ψ mass constraint in all plots that we show, if not stated otherwise.

The B_s^0 reconstructed proper time t_{reco} is obtained from a kinematic fit, using Lagrange multipliers to apply the constraint that the B_s^0 momentum originates from the re-fitted primary vertex [90]. The proper time resolution is defined as the average width of the Gaussians fitted to the distribution $\langle \sigma_m \rangle = t_{\text{reco}} - t_{\text{true}}$ shown in Figure 3.15 (centre), where t_{true} is the true proper time. The average proper time resolution, calculated using Equation 3.7 is 39 fs.

The proper time acceptance is shown in the Figure 3.15 (left). It is calculated by dividing the reconstructed proper time distribution by the theoretical expectation. The acceptance is almost flat conforming with the absence of biased cuts in the selection. However, we observe a slight decrease of efficiency at high values of proper time. One possible explanation [91] is related to the VELO acceptance, where reconstruction efficiency decreases with the decay length. Some events with higher decay length would likely be missed. We checked this hypothesis and found it to be partially true when asking the four decay product to be within the VELO acceptance. Work is still in progress to check this hypothesis.

Angular variables resolution and acceptance In Figures 3.16 we show the distributions of the three angles in the transversity basis for selected signal events. On the same plot, we show the projections of the theoretical decay rate onto each one of the angular variables. The angles are calculated using the equations in Chapter 1.

In Figures 3.17, we show the acceptances obtained by dividing the true angular distributions by the theoretical expectation. The distortions observed are mostly due to the unique geometrical acceptance of the detector and partly to the reconstruction and our selection cuts. The individual effect of each of these elements are described here [85]. The distortions are found to be less than 10%. The effect of these distortions on the

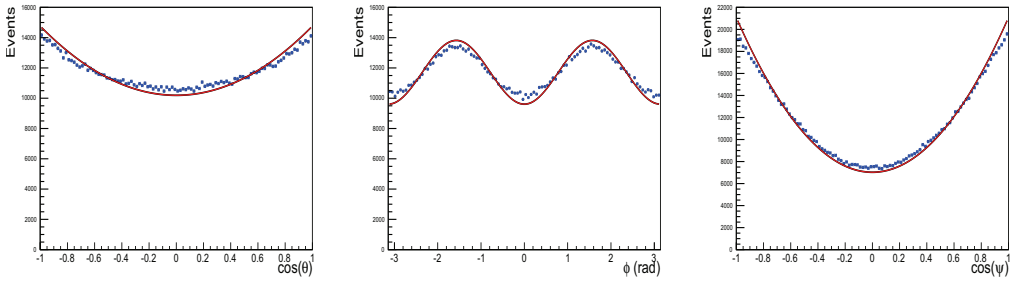

Figure 3.16: Distribution of angular variables, from left to right $cos(\theta), \phi$ and $cos(\psi)$. The red line is the projection of the theoretical differential decay rate, where the data points are the reconstructed angular variables (MC10).

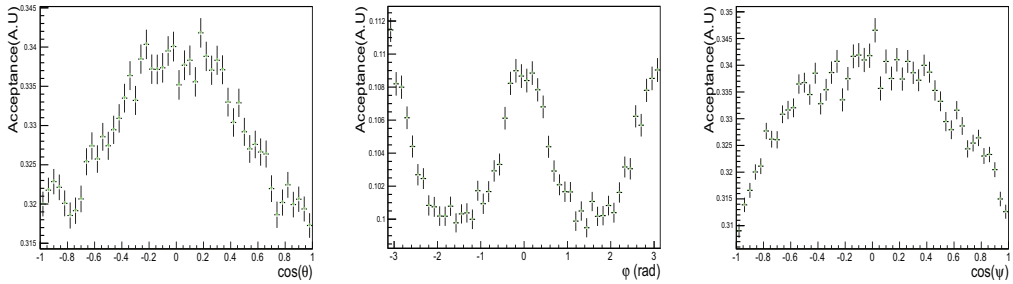

Figure 3.17: 1 D projection of acceptance of the angular variables, from left to right $cos(\theta), \phi$ and $cos(\psi)$. The projection of the theoretical differential decay rate onto variable plane where used (MC10).

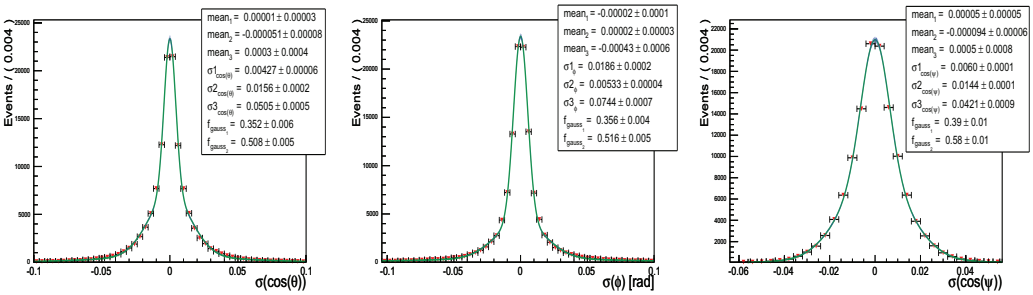

Figure 3.18: Distributions of angular variables resolution, Left:distribution of $cos(\theta)$ resolution where $\langle\sigma_{cos(\theta)}\rangle = 0.022$. Center:distribution of ϕ resolution, where $\langle\sigma_{\phi}\rangle = 0.029$ rad. Right:distribution of $cos(\psi)$ resolution where $\langle\sigma_{cos(\psi)}\rangle = 0.014$ (MC10).

fitted physical parameters is not negligible if not properly taken into account [5]. These distortions could be evaluated from the simulation, and cross checked in the $B^0_d \rightarrow J/\psi K^{*0}$ control sample. The angular resolutions fitted by the the sum of three Gaussian are shown in Figure 3.18.
Table 3.6 shows a summary of the angular variables average resolution

Angular variable	Resolution mrad	Acceptance distortion %
$\cos\theta$	22.4 ± 0.1	8 ± 1
ϕ rad	29.2 ± 0.1	7 ± 1
$\cos\psi$	14.5 ± 0.1	9 ± 1

Table 3.6: Summary of the angular resolution (column 2) and the acceptance distortions(column 3) for the angular variables $\cos(\theta), \cos(\phi)$ and $\cos(\psi)$.

and their acceptance distortions which are defined as: $(x_{\max} - x_{\min})/x_{\max}$, here $x_{\max(\min)}$ are the maximum (minimum) bin the acceptance distribution of the angular variable x.

3.3.5 Background studies

In this section we identify the main sources of the background with the help of Monte Carlo samples. Understanding the shapes of their proper time and angular distributions is a crucial point for the analysis, as ϕ_s is extracted from a fit of the tagged time-dependent angular distributions.

We distinguish two main types of background component:

- a prompt component of events having zero true proper time. We use the inclusive J/ψ sample to study this component. This is done by explicitly removing pp $\rightarrow$ b $\Rightarrow$ J/ψ from this sample along with the signal events;

- a long-lived component of events having a non-zero true proper time, due to a true b-particle. We use two samples to account for this background. The first is $B_{u,d,s} \rightarrow J/\psi X$ to study the angular and proper time distributions. Those samples are more abundant, after applying offline cuts, and most dangerous because of their signal-like properties. The second is inclusive $b\bar{b}$. This background is more general since more b-decays are included. Therefore it is more suitable for the calculation of the background to signal ratio. However, the sample surviving the offline cuts is not statistically sufficient to study its proper time and angular properties.

In the following, we detail both types using the simulation samples mentioned in Table 3.1.

Prompt background

This is the first type of background and the least dangerous, because of its proper time distribution is expected to be Gaussian-like centered around zero. Indeed the Figure 3.19 (right) shows the proper time distribution for the prompt events fitted with one Gaussian with $\sigma = 34$ fs. Because prompt events have zero lifetime, the σ represents the pure detector resolution. This is a useful information to extract the proper time resolution for our signal events.

The mass distribution, shown in Figure 3.19 (right), is fitted with a sum of decreasing exponential (background) and a Gaussian (signal). No mass peak is observed for this background.

Figure 3.20, shows the angular distribution for the prompt background. Because of its combinatorial nature, no unique pattern is found for this type of background (within the available statistics).

The calculation of background-to-signal ratio uses the following equation:

$$\frac{B_{\rm Pr}}{S} = \frac{\sigma_{\rm Pr} \times BR(J/\psi \rightarrow \mu\mu) \times \varepsilon_{\rm Pr} \times f_{\rm MW}}{2 \times \sigma_{b\bar{b}} \times f_s \times \mathcal{B}_{\rm vis} \times \varepsilon_{\rm tot}} = 2.6 \pm 0.6\,, \qquad (3.8)$$

where $\sigma_{\rm Pr}$ is the cross-section pp $\rightarrow$ J/ψX given in Table 3.2, $\varepsilon_{\rm Pr}$ is the selection efficiency for the prompt component in the $\pm 300\,{\rm MeV}/c^2$ mass window, $f_{\rm MW}$ is a scale factor needed to pass from $\pm 300\,{\rm MeV}/c^2$ to the

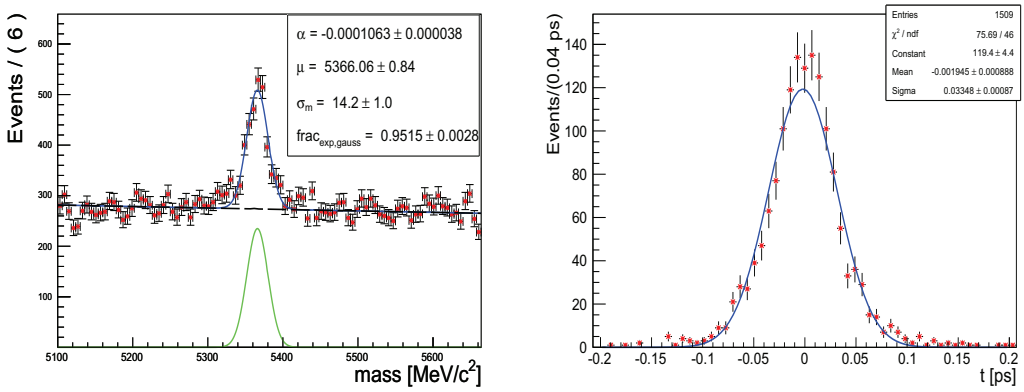

Figure 3.19: Mass distribution for prompt inclusive J/ψ (left), and its proper time distribution (right) (MC10).

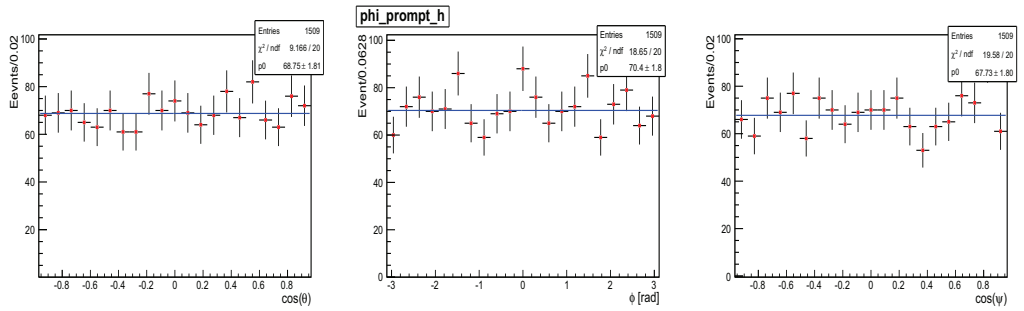

Figure 3.20: Angular distributions for prompt inclusive J/ψ background (MC10).

$\pm 50\,\mathrm{MeV}/c^2$ mass window[7] and $\varepsilon_{\mathrm{tot}}$ is the total efficiency for the signal. The f_s is the weakly decaying fraction for b $\rightarrow$ B_s, $\mathcal{B}_{\mathrm{vis}}$ is the visible branching fraction for the signal channel (given in Table 3.3).

Naturally B/S for the prompt background is high due to the nature of selection, where cuts on vertex, impact parameter are not used.

Long-lived background

This is the most dangerous background, since its decays have a true b content, making the proper time distribution more signal-like. This can compromise the separation power when fitting for physical signal parameters. The distribution of this background's proper time is shown in Figure 3.21 (right). This distribution is fitted with two exponentials convoluted

[7] assuming linear mass distribution.

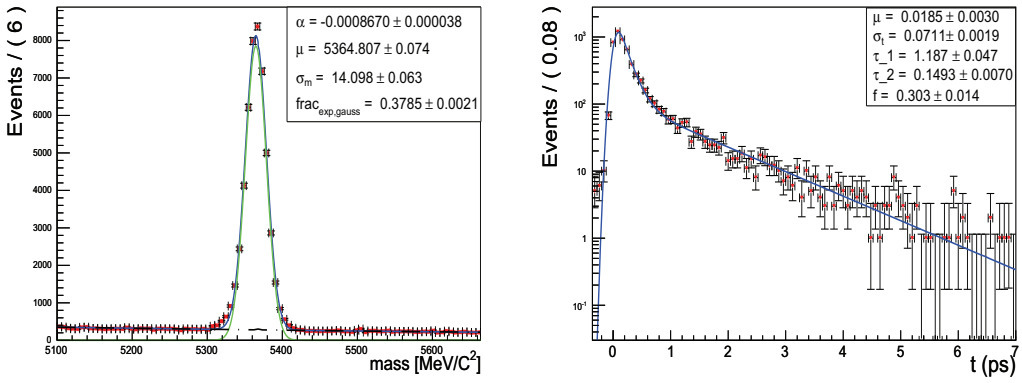

Figure 3.21: Mass distribution (left) for prompt inclusive J/ψ , and its proper time distribution (right) (MC10).

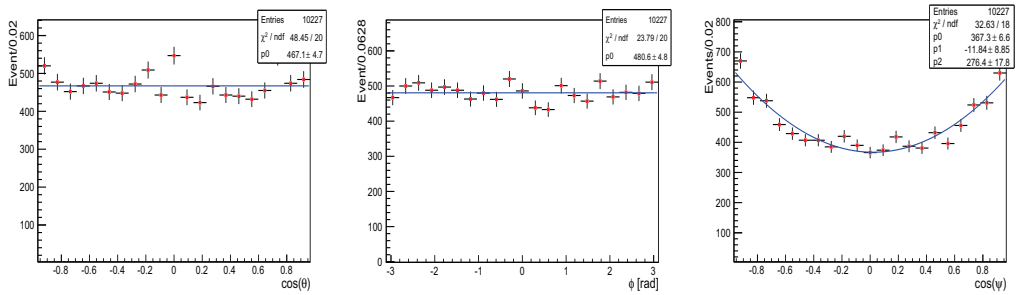

Figure 3.22: Angular distributions for $B_{u,d,s} \rightarrow J/\psi X$ background (MC10).

with a single Gaussian with $\sigma_t^{LL} = 71$ fs, the proper time distribution for this type of background is dominated by a short-decay exponential with $\tau_1^{LL} = 0.15$ ps, while the remaining component is a long-decay exponential with $\tau_2^{LL} = 1.2$ ps.

Figure 3.21 (left) shows also the mass distribution for selected events in this samples, where a decreasing exponential accounts for the background mass.

The angular distribution for the long-lived background events is shown in Figure 3.22. While $cos(\theta)$ and ϕ_s distributions are flat, it is clear that there is some structure, specially in the case of $cos(\psi)$ distribution, where the data points were fitted with second degree polynomial. This structure is due to the signal-like phenomenology of this type of background.

Background-to-signal rate is calculated using the following equation:

$$B_{\mathrm{LL}}/S = \frac{\varepsilon_{\mathrm{sel,b\bar{b}}}}{2 \times f_s \times \mathcal{B}_{\mathrm{vis}} \times \varepsilon_{\mathrm{tot}}} = 0.28 \pm 0.14\,, \tag{3.9}$$

where $\varepsilon_{\text{sel},b\bar{b}}$ is the selection efficiency in the $b\bar{b}$ sample after removing the signal events.

In the following, we summarize all our results in Table 3.7. This summary table will be the baseline for our toy Monte Carlo studies presented in Chapter 5. The tagging parameters are discussed in Chapter 4.

Parameter	Signal	Prompt background (Pr)	Long-lived background (LL)
Events in B_s^0 mass window $\pm 24\,\mathrm{MeV}/c^2$ (fractions, B/S)	60 k (25.7%)	156 k (66.9%, $B_{\mathrm{Pr}}/S = 2.6$)	16.8 k (7.3%, $B_{\mathrm{LL}}/S = 0.3$)
Mass m (MeV/c^2)	2 Gauss; $f^{\mathrm{s}}_{m,1} = 0.82$; $\sigma^{\mathrm{s}}_{m,1} = 5.2$; $\sigma^{\mathrm{s}}_{m,2} = 10.7$	$\mathrm{Exp}(-\alpha^{\mathrm{Pr}}_m m)$; $\alpha^{\mathrm{Pr}}_m = 0.0001$	$\mathrm{Exp}(-\alpha^{\mathrm{LL}}_m m)$; $\alpha^{\mathrm{LL}}_m = 0.0009$
Proper time t (fs)	Signal PDF $\otimes$ 2 Gauss; $f^{\mathrm{s}}_{t,1} = 0.27$; $\mu^{\mathrm{s}}_{t,1} = 0$; $\sigma^{\mathrm{s}}_{t,1} = 58.2$; $\mu^{\mathrm{s}}_{t,2} = 0$; $\sigma^{\mathrm{s}}_{t,2} = 28.4$	$\delta(t) \otimes$ 1 Gauss; $\mu^{\mathrm{Pr}}_t = 0$; $\sigma^{\mathrm{Pr}}_t = 34$	2 Exponentials $\otimes$ 1 Gauss; $f^{\mathrm{LL}}_{\tau_1} = 0.3$; $\tau^{\mathrm{LL}}_1 = 1187$, $\tau^{\mathrm{LL}}_{t,2} = 149$; $\mu^{\mathrm{LL}}_t = 0$; $\sigma^{\mathrm{LL}}_t = 71$
Angles	no acceptance flat background	no acceptance flat background	no acceptance flat background
Flavour tagging	$\varepsilon_{\mathrm{tag}} = 0.332$; $\omega = 0.306$	$\varepsilon^{\mathrm{Pr}}_{\mathrm{tag}} = 0.20$	$\varepsilon^{\mathrm{LL}}_{\mathrm{tag}} = 0.42$

Table 3.7: Summary of baseline detector input parameters for sensitivity studies with the *unbiased* cuts, extracted from full Monte Carlo. Flavour tagging performances are discussed in Chapter 4.

3.3.6 High pile-up impact on selection

In 2010 data taking, attempts to increase luminosity led to a specific configuration of the LHC machine, where the number of pp interactions per colliding bunch (ν) reached six times the LHCb design value creating a high"pile-up" environment. A Monte Carlo sample is generated with $\nu = 3$ and used for this study[8].

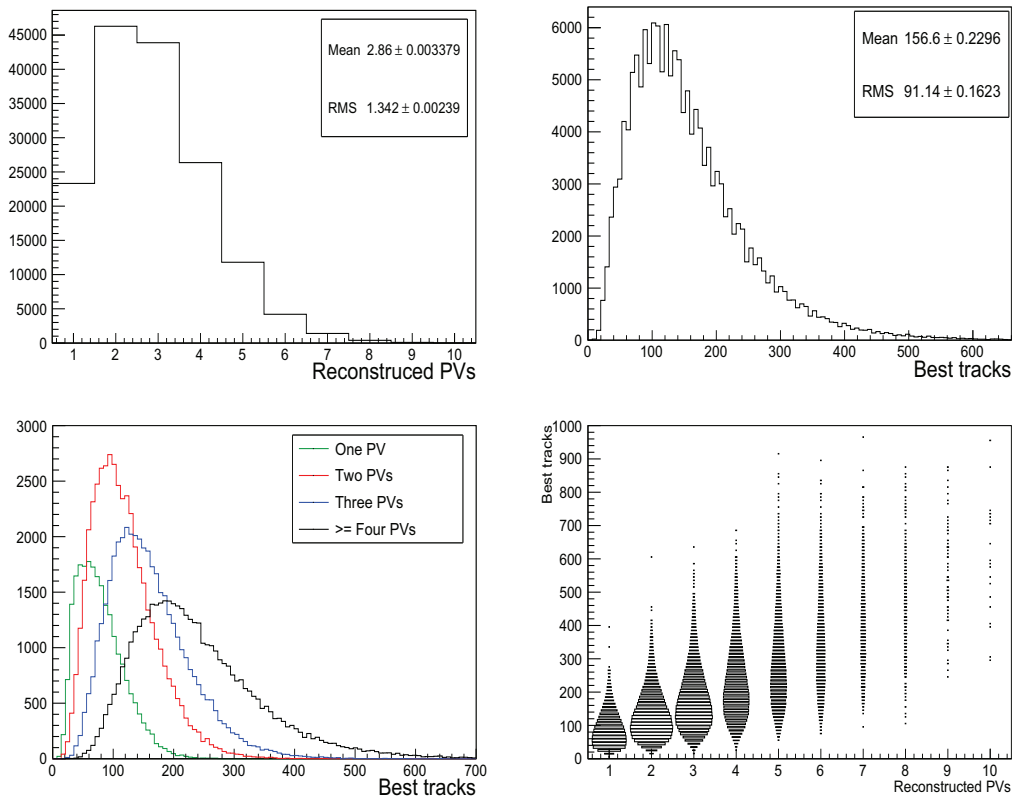

Figure 3.23: Top left: distribution of the number of reconstructed primary vertex per event. Top right: distribution of number of best tracks per event. Bottom left: distribution of best tracks number for events with one (green), two (red), three (blue), and more than three (black) primary vertexes per event. Bottom right: 2-D plot for number of best tracks versus number of reconstructed vertexes per event (MC2010).

Higher pile-up creates a difficult environment for the analysis, where the number of tracks and primary vertexes in the event increases. More

[8] /MC/2010/Beam3500GeV-VeloClosed-MagDown-Nu3/2010-Sim03Reco03-withTruth

events take longer to process during trigger and reconstruction. Moreover some tracks are matched with the wrong primary vertex.

In this section we study the effects of the high track multiplicity[9] on the proper time resolution, selection efficiency. Tagging properties are discussed in the tagging Chapter 4.

Plots in the Figure 3.23 (bottom) present the distribution of the number of tracks per primary vertex and the correlation between the primary vertex and their number of tracks. The number of tracks per event increases with the number of primary vertices reconstructed. The correlation between the two quantities implies that the best strategy to reduce the number of high occupancy events is to cut on track multiplicity rather than cutting on the number of reconstructed primary vertexes.

In second part of the study, we divide the sample into bins of track multiplicity and study the performance within those bins. We aim to study the trend when track multiplicity increases.

We show the distributions of the discriminating variables used during the selection in two bins of track multiplicity (first with < 150 and second bin with > 250). From the Figure 3.24 we see that muons and kaons tracks χ^2/nDoF depend on track multiplicity per events. The performance of this variable worsens for high track multiplicity events. This is due to reconstruction effects originating from increasing number of hits mismatched [93] to tracks resulting in worse track reconstruction. For the PID, better separation between muons and pions on one hand, and kaons and pions on the other hand are achieved for low track multiplicity. Increasing the number of tracks per events would result in higher pion background to muons and kaons tracks, making it more difficult to assign them with correct PID.

The discriminating variables of the J/ψ and ϕ particles show less dependence on track multiplicity than the muons and kaons, some degradation in B_s^0 vertex χ^2/nDoF distribution is observed as seen in Figure 3.25.

The degradations shown above lead to the fact that in higher track multiplicity one should expect a drop in signal efficiency. Indeed, when we calculate the signal efficiency in bins of track multiplicity ($> 150, 150 - 250, > 250$) we observe a clear drop with the increase of track multiplicity, see Figure 3.26 (left).

Concerning the proper time resolution, the Figure 3.26 shows a small degradation with the increase of track multiplicity in the event.

We can conclude then that: a clear drop of signal efficiency is observed

[9] track multiplicity refers here to the number of best tracks per event, where best tracks are all tracks in the event who passed the clone killer algorithm [92].

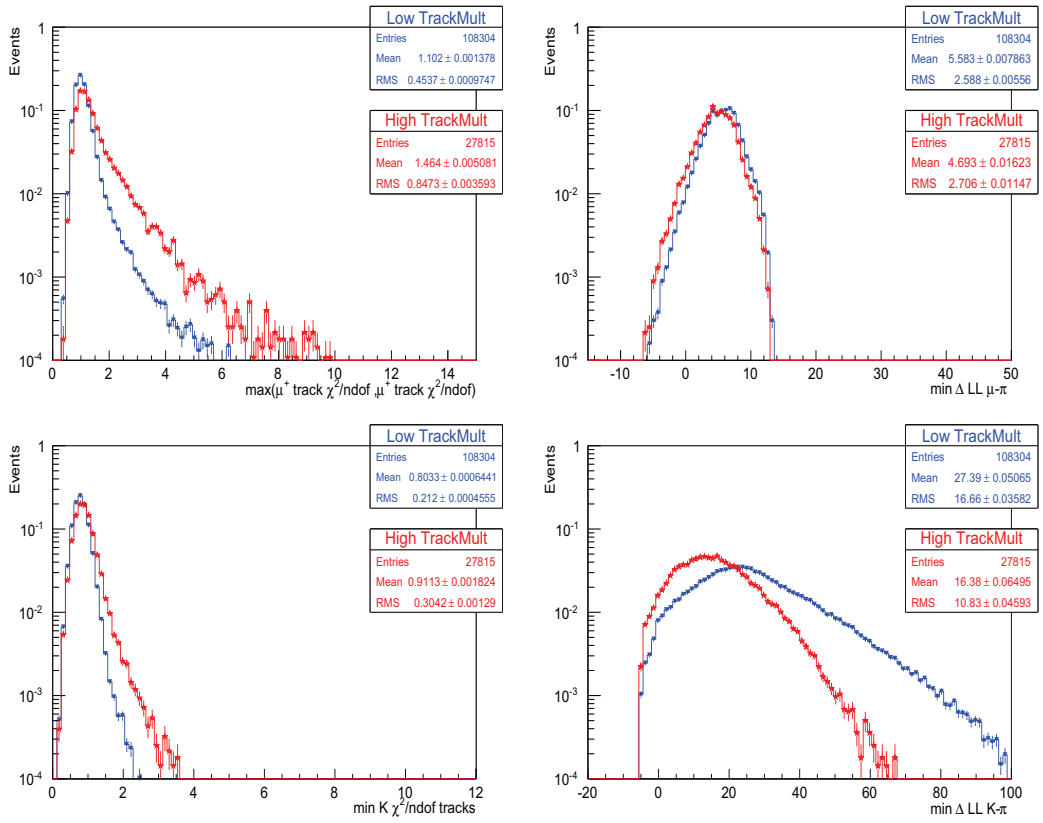

Figure 3.24: Maximum of χ^2_{track}/nDoF distribution (left). Minimum of muons $\Delta \ln \mathcal{L}_{\mu\pi}$ distribution (right). The top row is for muons and the bottom for kaon. High multiplicity variable distributions in red, low multiplicity distribution in blue (MC2010).

with the increase of number of tracks per event, this due to the degradation of PID and χ^2 variables , the proper time resolution is not affected by the increase of number of tracks per events.

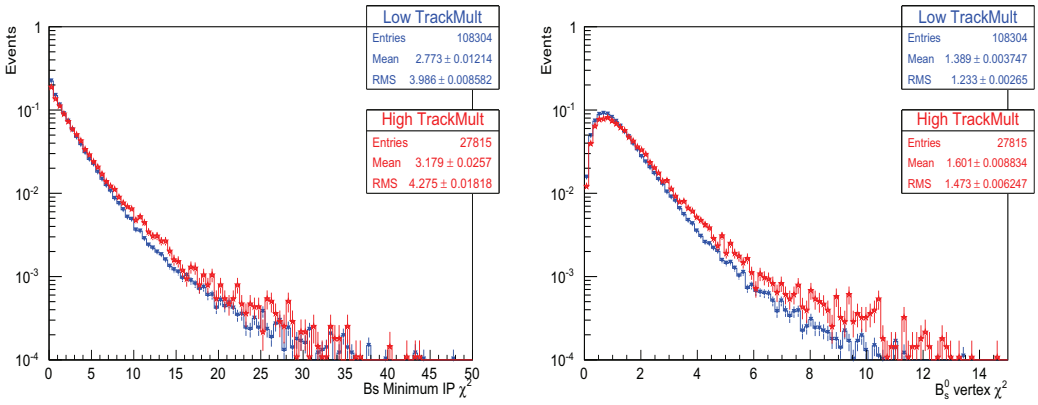

Figure 3.25: Left: distribution of B_s^0 min IP χ^2 wrt primary vertex for high track multiplicity (red), low track multiplicity (blue). Right: B_s^0 vertex χ^2/nDoF distribution for high track multiplicity (red), low track multiplicity (blue) (MC2010).

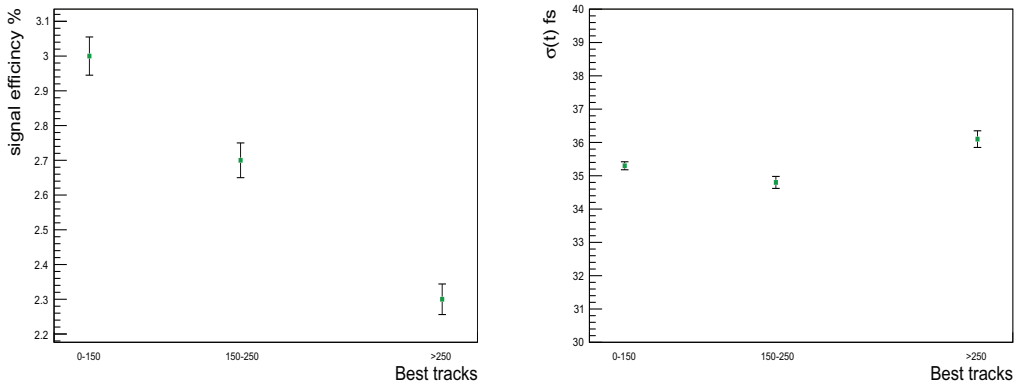

Figure 3.26: Left: graph shows signal efficiency versus track multiplicity per event. Right: a graph shows the proper time resolution versus track multiplicity per event (MC2010).

3.4 Selection performance with 2010 real data

In 2010 at LHC, data were taken at a center-of-mass energy $\sqrt{s} = 7\,\text{TeV}$. This was the first time a proton-proton collider achieved such energy. The corresponding integrated luminosity for this data is $\sim 36\,\text{pb}^{-1}$ with high pile-up environment.

The list of triggers applied to the data are presented in the Chapter 2. The unbiased trigger lines used for this analysis are Hlt1SingleMuonNoIP confirmed by L0Muon, and Hlt1DiMuonNoIP confirmed by L0DiMuon. The main feature of those lines is that they are fired mainly by muon objects and do not bias the proper time of the B_s^0. Events passing those lines are required to pass Hlt2UnbiasedJPsi line at the HLT2 level.

The sample surviving the trigger is then reconstructed with the reconstruction program BRUNEL v37r8p4 [63] and stripped with analysis software DaVinci v26r3 (Reco08-Stripping12) [94].

The data are then sent to dedicated trigger lines in the DiMuon stripping stream, where B candidates are further refined by applying final cuts. The cuts applied to select and refine the B_s^0 in $B_s^0 \to J/\psi\phi$ channel are those developed in this chapter and summarized in Table 3.5 with some minor changes explained below. Two additional cuts are motivated by the behavior of the background in data; details are found in [86]. A long negative tail is observed in the proper time distribution. For events with more than one primary vertex, the B_s^0 is sometimes being associated to the wrong primary vertex. As the primary vertex association is made according to a cut on the IP χ^2, a cut on the impact parameter χ^2 calculated to the *next* best primary vertex (χ^2 of *next* best primary vertex <50) is added to remove this tail. As mentioned before, a kinematic fit is performed using the DecayTreeFitter in order to calculate the proper time of the B_s^0 particle, and cutting on the χ^2 of this fit helps to obtain a high quality on B_s^0 candidates. This calculation of the proper time is made without the J/ψ mass constraint in order to reduce correlation between the proper time and the mass of the B_s^0. This facilitates the study of the proper time of the background in the mass sidebands ofthe B_s^0.

Concerning the values of the cuts, an optimization study [95] was carried out on the 2010 data. This study confirmed the validity of our cuts with only minor changes to the selection, where the $\chi^2_{\text{vtx}}/\text{nDoF}$ of the ϕ and the B_s^0 are loosened.

The reconstructed mass and proper time projections for the candidates passing unbiased offline $B_s^0 \to J/\psi\phi$, is shown in Figure 3.27, along with the proper time distribution for these candidates. A two-dimensional un-

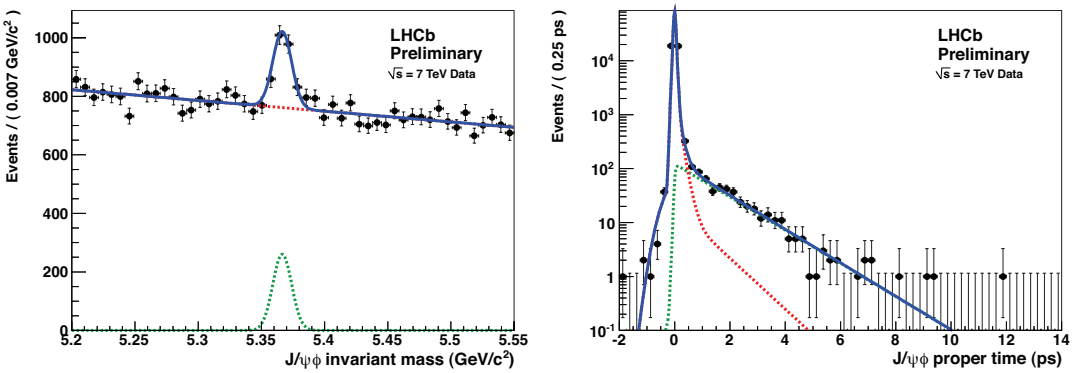

Figure 3.27: B_s^0 mass (left) and proper time (right) projections of the two-dimensional fit to $B_s^0 \to J/\psi\phi$ candidates. The total fit is represented by the blue solid line, the signal contribution by the green dashed line and the background contribution by the red dashed line. The mass range for the fit is $[5.20, 5.55]$ GeV/c^2 [86].

binned maximum likelihood fit to the mass and the proper time distributions is performed in order to extract the B_s^0 effective lifetime.

$$\mathcal{P}_{\text{sig}} = \text{Acc}(t_{\text{true}}) \times \frac{1}{\tau}\exp(\frac{-t_{\text{true}}}{\tau}) \times \text{Pdf}_{\text{mass}}. \tag{3.10}$$

The time part of this fit is a function shown in Equation 3.10, where an simplified single-sided exponential, describing the true proper time distribution for B_s^0 signal candidates, is corrected with an acceptance function. This is to take into account effects seen in Figure 3.15. $\tau_{B_s^0}^{single}$ is the effective lifetime of B_s^0 and is given by:

$$\tau_{B_s^0}^{single} = \frac{A\tau_H^2 + B\tau_L^2}{A\tau_H + B\tau_L} \tag{3.11}$$

with:

$$\begin{aligned} A &= \left((1-\cos\phi_s)\frac{|A_0(0)|^2}{2} + (1-\cos\phi_s)\frac{|A_\parallel(0)|^2}{2} + (1+\cos\phi_s)\frac{|A_\perp(0)|^2}{2}\right), \\ B &= \left((1+\cos\phi_s)\frac{|A_0(0)|^2}{2} + (1+\cos\phi_s)\frac{|A_\parallel(0)|^2}{2} + (1-\cos\phi_s)\frac{|A_\perp(0)|^2}{2}\right) \end{aligned} \tag{3.12}$$

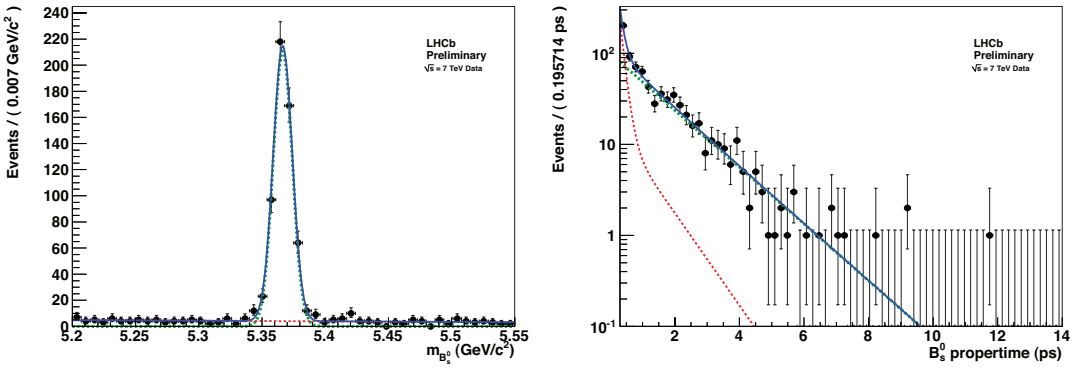

Figure 3.28: B_s^0 mass (left) and proper time (right) projections of the two-dimensional fit to $B_s^0 \to J/\psi\phi$ candidates with $t > 0.3$ ps. The total fit is represented by the blue solid line, the signal contribution by the green dashed line and the background contribution by the red dashed line. The mass range for the fit is $[5.20, 5.55]$ GeV/c^2 [86].

$|A_0(0)|, |A_\parallel(0)|, |A_\perp(0)|$ and ϕ_s are respectively the angular amplitudes and the CP-violating phase in $B_s^0 \to J/\psi\phi$.

The resulting function is then convoluted with three Gaussians with different widths, which describe the detector resolution function. For the background, two exponentials are used to describe the long-lived background candidates, and the prompt component is described by three Gaussians as the resolution function.

For the mass part Pdf_{mass}, one Gaussian is used to model the signal, and a linear function for the background. The mass of the B_s^0 candidates is calculated with the J/ψ mass constraint applied. It is observed that the description of the resolution model is not perfect and affected by the candidates with negative proper time. The fit was also performed with t$>$ 0.3 ps (projections are shown in Figure 3.28). In this case, no prompt background survives, this simplify the fit and make it faster without loosing any sensitivity on physical parameters.

The long-lived background parameters are left floating in the fit, while those of the resolution are fixed from the fit performed at wider time range, see Figure 3.27. The number of signal candidates found by the fit is $N_{sig} = 570 \pm 24$, and the mass resolution is ~ 7 MeV/c^2.

As it is explained in the introduction of this Chapter, the proper time

distribution is fitted with a single exponential, this B_s^0 effective lifetime is denoted $\tau_{B_s^0}^{single}$ and is found to be:

$$\tau_{B_s^0}^{single}(B_s^0 \to J/\psi\phi) = 1.447 \pm 0.064(stat) \pm 0.056(sys)\,\text{ps}\ ,$$

Using a single exponential to model the proper time distribution implies ignoring the non-zero width difference of the B_s^0 system. $\tau_{B_s^0}^{single}$ equations are given in Equation 3.11

Our measurement of $\tau_{B_s^0}^{single}$ at LHCb is compatible with the CDF and D0 average for the $\tau_{B_s^0}^{single}$ [96].

Systematic uncertainty sources are studied in detail in [97]. It is found that the systematic uncertainty is dominated by the proper time acceptance mismodeling ($= 0.04\,\text{ps}$). The proper time acceptance function is extracted from the Monte Carlo. The systematic error of this source is estimated as the difference between the results obtained with and without the acceptance correction.

Non-perfect modeling of signal and background is also considered in this analysis and estimated by running the fits with alternative parametrization. It is expected to drop when more statistics are available. In addition the errors related to the momentum scale and the decay length scale are expected to improve with better understanding of the alignment and tracking detectors.

3.5 Alternative selection proposal

In this section we propose a new selection for the advanced phase of data taking at LHCb. In this new approach, we free the selection optimization from constraints on proper time. The motivation behind this study is based on following points:

- the unbiased lines saturate the trigger bandwidth with prompt background candidates. Using proper time cuts will remove the prompt background component, enabling a better use of the bandwidth;
- Adding lifetime biasing cuts allows to relax the tight kinematic cuts, resulting in a gain in the signal yield.

The new selection is a part of strategy where:

- the lifetime biased selection is the main line and provides the fit with $B_s^0 \to J/\psi\phi$ events;
- a dedicated lifetime unbiased selection is designed to extract the proper time acceptance and the resolution model.

The unbiased line in the case of biased strategy should be prescaled. This reduces the number of the unbiased signal event by a prescaling factor. This makes those event contribute only marginally in the phis fit.

In the following we present the set of cuts chosen for this selection using MC2010 Monte Carlo samples. The cuts optimization is addressed against the prompt background.

Selection cuts proposal

Cuts on kinematics and PID informationof the $B_s^0 \to J/\psi\phi$ decay products are loosened and will be summarized in Table 3.8. We show the plots of cuts that are unique for the biased selection. The main principle to select muons and kaons remains unchanged; we apply PID cuts to distinguish those from pions. In addition, cuts on their tracks χ^2/nDoF are loosened. The cut on the p_T of the muons is removed (although no real gain can be assigned to this, because different trigger levels already cut on this quantity). All cuts are loosened when building the J/ψ vertex, mass range is larger (50 MeV/c^2) and the J/ψ vertex χ^2/nDoF is looser.

The first cut added to the biased selection is a cut on the distribution of minimum of the p_T of the two kaons. The Figure 3.29, shows the distribution for this quantity for the signal and different background sources. We

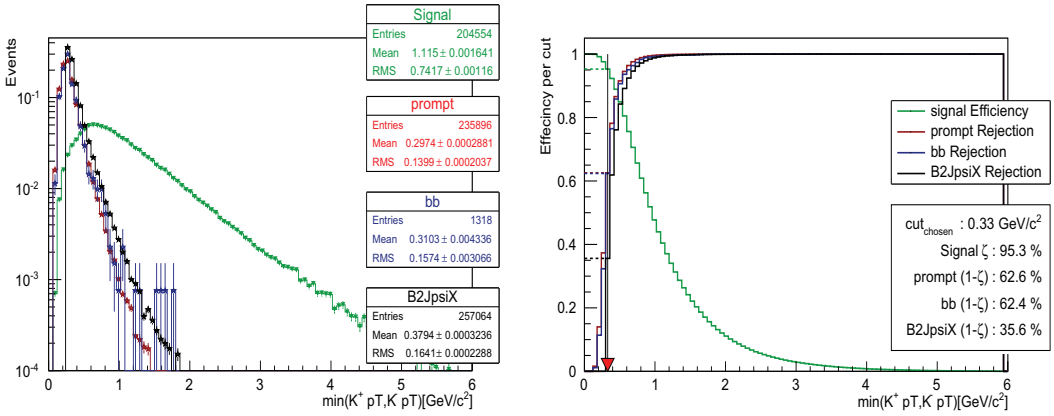

Figure 3.29: Left: distribution of the minimum kaons' p_T for $B_s^0 \to J/\psi\phi$ signal candidates (green), $b\bar{b}$ inclusive candidates (blue), $B_{u,d,s} \to J/\psi X$ candidates (black), and prompt inclusive J/ψ candidates. Right: signal efficiency and individual background rejection rates per cut.

then remove the cut on the p_T of the ϕ, and release the cut on its mass to 20 MeV/c^2 around the nominal mass of the ϕ.

Combining the two particles into one vertex yields the B_s^0 particle. We release the cut on the vertex quality to be $\chi^2_{\text{vertex}}/\text{nDoF} < 12$.

The biasing cuts, used to get rid of the prompt background, are: the direction angle cut, and the vetex separation χ^2. We show the definitions of those variables in Figure 3.30. Firstly, we cut on the direction angle cut, which is the cosine of the angle between the reconstructed momentum of the B_s^0 and the direction of the vetex separation originating from a primary vertex.

Secondly, we cut on the χ^2 of the vetex separation, where the vetex separation is the distance between the decay vertex of the B_s^0 particle and its reconstructed primary vertex. The distribution is correlated with the direction angle variable.

The background-to-signal ratios, for the prompt and long-lived background, can be calculated using the same conventions and equations as before (see Section 3.3.5 Equations 3.8 and 3.9). The results are gathered in the Table 3.9, those results are obtained without applying any trigger cuts.

The trigger strategy for this analysis is in development. Any trigger lines for this analysis should take in consideration the fact that one need a control sample where the biasing cut are *not* applied, in order to calculate the proper time distortions caused by these cuts, and the proper time resolution function.

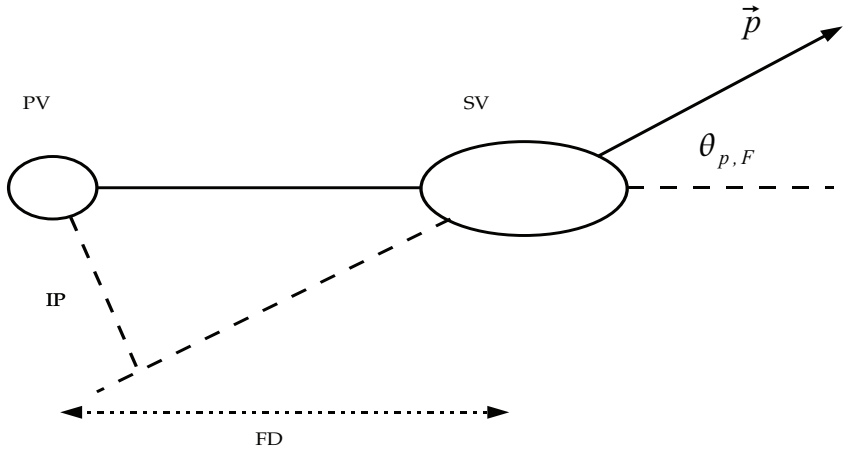

Figure 3.30: Geometrical variable definitions, vetex separation (FD), impact parameter (IP), direction angle ($\theta_{p,F}$).

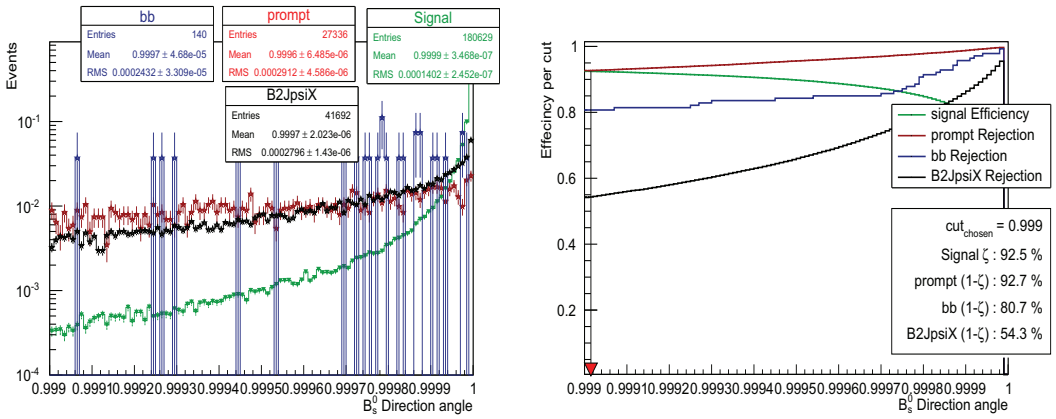

Figure 3.31: Left: distribution of the B_s^0 direction angle for $B_s^0 \to J/\psi\phi$ signal candidates (green), $b\bar{b}$ inclusive candidates (blue), $B_{u,d,s} \to J/\psi X$ candidates (black), and prompt inclusive J/ψ candidates. Right: signal efficiency and individual background rejection rates per cut.

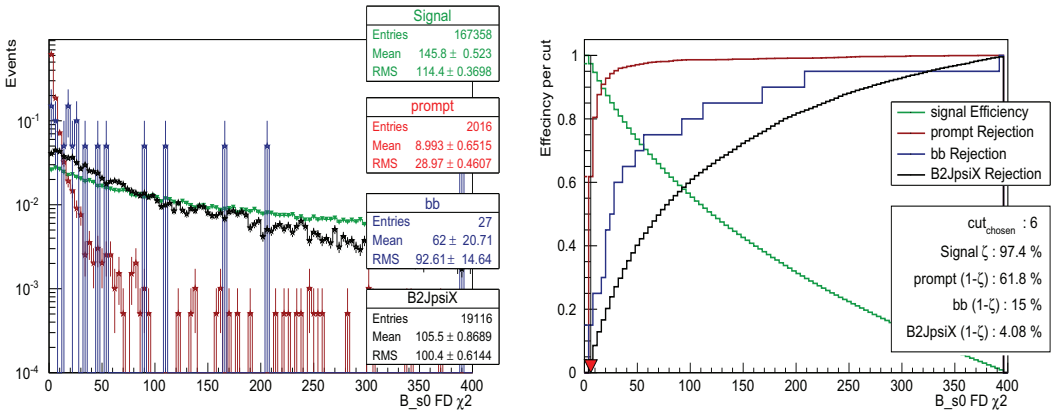

Figure 3.32: Left: distribution of the B_s^0 vetex separation χ^2 for $B_s^0 \to J/\psi\phi$ signal candidates (green), $b\bar{b}$ inclusive candidates (blue), $B_{u,d,s} \to J/\psi X$ candidates (black), and prompt inclusive J/ψ candidates. Right: signal efficiency and individual background rejection rates per cut.

Decay mode	Cuts
$J/\psi \to \mu^+\mu^-$	$\Delta \ln \mathcal{L}_{\mu\pi} > -5$ muons $\chi^2_{\text{track}}/\text{nDoF} < 5$ $\chi^2_{\text{vtx}}/\text{nDoF}(J/\psi) < 15$ $\lvert M(\mu\mu) - M(J/\psi)\rvert < \pm 50\,\text{MeV}/c^2$
$\phi \to K^+K^-$	$\Delta \ln \mathcal{L}_{K\pi} > 0$ $min(K^+ p_T, K^- p_T) > 350\,\text{MeV}/c^2$ kaons $\chi^2_{\text{track}}/\text{nDoF} < 5$ $\chi^2_{\text{vtx}}/\text{nDoF}(\phi) < 15$ $\lvert M(K^+K^-) - M(\phi)\rvert < \pm 20\,\text{MeV}/c^2$
$B_s^0 \to J/\psi\phi$	$\chi^2_{\text{vtx}}/\text{nDoF} < 12$ $cos(\theta_{p,F}) > 0.999$ FD $\chi^2 > 6$ $\lvert M(B_s^0) - M(J/\psi\phi)\rvert < \pm 50\,\text{MeV}/c^2$

Table 3.8: Table summarizes the cuts developed for the biased analysis, applied to the $B_s^0 \to J/\psi\phi$ channel.

	Biased selection	factor w.r.t unbiased analysis
$\mathcal{Y}$	$160.\,k$	1.52
B_{prompt}/S	0.19 ± 0.10	13
$B_{\text{b}\bar{\text{b}}}/S$	0.15 ± 0.08	1.33

Table 3.9: Table summarizes the yield and B/S rates for biased analysis, along with the gain obtained comparing to the same quantities in the unbiased selection (MC2010).

A clear gain in terms of yield is obtained, indeed releasing the kinematic cuts on the ϕ particle in addition to loosening the quality cuts specially on the B_s^0 vertex pays off in terms of signal efficiency. The signal yield in Table 3.9 is obtained *before any trigger* and it is compared to the yield expected from the unbiased selection *before any trigger* as well[10].

For biased analysis, we expect a better trigger efficiency since the biased selection can benefit from both biased and unbiased trigger lines [11]. Detailed studies about the biased trigger lines and strategy were carried out here [99]. We performed full study of the biased selection on the background using Monte Carlo sample in [98]. Here, we update the signal yield and the B/S ratios, we use the same tagging performance measured in the unbiased selection. We summarize the results of this study in the Table 3.10.

[10] unbiased yield before any trigger is $60\,000/57\% = 105$k events.

[11] the biased trigger efficiency can be as high as 80% for some scenarios [98].

Parameter	Signal	Prompt background (Pr)	Long-lived background (LL)
Events in B_s^0 mass window $\pm 50\,\mathrm{MeV}/c^2$ (fractions, B/S)	100 k (74.6%)	19 k (14.2%, $B_{\mathrm{Pr}}/S = 0.19$)	15 k (11.2%, $B_{\mathrm{LL}}/S = 0.15$)
Mass m (MeV/c^2)	2 Gauss; $f^{\mathrm{s}}_{m,1} = 0.67$; $\sigma^{\mathrm{s}}_{m,1} = 4.9$; $\sigma^{\mathrm{s}}_{m,2} = 9.14$	$\mathrm{Exp}(-\alpha^{\mathrm{Pr}}_m m)$; $\alpha^{\mathrm{Pr}}_m = -0.0015$	$\mathrm{Exp}(-\alpha^{\mathrm{LL}}_m m)$; $\alpha^{\mathrm{LL}}_m = 0.0016$
Proper time t (fs)	Signal PDF $\otimes$ 2 Gauss; $f^{\mathrm{s}}_{t,1} = 0.63$; $\mu^{\mathrm{s}}_{t,1} = 0$; $\sigma^{\mathrm{s}}_{t,1} = 27.9$; $\mu^{\mathrm{s}}_{t,2} = 0$; $\sigma^{\mathrm{s}}_{t,2} = 53.2$	$\delta(t) \otimes$ 1 Gauss; $\mu^{\mathrm{Pr}}_t = 0$; $\sigma^{\mathrm{Pr}}_t = 40$ (one-side)	2 Exponentials $\otimes$ 1 Gauss; $f^{\mathrm{LL}}_{\tau_1} = 0.50$; $\tau^{\mathrm{LL}}_1 = 758$, $\tau^{\mathrm{LL}}_{t,2} = 252$; $\mu^{\mathrm{LL}}_t = 0$; $\sigma^{\mathrm{LL}}_t = 60$
Angles	no acceptance flat background	no acceptance flat background	no acceptance flat background
Flavour tagging	$\varepsilon_{\mathrm{tag}} = 0.564$; $\omega = 0.334$	$\varepsilon^{\mathrm{Pr}}_{\mathrm{tag}} = 0.30$	$\varepsilon^{\mathrm{LL}}_{\mathrm{tag}} = 0.62$

Table 3.10: Summary of baseline detector input parameters for sensitivity studies with the biased cuts, extracted from full Monte Carlo.

Proper time acceptance extraction:

The benefits of the biased selection comes with a cost, that is the bias created on the proper time distribution. Such bias results in a non-trivial proper time acceptance function.

We discuss here a method to extract this acceptance directly from real data, without relying on Monte Carlo. The method is based on a "smart" background subtraction called the "sPlot" technique [100]. If a data sample consists of multiple types of events (e.g. signal and backgrounds), sPlot reconstructs variables which are unknown for each type, by using information from a known "discriminate" variables available in the sample (e.g. mass).

With this tool, we can extract the biased proper time distribution, for the signal, from the data sample. The next step is to repeat the same process using an unbiased data sample, where the biasing cuts are not applied. This provides the unbiased proper time distribution for the signal events. Dividing the two distributions gives the desired proper time acceptance function.

We make use of a Monte Carlo data sample that is similar to real data in order to test this method. Our choice is the $B_{u,d,s} \rightarrow J/\psi X$, as it is rich in both signal and background.

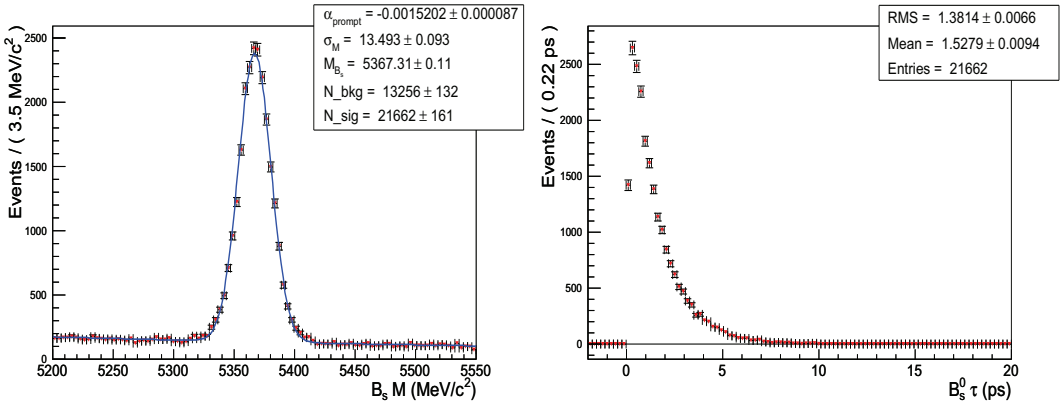

Figure 3.33: Left: mass distribution for events passing the biased selection cuts, in the $B_{u,d,s} \rightarrow J/\psi X$ Monte Carlo sample, it is fitted with a single Gaussian for the signal model and an exponential to model the background. Right: biased proper time distribution for the *signal* obtained using sPlos technique

We apply the biased selection on the sample Table 3.8. Figure 3.33 shows the proper time distribution obtained with sPlot technique. By removing the biasing cuts (i.e. $cos(\theta_{p,F}) > 0.999$ and FD$\chi^2 > 6$), we repeat

the same procedure using sPlot, extracting the unbiased proper time distribution for the signal, as shown in Figure 3.34.

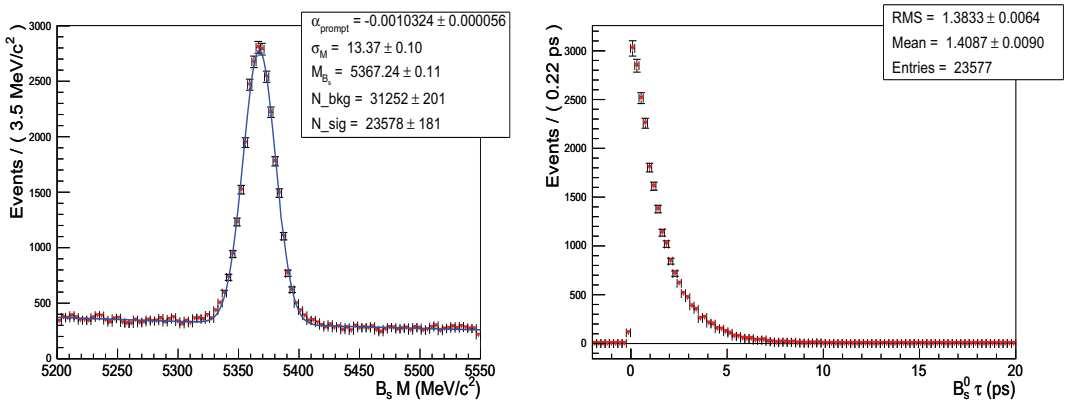

Figure 3.34: Left: mass distribution for all event passing the unbiased selection cuts, in the $B_{u,d,s} \rightarrow J/\psi X$ Monte Carlo sample, this is fitted with a Gaussian for the signal and an exponential to model the background. Right: unbiased proper time distribution for the *signal* obtained using sPlot technique (MC2010).

At last, the ratio of the biased proper time distribution to the unbiased one is the acceptance function, shown in Figure 3.35 (right). To check the validity of this method, we compute the "true" proper time acceptance, as it is explained in Section 3.3.4, where we rely on Monte Carlo information to pick the true signal in the $B_{u,d,s} \rightarrow J/\psi X$ sample. Figure 3.35 (left), shows the "true" proper time acceptance for the signal events. We fit both acceptance function with this empirical function:

$$\mathrm{Acc}_{\mathrm{fit}} = \frac{(s \times t_{\mathrm{reco}})^3}{1 + (s \times t_{\mathrm{reco}})^3}. \tag{3.13}$$

where s represents the slope of at low proper times, t_{reco} is the reconstructed proper time.

The s values are given in Table 3.5. We find the two slopes coming from the true and the sPlot acceptance function to be compatible within $\sim 0.8\sigma$.

This method gave an accurate estimation to the proper time acceptance function, without relying on Monte Carlo. It requires, nonetheless, a dedicated unbiased line in order to extract the unbiased proper time distribution for the signal. This study is an important result of this analysis. Systematics induced by this method are studied in chapter 5

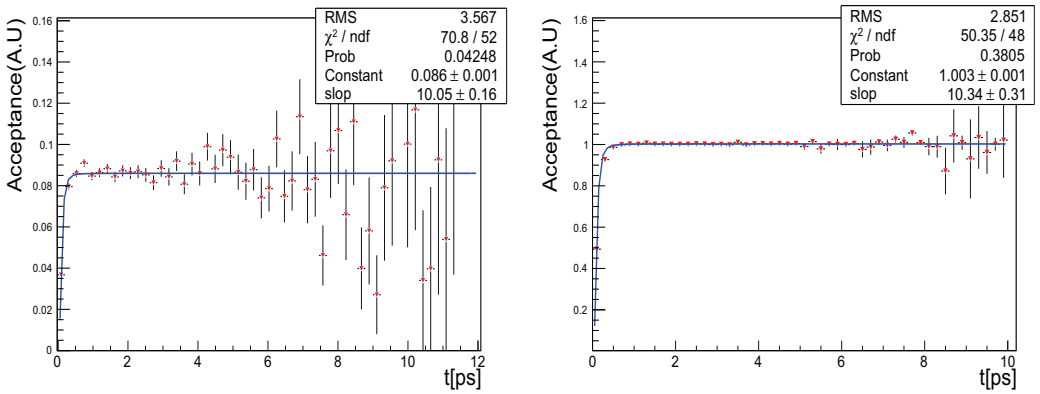

Figure 3.35: Left: proper time acceptance using Monte Carlo information calculated in the $B_{u,d,s} \to J/\psi X$ sample. Right: proper time acceptance calculated using sPlot distributions in the same sample.

	"True" acceptance	sPlot acceptance
Slope	10.05 ± 0.16	10.34 ± 0.31

Table 3.11: The slope values extracted from "true" acceptance (column 2) and from acceptance function fitted to sPlot acceptance function (column 3).

3.6 Summary

In this chapter, we described the proper time unbiased selection optimization and performance using extensive studies on Monte Carlo samples. This is the core of first data analysis strategy at LHCb. A unified selection for the $B_s^0 \to J/\psi\phi$, $B_d^0 \to J/\psi K^{*0}$ and $B^+ \to J/\psi K^+$ channels is adopted to reduce systematic uncertainties when measuring the ϕ_s parameter.

The selection tightens the kinematic cuts (p_T, mass) and avoids any cut that biases the proper time and angular variables. Background is composed of two components: the highest background is the *prompt*, the second is the *long-lived*. A detailed study for both signal and background properties is shown with the help of Monte Carlo.

The 2010 configuration of the LHC machine creates a high pile-up environment. Its effects on the signal selection efficiency and proper time resolution is studied.

An unbiased selection is applied to the first data taken in 2010. We presented briefly the effective lifetime measurement for the $B_s^0 \to J/\psi\phi$

performed on $\sim 36\,\mathrm{pb}^{-1}$ of integrated luminosity. The effective B_s^0 lifetime is determined with this data sample: $\tau_{B_s^0}^{single} = 1.447 \pm 0.064(\mathrm{stat}) \pm 0.056(\mathrm{sys})$.

We presented an alternative strategy, developed for the next phase of data taking, where prompt occupancy of band width will not be tolerated. This new selection removes all constraints from the unbiased one, and uses proper time biasing cuts. Using this selection, clear gains in terms of yield and prompt background reduction are observed with respect to the unbiased selection.

One of the disadvantages of the biased selection is the proper time distortion. We proposed a method relying on sPlot technique in order to extract this distortion from real data without relying on Monte Carlo information. This method requires an unbiased sample provided by an unbiased trigger line.

Chapter 4

Tagging studies

The determination of the flavour of the B_s^0 meson is a crucial step when performaing many of the CP measurments. This process is called flavour tagging. In this Chapter, the performance of the flavour tagging with both Monte Carlo and 2010 data samples are presented. These results are obtained using the unbiased selection applied on $B_s^0 \to J/\psi\phi$ channel and its control channels $B_d^0 \to J/\psi K^{*0}$ and $B^+ \to J/\psi K^+$ [101]. This chapter deals with the "opposite-side" tagging properties. Effects of high pile-up on reconstruction and selection were studied in the previous chapter. Here we show that those changes affect the tagging performance of the $B_s^0 \to J/\psi\phi$ channel.

In Section 4.1, we summarize the flavor tagging procedure in LHCb. High pile-up effects on tagging performance are studied in Section 4.3. Finally in Section 4.4 we describe the tagging performance for Monte Carlo samples and 2010 data respectively in the three channels $B^+ \to J/\psi K^+$, $B_d^0 \to J/\psi K^{*0}$ and $B_s^0 \to J/\psi\phi$.

4.1 Flavor tagging algorithm

Tagging the initial flavor of the B_s^0 at production is an indispensable elemnet of ϕ_s analysis. Although the untagged decay rates do carry information on ϕ_s, the sensitivity of the tagged rates is much higher, particularly in the case that ϕ_s is small [5].

Many CP asymmetry measurements depend on the knowledge of the b-meson initial flavor. The process of the determining whether a b-meson contains a b or $\overline{b}$ quark at production is called "flavor tagging". This process is performed at LHCb using different tagging algorithms described

in [101, 102, 103] and illustrated in Figure 4.1.

At LHC, b-hadrons are generally produced in pairs. We designate the studied b-meson and its final state particles as "signal side" (also called "same side") and the other b-meson as the "opposite side". Two types of taggers are used to identify the initial b-meson flavor:

- Opposite-side (OS) taggers use the charge of leptons from semileptonic b-hadron decays and kaons from the b to c to s decay chain. They can also use the charge of the inclusive secondary vertex reconstructed from the b decay products. Opposite-side taggers can be used to tag all b-hadrons;

- Same-side (SS) taggers are based on the correlation between the charge of the B and the charge of nearby mesons from fragmentation chain or from the decay of existed $\mathrm{B_s^0}$. Kaons are used to tag $\mathrm{B_s^0}$, while pions are used to tag $\mathrm{B_d^0}$ and $\mathrm{B^+}$.

The tagging algorithm is characterized by:

- mistag rate: $\omega = W/(W+R)$;

- tagging efficiency: $\epsilon_{\mathrm{tag}} = (W+R)/(W+R+U)$;

- effective tagging efficiency (or tagging power): $\epsilon_{\mathrm{eff}} = \epsilon_{\mathrm{tag}}(1-2\omega)^2$.

where W, R and U are, respectively, the number of candidates wrongly tagged, correctly tagged and untagged.

To select a tagging particle, cuts on track quality, PID information and momentum are applied. The charge of the tagging particle is used to define the tagging decision d, denoted -1 if the b-hadron contains b quark, $+1$ if it contains $\overline{\mathrm{b}}$ quark and 0 if no tag decision is given.

The cuts have been optimized to maximize the effective tagging efficiency using 2010 data. This optimization was first performed on the $\mathrm{B_d^0} \to \mathrm{D^{*-}}\mu^+\nu_\mu$ and the $\mathrm{B^+} \to \mathrm{J/\psi K^+}$ self-tagging channels, since these channels have the largest number of event. The performance obtained from the optimized cuts are then measured with the $\mathrm{B_d^0} \to \mathrm{J/\psi K^{*0}}$ channel.

For each tagger i a probability $(1-\omega_i)$ of the tagging decision to be correct is assigned. It is estimated using several kinematic and geometrical properties of the tagger. This is done by the means of a neural net. The mistag rate can be measured on data using flavor-specific decay channels. For charged mesons the mistag is obtained by comparing the flavor of the

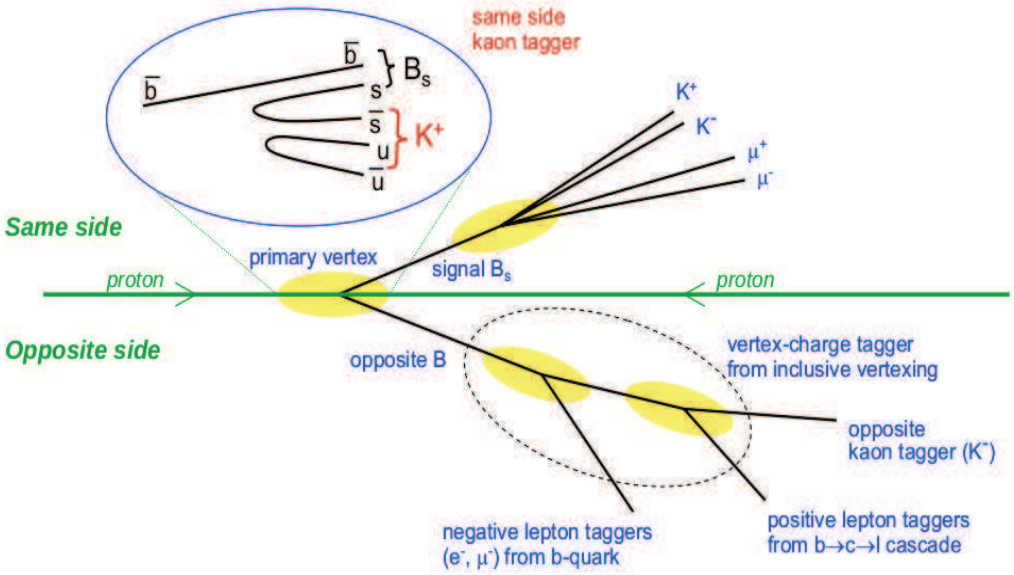

Figure 4.1: Schematic representation of the different sources of information available to tag the b-meson flavor, here $B_s^0 \to J/\psi\phi$.

reconstructed flavor with the tagging decision. For neutrals it is done by fitting the flavor oscillation as a function of proper time.

These probabilities are calibrated on data using $B^+ \to J/\psi K^+$ channel.The mistag probabilities of different taggers can be combined in different ways:

- combining the tagging decisions and probabilities for the opposite-side taggers only, this is a universal combination for all b-mesons;
- combining all taggers (including the same-side tagger (SS kaon or SS pion), this combination is different for B_s^0 and B_d^0, B^+ ones.

Those combined mistag probabilities can be then used in three ways:

- to form one average mistag for the full sample. This is the simplest solution but the one giving the least sensitivity to the physical parameters;
- to split events into categories of similar effective tagging efficiencies, and then to calculate an average mistag for the whole sample using those categories;
- to estimate the mistag probability on event-per-event basis.

The event by event mistag probability is calibrated in the $B^+ \to J/\psi K^+$ channel, where a linear dependence between the measured and the calculated mistag is observed:

$$\omega = p_0 + p_1(\eta - \langle\eta\rangle), \tag{4.1}$$

where p_0 and p_1 are free parameters and $\langle\eta\rangle$ is the mean calculated mistag probability. To extract the calibration parameters, an unbinned likelihood fit to the mass, tagging decision and η observables is performed[1]. In the following, we will present the tagging performance with the unbiased selection using Monte Carlo samples.

4.2 Tagging properties with Monte Carlo samples

The cuts developed in Chapter 3 for $B_s^0 \to J/\psi\phi$ are applied when possible in the control channels. This is done to ensure that B_s^0 candidates in the signal channel will have similar kinematics to the B candidates in the two control channels. This allows, the opposite-side tagging properties to be exported from control to signal channels without corrections.

The flavor tagging performance are measured by comparing the true initial B flavor as determined by the Monte Carlo truth information to the decision given by the tagging algorithm.

The total effective tagging efficiency is given after sorting all the events into five exclusive samples of increasing tagging purity, this allows the increase of the total effective efficiency. A detailed description of the combination is found in [102].

Trigger lines and selection cuts, used for the 2010 data, are applied on the Monte Carlo samples used in this study. Tables 4.1, 4.2 and 4.3 show the individual mistag, tagging efficiency and effective efficiency for the individual taggers and for tagging categories, and present the combination of tagging parameters for opposite-side taggers. The combined opposite-side effective efficiency $\epsilon_{\text{eff}}(B_s^0 \to J/\psi\phi) = (2.64 \pm 0.08)\%$, $\epsilon_{\text{eff}}(B^+ \to J/\psi K^+) = (2.77 \pm 0.07)\%$, $\epsilon_{\text{eff}}(B_d^0 \to J/\psi K^{*0}) = (2.64 \pm 0.10)\%$ are compatible for the three channels, as a result of applying a unified event selection for the three channels.

[1] The pdf fo η, involved in the fit, is extracted from data for signal and background separately.

$B^+ \to J/\psi K^+$			
	$\varepsilon_{tag}(\%)$	$\omega(\%)$	$\varepsilon_{eff}(\%)$
Individual taggers			
μ	4.93±0.03	30.37±0.33	0.76±0.03
e	2.46±0.02	33.16±0.48	0.28±0.02
K	11.43±0.05	33.20±0.22	1.29±0.03
SSπ	16.71±0.06	39.83±0.19	0.69±0.03
Q_{vtx}	22.09±0.07	40.31±0.17	0.83±0.03
Combination of taggers: OS			
Average	23.92±0.07	34.43±0.16	2.32±0.05
combined	23.92±0.07	33.00±0.16	2.77±0.07
Combination of taggers: SSπ+OS			
Average	31.24±0.07	34.56±0.14	2.98±0.05
combined	31.24±0.07	33.14±0.14	3.55±0.08

Table 4.1: Flavour tagging performance for the individual taggers and the combinations of taggers with $B^+ \to J/\psi K^+$ signal Monte Carlo events passing the selection and the trigger cuts. Uncertainties are statistical.

$B_d^0 \to J/\psi K^{*0}$			
	$\varepsilon_{tag}(\%)$	$\omega(\%)$	$\varepsilon_{eff}(\%)$
Individual taggers			
μ	4.94±0.05	31.45±0.48	0.68±0.04
e	2.49±0.04	32.67±0.69	0.30±0.02
K	11.40±0.07	33.96±0.32	1.17±0.05
SSπ	17.76±0.09	40.15±0.27	0.69±0.04
Q_{vtx}	22.17±0.10	40.30±0.24	0.83±0.04
Combination of taggers: OS			
Average	23.95±0.10	34.96±0.23	2.17±0.07
combined	23.95±0.10	33.41±0.23	2.64±0.10
Combination of taggers: SSπ+OS			
Average	32.35±0.11	35.23±0.19	2.82±0.07
combined	32.35±0.11	33.69±0.19	3.44±0.11

Table 4.2: Flavour tagging performance for the individual taggers and the combinations of taggers with $B_d^0 \to J/\psi K^{*0}$ signal Monte Carlo events. Uncertainties are statistical.

$B_s^0 \to J/\psi\phi$			
	$\varepsilon_{tag}(\%)$	$\omega(\%)$	$\varepsilon_{eff}(\%)$
Individual taggers			
μ	4.62 ± 0.06	30.28 ± 0.60	0.72 ± 0.04
e	2.41 ± 0.04	32.02 ± 0.85	0.28 ± 0.03
K	11.55 ± 0.09	33.74 ± 0.39	1.22 ± 0.06
SS K	14.48 ± 0.10	31.88 ± 0.34	1.90 ± 0.07
Q_{vtx}	21.41 ± 0.12	40.2 ± 0.30	0.82 ± 0.05
Combination of taggers: OS			
Average	23.94 ± 0.13	34.82 ± 0.25	2.21 ± 0.06
combined	23.94 ± 0.12	33.38 ± 0.27	2.64 ± 0.08
Combination of taggers: SSK+OS			
Average	33.21 ± 0.13	32.64 ± 0.20	4.00 ± 0.07
combined	33.21 ± 0.13	30.60 ± 0.23	5.00 ± 0.11

Table 4.3: Flavor tagging performance the individual taggers and the combinations of taggers with $B_s^0 \to J/\psi\phi$ signal Monte Carlo events. Uncertainties are statistical.

4.3 High pile-up impact on tagging

In this section we continue the study started in Chapter 3, where we present the effect of the high pile-up scheme adopted by the LHC machine for the 2010 run. This scheme has a high number of proton-proton collisions (ν) per bunch which creates an environment where the number of tracks and vertices per event increases[2].

A Monte Carlo sample are generated to simulate this environment. We study the effect of such phenomena in terms of the number of tracks per event, dividing the Monte Carlo sample into bins of track multiplicity[3] ($< 150, 150 - 250, > 250$) and measuring the tagging performance in each bin.

Figure 4.2 shows the mistag rate for individual taggers (left) and the combined mistag rate (right). A clear increase in mistag rate is observed as the number of tracks per event increases. In Figure 4.3, the tagging efficiency increase with the track multiplicity for most of the taggers. As the background increases in such an environment (e.g. more pion tracks), selecting the right taggers in the event will become harder, resulting in a higher mistag rate.

The resulting effective tagging efficiency, which is the parameter of interest for the ϕ_s sensitivity, suffers a drop for all taggers, where the excess in tagging efficiency can not compensate the mistag loss. This drop will have negative impact on the ϕ_s sensitivity. Figure 4.4 shows the degradation of effective tagging efficiency per tagger (left) and the combined one (right)

The impact of tagging performance degradation and other effects studied in Chapter 3 on the ϕ_s sensitivity is summarized in Figure 4.5, where the following formula is used:

$$\sigma(\phi_s) \propto \frac{1}{\sqrt{N_{sig}\epsilon_{\text{tag}}}} \times \exp(0.5 \times (\sigma_t \times \Delta m_s)^2). \tag{4.2}$$

Figure 4.5 indicates that the ϕ_s sensitivity decreases when more tracks are present in the event. A new strategy for the tagger selection can help reduce the loss in effective tagging efficiency and consequently gain back some of the ϕ_s sensitivity. A new approach that includes developments in trigger, reconstruction and tagging algorithms has been performed to face the high pile-up challenge. The new optimization performed on the 2010 data was able to recover most of the loss.

[2]LHCb was designed for $\nu = 0.4$, in 2010 LHCb this value surpassed $\nu = 2.5$ in some runs.

[3]number of best tracks per event is defined in Chapter 3 .

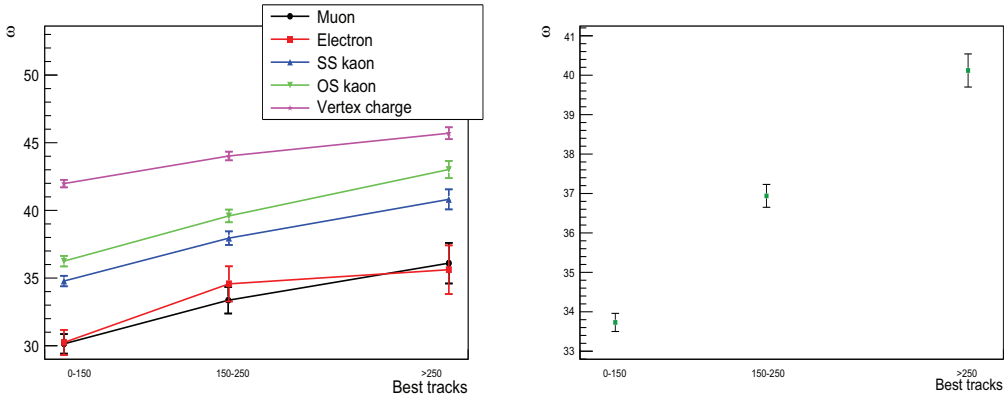

Figure 4.2: Left: individual mistag rate for each tagger in range of track multiplicity. Right: *combined* mistag rate in range of track multiplicity.

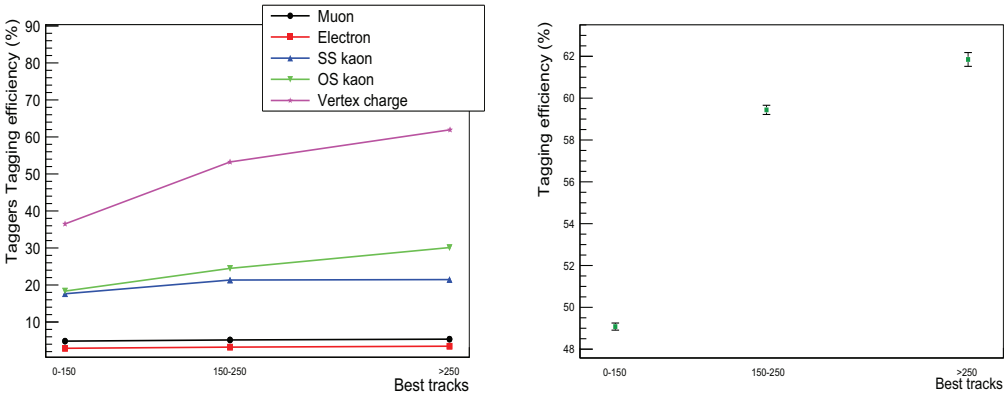

Figure 4.3: Left: individual tagging efficiency for each tagger in range of track multiplicity. Right: *combined* tagging efficiency in range of track multiplicity per event.

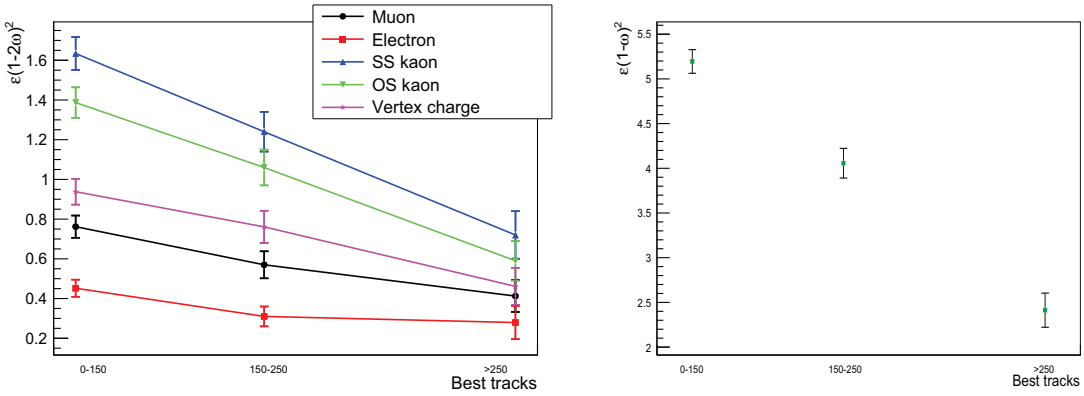

Figure 4.4: Left: individual effective tagging efficiency in range of track multiplicity. Right: *combined* effective tagging efficiency in range of track multiplicity.

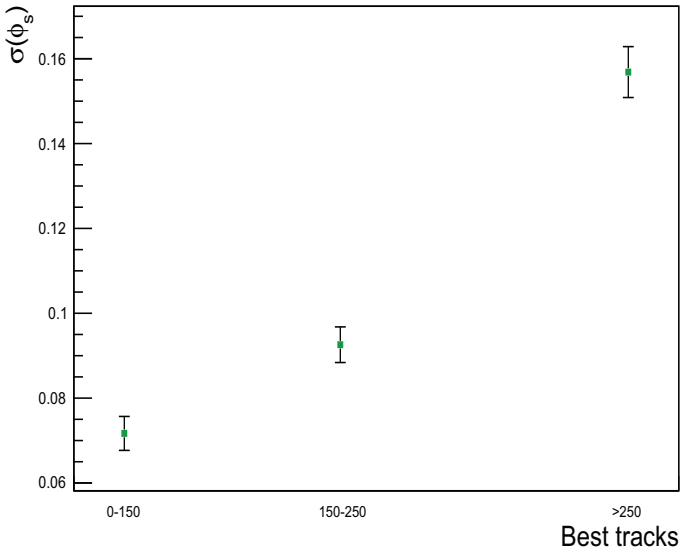

Figure 4.5: Sensitivity of ϕ_s parameter versus the number of tracks per event.

p_0	p_1	$\langle\eta\rangle$	$\rho(p_0, p_1)$
$0.338 \pm 0.012 \pm 0.004$	$1.01 \pm 0.12 \pm 0.01$	0.339	-0.05

Table 4.4: Calibration parameters, average mistag and correlation between the calibrations parameters, extracted from the $B_s^0 \to J/\psi\phi$ control channel [101]. The first error is statistical and the second systematic.

4.4 Opposite side tagger in 2010 real data

The measured mistag in the calibration channels can be used in the ϕ_s final fit performed in the $B_s^0 \to J/\psi\phi$ channel. This is done with the restriction that selection, trigger, p_T spectrum and running conditions are similar if not identical. In the final determination of the ϕ_s with 2010 data, the event-by-event misatg is used.

As explained earlier the calibration of the event-by-event mistag is done in the self-tagged $B^+ \to J/\psi K^+$ channel. The calibration parameters of the Equation 4.1 are fitted and given in Table 4.4, the p_0 and p_1 values are compatible with $\langle\eta\rangle$ and 1 respectively, indicating that the calculated mistag is correct.

To check the calibrated mistag, a time dependent asymmetry fit is performed in the $B_d^0 \to J/\psi K^{*0}$ control channel with floating calibration parameters, the results: $p_0 = 0.333 \pm 0.025 \pm 0.003$, $p_1 = 0.71 \pm 0.26 \pm 0.24$ and $\langle\eta\rangle = 0.35$ are compatible with what is found in $B^+ \to J/\psi K^+$ channel.

We summarize in the Table 4.5, the opposite-side mistag, tagging efficiency and effective tagging efficiency for the two control channels after the optimization of the tagger selection and the calibration of the mistag using the 2010 data. The measured mistag rate in the two channels agree within the available statistics. The complete study can be found in [101].

To validate the use of the above mistag rates in $B_s^0 \to J/\psi\phi$ channel, we compare the *signal* distribution of the p_T and the opposite-side combination of the mistag for those channels in 2010 data. This is done by using the sPlots technique [100] previously introduced in Chapter 3.

Figures 4.6, 4.7 and 4.8 shows the p_T and opposite-side mistag distributions for the control and signal channels. These plots are made with the unbiased selection cuts, applying proper time cut $t > 0.3$ ps and for events that are opposite-side tagged only. We observe a high degree of similarity among those distributions. For the $B_d^0 \to J/\psi K^{*0}$ p_T distribution, the p_T average is higher than the other modes. This is simply due to the $p_T > 2$ GeV cut applied in the stripping phase to reduce the high K^{*0}

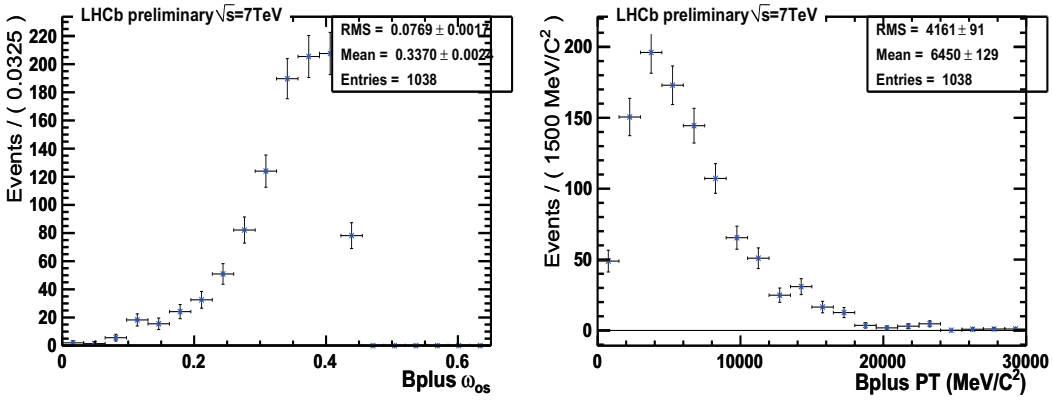

Figure 4.6: Left: Calibrated opposite-side mistag probability distribution for $B^+ \to J/\psi K^+$. Right: p_T distribution for $B^+ \to J/\psi K^+$.

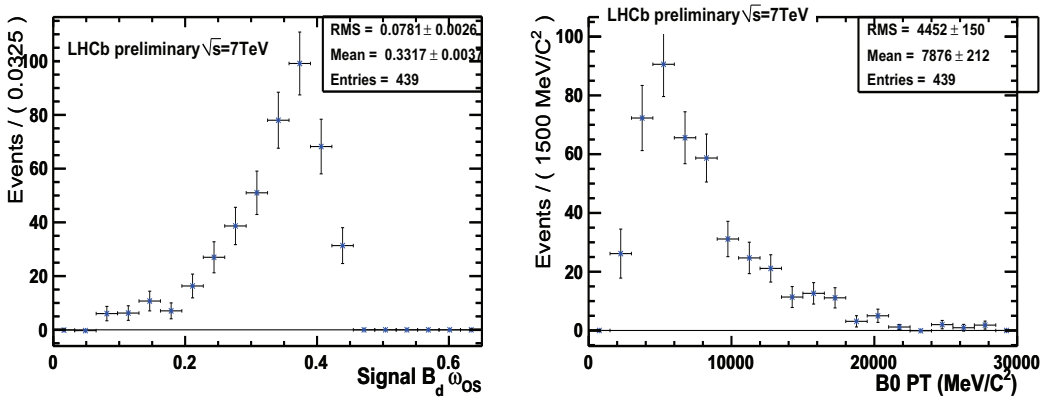

Figure 4.7: Left: Calibrated opposite-side mistag probability distribution for $B^0_d \to J/\psi K^{*0}$. Right: p_T distribution for $B^0_d \to J/\psi K^{*0}$.

	$\varepsilon_{tag}(\%)$	$\omega(\%)$	$\varepsilon_{eff}(\%)$
$B^+ \to J/\psi K^+$			
average OS	15.4±0.4	33.3±1.2	1.71±0.29
combined OS	15.4±0.3	32.2±1.2	1.97±0.31
$B_d^0 \to J/\psi K^{*0}$			
average OS	15.7 ± 0.6	33.1 ± 3.0	1.79 ± 0.71
combined OS	15.8 ± 0.7	30.0 ± 6.6	2.52 ± 0.82

Table 4.5: The flavor tagging performance is given for the OS and SSπ+OS separately, both averaged over the sample and combined after splitting in categories, for $B^+ \to J/\psi K^+$ (top) and $B_d^0 \to J/\psi K^{*0}$ (bottom), after the calibration. The quoted uncertainties are statistical only.

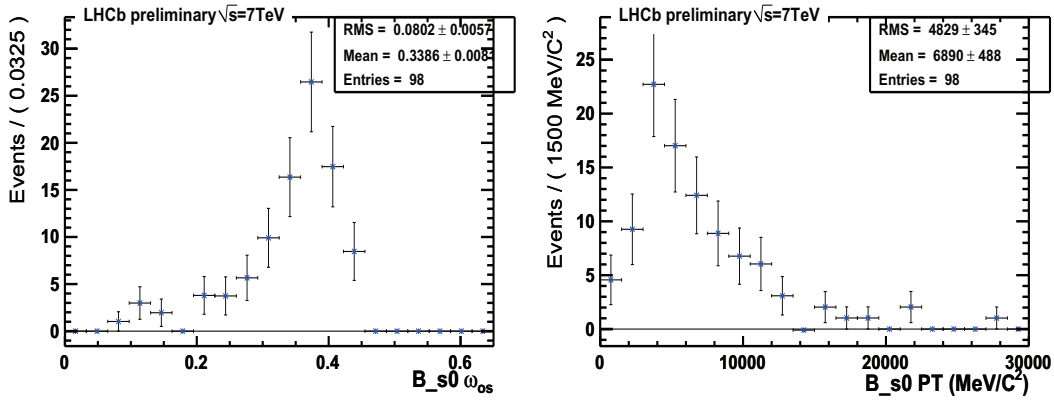

Figure 4.8: Left: Calibrated opposite-side mistag probability distribution for $B_s^0 \to J/\psi\phi$. Right: p_T distribution for $B_s^0 \to J/\psi\phi$.

background, keeping an acceptable retention.

From the $B_s^0 \to J/\psi\phi$ ω plot 4.9 (right), we calculate the tagging efficiency to be $98/575 = (17.04 \pm 1.56)\%$ which is compatible with what is found Table 4.5. We estimate the tagging dilution:

$$\langle \mathcal{D}^{tag} \rangle_{\text{eff}} = \sqrt{\frac{1}{N}\sum_{i=1}^{n}(1-2\omega_i)} = 0.35 \pm 0.03, \tag{4.3}$$

where the error on the dilution is dominated by the number of event in the calibration channel. The effective tagging efficiency for the $B_s^0 \to J/\psi\phi$ channel is: $\epsilon_{tag}\langle \mathcal{D}^{tag} \rangle_{\text{eff}} = (2.2 \pm 0.4)\%$

Another interesting check is the correlation between mistag rate and

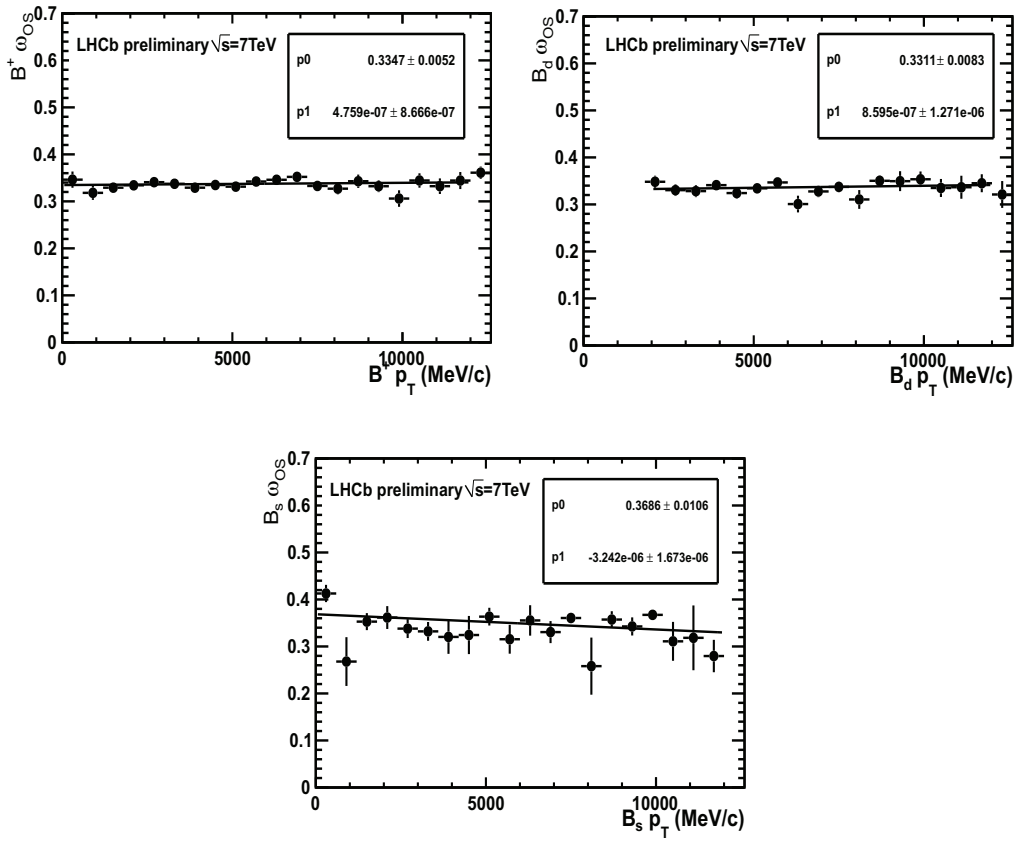

Figure 4.9: distributions of the mean calibrated opposite-side mistag probability as a function of the p_{T} of signal B for $\mathrm{B}^{+} \to \mathrm{J}/\psi\mathrm{K}^{+}$ (left), $\mathrm{B}^{0}_{\mathrm{d}} \to \mathrm{J}/\psi\mathrm{K}^{*0}$ (centre), $\mathrm{B}^{0}_{\mathrm{s}} \to \mathrm{J}/\psi\phi$ (right).

p_{T}. In Figure 4.9, we show the plots of mistag versus p_{T} for the control and signal channels. The plots shows a flat tendency, which agrees with the expectation from Monte Carlo.

4.5 Summary

In this chapter, we reviewed the flavor tagging procedure in LHCb and give the tagging performance on the $B_s^0 \to J/\psi\phi$ on Monte Carlo samples. A dedicated description of the tagging performance with the 2010 data was presented.

We explored the effects of high pile-up environment on the tagging properties and ϕ_s sensitivity. This is of particular importance as the running condition at LHCb in 2010 followed a scheme with high pile-up. The study concludes that high pile-up could lead to losses in tagging performance and consequently on ϕ_s sensitivity. A new strategy for the taggers selection has been adopted in order to cope with the 2010 running conditions.

In Monte Carlo and 2010 data, we found similar tagging performance among the signal and the two control channels $B_d^0 \to J/\psi K^{*0}$ and $B^+ \to J/\psi K^+$. This is an important validation of the purposes of the unbiased selection strategy which requires the same tagging properties for the signal and for the control channels..

The calibration performed in the $B^+ \to J/\psi K^+$ channel allows a correct estimation of the calculated event-by-event mistag, the calibration of the mistag rate is one of the crucial parameters in the final step of this analysis–the fit of the ϕ_s phase, which we will discuss in the Chapter 5.

Chapter 5

Fit

We describe in this chapter the fit of the ϕ_s phase in the $B_s^0 \to J/\psi\phi$ channel, which we developed before the data taking. We derive the probability density function (pdf). It is composed of two main parts: signal and background, where the signal decay rates are described in Chapter 1 and the backgrounds are described in Chapter 3. The pdf depends on the following observables: B_s^0 mass, proper time, angular variables and tagging decision. We make use of a fast Monte Carlo simulation tool (toy MC), and full Monte Carlo simulation in order to test and validate our fitter program.

In Section 5.1 we introduce the pdf describing the signal and background sources of the $B_s^0 \to J/\psi\phi$ channel. A fit to the full Monte Carlo signal sample is presented in Section 5.2. In Section 5.3 we describe the sensitivity to physics parameters in the $B_s^0 \to J/\psi\phi$ channel using the unbiased and biased selections. In addition, we studied the effects of low signal statistics on the fitter stability. We also study the systematic error imposed by the proper time acceptance of the biased selection. Finally the determination of ϕ_s in 2010 data is reviewed in Section 5.4. The full ϕ_s measurement made with $36\,pb^{-1}$ of integrated luminosity is published in [104]. It uses the selection developed in this thesis, the small difference between the fitter used by the collaboration and the one developed in this thesis are given in the same section.

5.1 Fitter description

The determination of the physical parameters in $B_s^0 \to J/\psi\phi$ channel is done by the means of an unbinned maximum-likelihood fit of the probability density function to the dataset. The pdf comprises two main components:

- signal pdf depends on the theoretical description of the $B_s^0 \to J/\psi\phi$ events, and on the detector effects on this pdf;
- Background pdf is an empirical description of the different background sources.

The likelihood function for N events can be written as:

$$\mathcal{L} = \prod_e^N \mathcal{P}(X_e; \lambda_{\text{phys}}, \lambda_{\text{det}}) \,, \tag{5.1}$$

where

- X_e are the measured event physics observables. These are proper time t, decay angles Ω, B mass m and tagging decision of the initial B flavor tag d;
- $\lambda_{\text{phys}} = \{\Gamma_s, \Delta\Gamma_s, R_\perp, R_0, \delta_\perp, \delta_\parallel, \Delta m_s, \phi_s\}$ are discussed in Chapter 1;
- λ_{det} are the detector parameters: mass resolution σ_m, proper time resolution σ_t, mistag rate ω and the background parameters: prompt Gaussian parameters σ and mean values and parameters of long-lived background component τ_{LL_1}, τ_{LL_2} and long-lived resolution parameters, discussed in Chapter 3.

The pdf can be written then as:

$$\mathcal{P} = f_{\text{sig}}\mathcal{S} + (1 - f_{\text{sig}})\mathcal{B} \,, \tag{5.2}$$

where f_{sig} is the expected overall signal fraction.

Signal pdf

The signal pdf is described by the equation:

$$\mathcal{S}(X_e; \lambda) \quad \propto \quad \mathcal{S}_1(t, q, \Omega; \lambda_{\text{phys}}, \lambda_{\text{det}})\ \mathcal{S}_2(m; \lambda_{\text{phys}}, \lambda_{\text{det}})\ \epsilon(t, \Omega), \tag{5.3}$$

where it comprises the following parts:

- $\mathcal{S}_1$, the differential decay rate for the $B_s^0 \to J/\psi\phi$ channel convoluted with the proper time resolution model;
- $\mathcal{S}_2$, the mass pdf described by the two (or more) Gaussian distributions to account for the detector smearing on the B_s^0 mass;
- ϵ, the acceptance function which describes effects of the detector and analysis cuts on the proper time and angular distributions.

The theoretical pdf is divided into two main parts; time-dependent functions and angular-dependent functions.

Flavor tagging effects appear in the time-dependent functions of the differential decay rates of the $B_s^0 \to J/\psi\phi$ channel. Inserting the tagging decision ($q = -1, 0, +1$) and the dilution term ($D = 1 - 2\omega$) in front of the mixing terms accounts for tagging effects:

$$\begin{aligned}
(1-\omega)|A_0(t)|^2 + \omega|\bar{A}_0(t)|^2 &= |A_0(0)|^2 e^{-\Gamma_s t} \times \Big[\cosh\left(\frac{\Delta\Gamma_s t}{2}\right) \\
&\quad - \cos\phi_s \sinh\left(\frac{\Delta\Gamma_s t}{2}\right) + (1-2\omega)\ \sin\phi_s \sin(\Delta m_s t)\Big], \quad (5.4)\\
(1-\omega)|A_\parallel(t)|^2 + \omega|\bar{A}_\parallel(t)|^2 &= |A_\parallel(0)|^2 e^{-\Gamma_s t} \times \Big[\cosh\left(\frac{\Delta\Gamma_s t}{2}\right) \\
&\quad - \cos\phi_s \sinh\left(\frac{\Delta\Gamma_s t}{2}\right) + (1-2\omega)\ \sin\phi_s \sin(\Delta m_s t)\Big], \quad (5.5)\\
(1-\omega)|A_\perp(t)|^2 + \omega|\bar{A}_\perp(t)|^2 &= |A_\perp(0)|^2 e^{-\Gamma_s t} \times \Big[\cosh\left(\frac{\Delta\Gamma_s t}{2}\right) \\
&\quad + \cos\phi_s \sinh\left(\frac{\Delta\Gamma_s t}{2}\right) - (1-2\omega)\ \sin\phi_s \sin(\Delta m_s t)\Big], \quad (5.6)\\
(1-\omega)\Im\{A_\parallel^*(t)A_\perp(t)\} + \omega\Im\{\bar{A}_\parallel^*(t)\bar{A}_\perp(t)\} &= |A_\parallel(0)||A_\perp(0)|\, e^{-\Gamma_s t}\Big[-\cos(\delta_\perp - \delta_\parallel)\sin\phi_s \sinh\left(\frac{\Delta\Gamma_s t}{2}\right) \\
&\quad + (1-2\omega)\ \Big\{\sin(\delta_\perp - \delta_\parallel)\cos(\Delta m_s t) - \cos(\delta_\perp - \delta_\parallel)\cos\phi_s \sin(\Delta m_s t)\Big\}\Big], \quad (5.7)\\
(1-\omega)\Re\{A_0^*(t)A_\parallel(t)\} + \omega\Re\{\bar{A}_0^*(t)\bar{A}_\parallel(t)\} &= |A_0(0)||A_\parallel(0)|\, e^{-\Gamma_s t}\cos(\delta_\parallel) \times \\
&\quad \Big[\cosh\left(\frac{\Delta\Gamma_s t}{2}\right) - \cos\phi_s \sinh\left(\frac{\Delta\Gamma_s t}{2}\right) + (1-2\omega)\ \sin\phi_s \sin(\Delta m_s t)\Big], \quad (5.8)\\
(1-\omega)\Im\{A_0^*(t)A_\perp(t)\} + \omega\Im\{\bar{A}_0^*(t)\bar{A}_\perp(t)\} &= |A_0(0)||A_\perp(0)|\, e^{-\Gamma_s t}\Big[-\cos\delta_\perp \sin\phi_s \sinh\left(\frac{\Delta\Gamma_s t}{2}\right) \\
&\quad + (1-2\omega)\ \{\sin(\delta_\perp)\cos(\Delta m_s t) - \cos(\delta_\perp)\cos\phi_s \sin(\Delta m_s t)\}\Big], \quad (5.9)
\end{aligned}$$

The $\overline{B}_s^0$ pdf is obtained by swapping the sign of the terms involving $\sin(\Delta m_s t)$. In the untagged pdf where $d = 0$, the dilution term in the Equations 5.4 to 5.9 vanishes. This part is less sensitive to the ϕ_s parameter than the tagged one. This is because mixing terms, dependent on $sin(\phi_s)$, disappear when the tagging information is absent. Notice that the S-wave contribution to the $B_s^0 \to J/\psi\phi$ channel is neglected.

To account for the finite detector resolution on proper time, the theoretical pdf is convoluted with Gaussian(s) function(s):

$$\begin{aligned}
\mathcal{S}_1'(t, \Omega, q; \lambda_{\text{phys}}, \lambda_{\text{det}}, R) &= \int_{t'=0}^{\infty} dt'\, \mathcal{S}_1(t, \Omega, q; \lambda_{\text{phys}}) G(t' - t; R) \\
&\equiv \mathcal{S}_1(t, \Omega, q; \lambda_{\text{phys}}) \otimes G(t' - t; R), \quad (5.10)
\end{aligned}$$

where t' denotes the true proper time. The parameters $R = \{f_1, \sigma_{t1}, \sigma_{t2}\}$ describe the proper time resolution model and are defined in time units (ps).

The angular resolution functions is studied in Chapter 3. In the study, we neglect the angular resolution in the signal pdf. This is justified by the small effect of such simplification in the ϕ_s determination [105].

Sculpting of proper time and angular variable distributions were discussed in Chapter 3. As explained there, proper time Sculpting comes either from detector effects or due to analysis cuts. This is valid for the sculpting of angular variable distributions, also called "acceptance functions". Those functions are calculated either from data or from Monte Carlo. To take those into account we multiply the theoretical pdf by the acceptance function(s) as shown in Equation 5.3.

Background pdf:

There are two main background sources in the $B_s^0 \to J/\psi\phi$ channel: long-lived and prompt. The background pdf is described by the following equation:

$$\mathcal{B}(m;\lambda_{\rm det})\,\mathcal{B}(t;\lambda_{\rm det})\,\mathcal{B}(\Omega), \tag{5.11}$$

composed of three main parts:

- mass pdf;
- proper time pdf;
- angular pdf.

The mass distribution for both background types (prompt and long-lived) follows an exponential distribution:

$$\mathcal{B}(m;\lambda_{\rm det}) \;=\; N_{det}\,{\rm e}^{-\alpha_{det}}\,, \tag{5.12}$$

Modeling the proper time and angular distributions is done using a fit of empirical functions on the mass distribution side bands. The description of the long-lived proper time distribution uses exponential function convoluted with a resolution function different from that of the signal. The proper time distribution of prompt background is simulated with a multicomponent Gaussian function. The angular distributions are considered flat in the fit (we neglect the unique shape of the $cos\psi$ in the Monte Carlo simulation samples).

No correlation is found between the angular and proper time distributions for both background sources. This leads to separate the proper time and angular empirical pdfs. Chapter 3 contains a detailed description of the angular and proper time descriptions in Monte Carlo.

5.2 ϕ_s fit in full simulation

To check the fitter program we test it first against the full Monte Carlo simulation of $B_s^0 \to J/\psi\phi$ (version MC10).

To account for the geometrical effects of the detector on the angular variables a 3D acceptance function is determined using the Monte Carlo information. Many approaches are studied in LHCb to account for acceptance effects:

- multiply the signal pdf by a 3D histogram calculated from the Monte Carlo signal sample. One can further use Legendre or Tchebytchev polynomials (as in Ref. [106]) fitted to the 3D histogram to extract the 3D acceptance function as explained in Ref. [107];
- account for the acceptances using a normalization weights calculated from the 3D histogram in the likelihood function [105];
- use the p_T spectrums and reconstruction efficiencies to extract the acceptance histograms from data. This approach is studied in Ref. [108].

In our fitter we account for the angular acceptance using the 3D histogram. In the published analysis with 2010 data the 3D histogram is fitted with Legendre polynomial to smooth the binning effects. The acceptance histogram consists of 20 bins in each angular variables meaning 8 000 bins for the 3D histogram. The bin coordinates are the division of the true angular variables by the theoretical expectations.

It is necessary to use a 3D histogram and not a simple acceptance projections onto angular variables plane, because they include the correlation between the angular distortions. In case of proper time acceptance, a proper time function should be also taken into account in the signal pdf. In general, neglecting the angular acceptances in the fit procedure biases $R_\perp, R_0, \delta_\perp, \delta_\parallel$ but would also bias $\Gamma_s, \Delta\Gamma_s$ parameters as the proper time and angular variables correlation is not trivial and depends on the $\Delta\Gamma_s$ values [99].

Figure 5.1, shows the 3D angular acceptance and the proper time function in case of the unbiased selection, $\sim$ 500 000 events are fitted (218 000 untagged events, 254 000 tagged events).

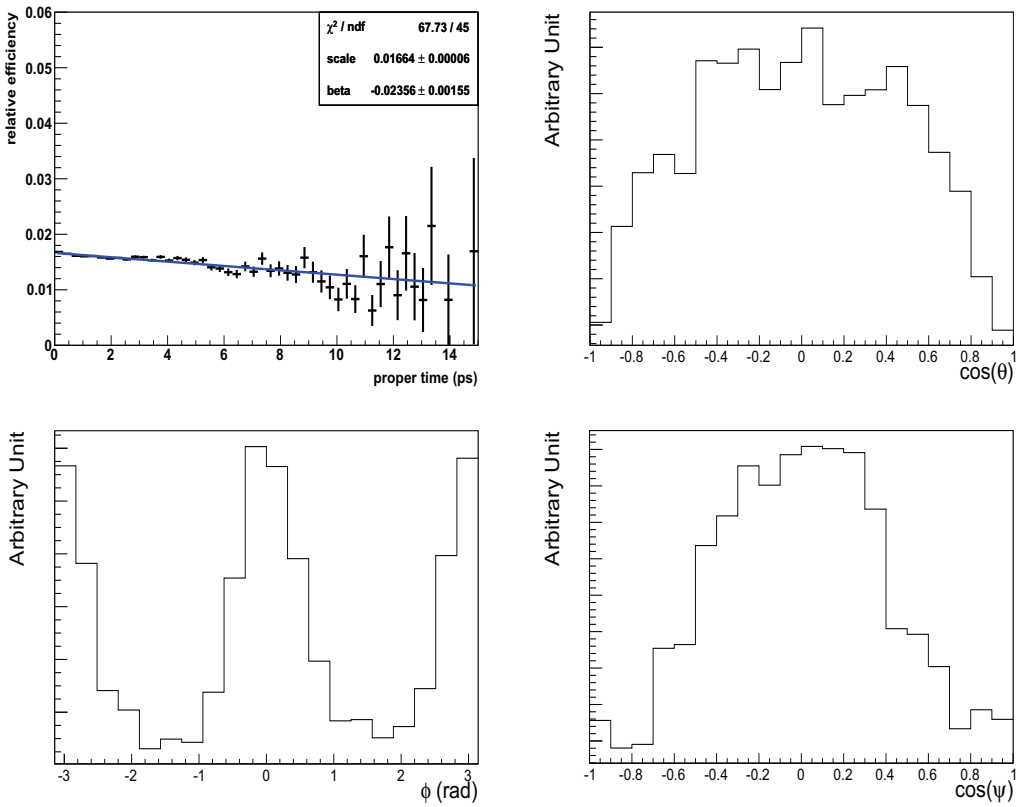

Figure 5.1: Proper time acceptance function (top left) and projection of the determined 3D angular acceptance in the transversity basis and the proper time acceptance used in the signal fit to the Monte Carlo data ‘(MC2010).

In the fit, all detector and physical parameters are float; a simple Gaussian for the resolution model is used. Fit results are shown in Table 5.1, where all the physical parameters are correctly returned by the fitter with less than 2σ deviation from the input values. Errors are correctly estimated and the fit converges with no problems. Figure 5.2 shows the projection of the signal pdf onto the angular variables and proper time planes.

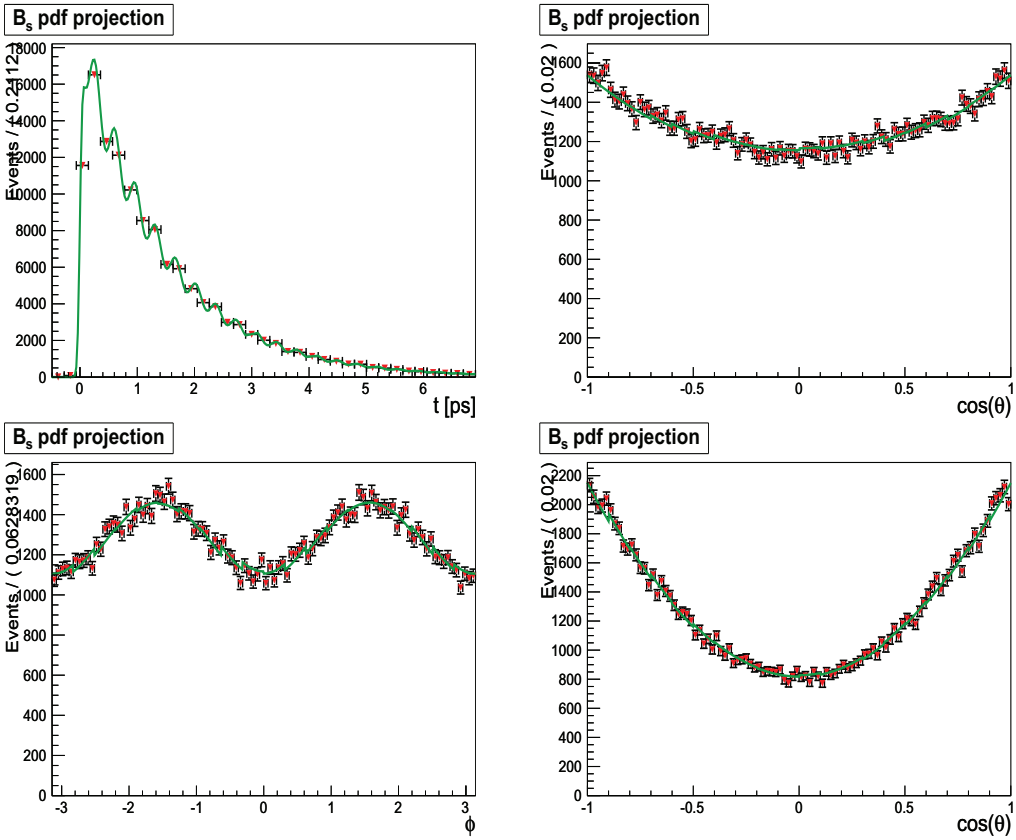

Figure 5.2: Left: the $B_s^0 \to J/\psi\phi$ MC10 data and the projections of signal Pdf including the angular and proper time effects, only B_s^0 events are shown.

Parameter	Fit result and error	σ from input
τ_s	1.468 ± 0.003 ps	-1.2
$\Delta\Gamma_s$	0.055 ± 0.005 ps^{-1}	-1.1
$\lvert A_\perp \rvert^2$	0.159 ± 0.001	1.
$\lvert A_0 \rvert^2$	0.601 ± 0.001	0.84
$\delta_\parallel$	2.511 ± 0.015 rad	1.
$\delta_\perp$	-2.079 $\pm$ 0.043 rad	0.7
Δm_s	17.78 ± 0.011 ps^{-1}	1.8
ϕ_s	-0.713 $\pm$ 0.021 rad	-0.62

Table 5.1: Table showing the fit results and errors for the fitted parameters (physical) with the standard deviation with respect to input values.

5.3 Toy Monte-Carlo studies

In order to determine the sensitivity of the LHCb experiment to the ϕ_s phase, a large number of simulations should be generated with different seeds and fitted to the same pdf used to generate the events. The distributions of the values and pull are then checked for any anomaly (e.g. overestimation of the errors or a bias on the estimation of a given parameter). The pull distribution for the parameter x is calculated as:

$$\text{pull} = \frac{x_{\text{fit}} - x_{\text{input}}}{\sigma_x}, \tag{5.13}$$

where the x_{fit} is the value of the parameter given by the fit, x_{input} is the true value of the parameter used in the generation of the toy, and σ_x is the error estimated by the fit.

This task seems nearly impossible if one considers the production of full Monte Carlo simulation. A toy Monte Carlo or fast Monte Carlo simulation are tools that enable us to generate rapidly a large number of experiments using a physics pdf. Toy Monte Carlo is useful to study the sensitivity of given parameters or study the effects on parameters.

The toy Monte Carlo is also useful to test the reliability of the statistical estimator used in the fit. An example is given acceptin 5.3.2 where we study the likelihood fit behavior with low number of signal events.

Finally, the toy Monte Carlo is used to study the systematic effects from different parameters of the analysis. One can generate data with standard value of the parameter under study, while varying its value in the pdf. In 5.3.3, we explore the systematic of non-trivial proper time acceptance function in the context of the biased selection.

Our toy Monte Carlo uses a collection of Root [109] and RooFit [110] classes that helps generate events using the accept/reject method and fit those events to $B_s^0 \to J/\psi\phi$ channel pdf using Minuit program [111].

5.3.1 Fitter validation and sensitivity studies

We define the sensitivity of our analysis to a parameter x as the Gaussian-width of the fitted distribution obtained using the toy experiments. The pull distribution of a given parameter provides two valuable informations:

- the first is the information about the bias on the estimation, since the mean of the distribution should be compatible with zero;
- the second information is the standard deviation of the pull distribution. When this parameter is found to be compatible with unity

it means that the error given by the fitter is correctly estimated (> 1 implies to an underestimation of the error).

In order to get a unbiased fit the pull should be centered around zero and its width should be compatible with 1. We explore first the sensitivity on ϕ_s and other physical parameters of the unbiased selection scenario. We fit the physical parameters: $\tau_s, \Delta\Gamma_s, R_\perp, R_0, \delta_\perp, \delta_\parallel, \phi_s$, while we fix[1] Δm_s. Parameters input values are found in Table 5.2a.

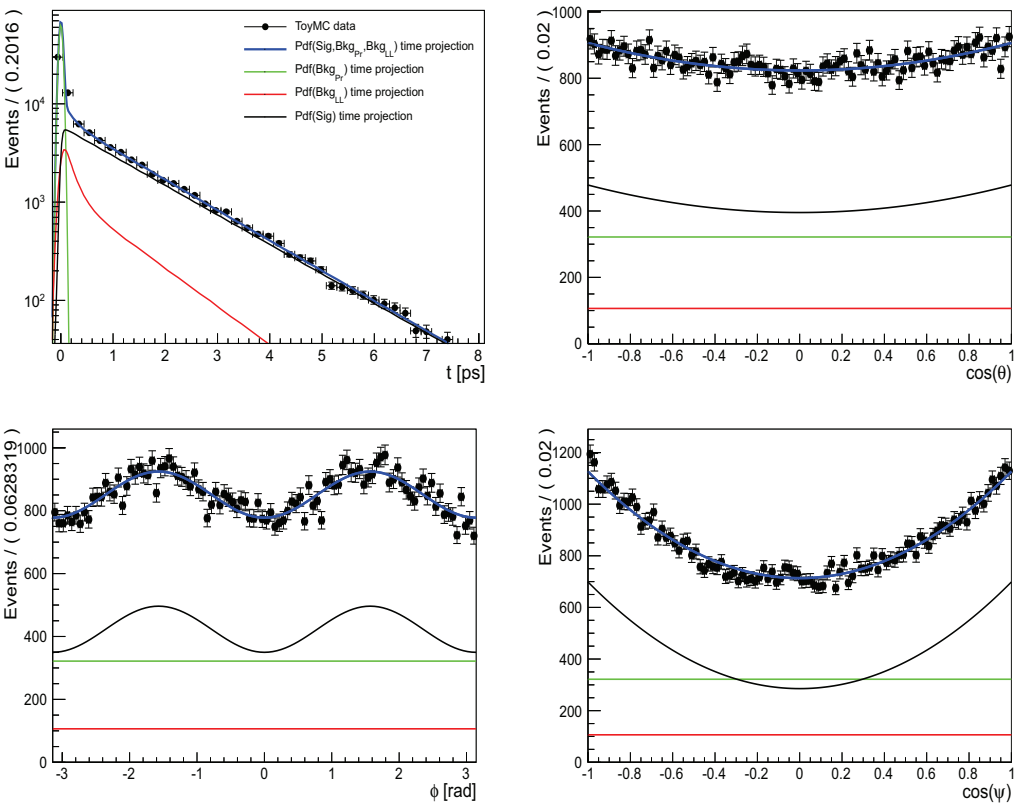

Figure 5.3: Left: pdf projections (unbiased scenario) onto: proper time (Top Left), $cos\theta$ (Top Right), ϕ (Bottom Left) and $cos\psi$ (Bottom Right), black line is the signal component, green is for prompt component, red is for the long-lived component.

The background parameters are fixed. In data we measure those parameters from the sidebands of the mass distribution and fix them in the

[1] this has a negligible effect on the fit as its correlation with other parameters is proved to be small.

signal mass window[2].

Toys are generated with the unbiased configuration described in the Table 3.7 (index) that summarizes the full simulation results detailed in Chapter 3. We plot the distribution of proper time and angular variables for the unbiased scenario using one toy Monte Carlo in Figure 5.3. Signal and background events tagged as B_s^0 are plotted. Distributions of fitted parameters and their pulls are shown in Figures 5.4, 5.5 and 5.8. The sensitivity to ϕ_s using the unbiased configuration is $\sigma_{\phi_s} = 0.042 \pm 0.002$ rad at $2\,fb^{-1}$ of integrated luminosity. The sensitivity of ϕ_s depends on the annual yield, proper time resolution and effective tagging efficiency. The ϕ_s sensitivity obtained is a function of tagging power, proper time resolution and signal yield, a detailed study accounting for those elements is found in [112] and in [5].

A similar study is done to explore the sensitivity on ϕ_s and physical parameters for the biased scenario. toys are generated using the configuration in Chapter 3, where we follow the same fitting scheme as explained above. We plot the proper time and angular distribution for the biased scenario using one toy Monte Carlo in Figure 5.7, events shown are those of signal and background where the B meson is tagged as B_s^0.

In Table 5.2c and 5.2b, we give all the mean the RMS values for the all physical parameters for both biased and unbiased scenarios. Pull distributions are normal showing that the parameters are correctly calculated by the fit. For the $\delta_\perp$ the estimation is bias, this is still under investagation.

The sensitivity obtained with the biased selection is 0.028 ± 0.001 rad at $2\,fb^{-1}$ at 7 TeV of integrated luminosity, much higher than that of the unbiased one. This is simply explained by the higher signal yield in the biased case. Note that the sensitivity in the biased case is obtained with no trigger.

[2] range of the mass window is dependent on the mass resolution of the signal events.

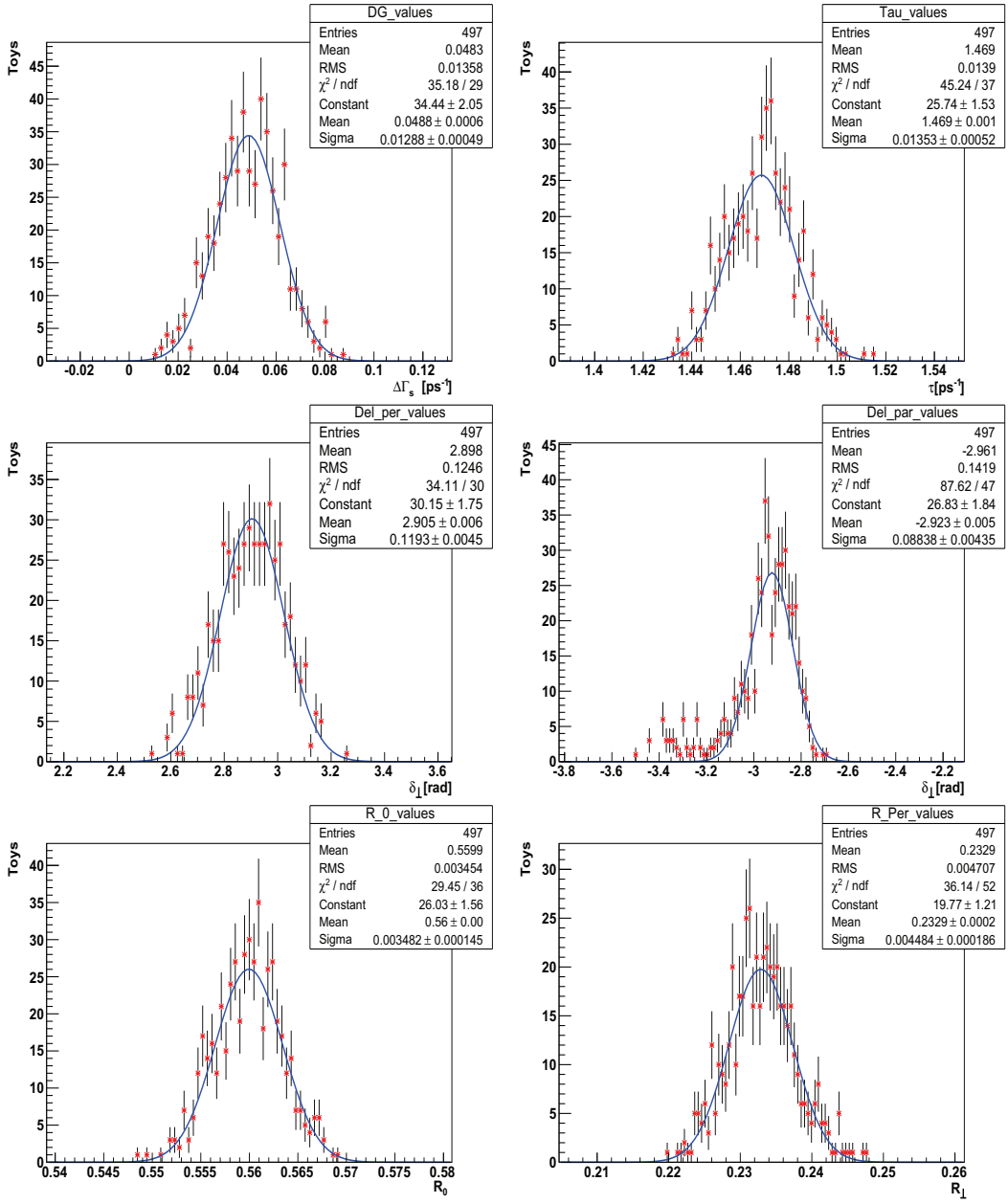

Figure 5.4: Distributions for fitted parameters ($\Delta\Gamma_s, \tau_s, R_\perp, R_0, \delta_\perp, \delta_\parallel$) with the unbiased configuration ($\sim$ 500 toys).

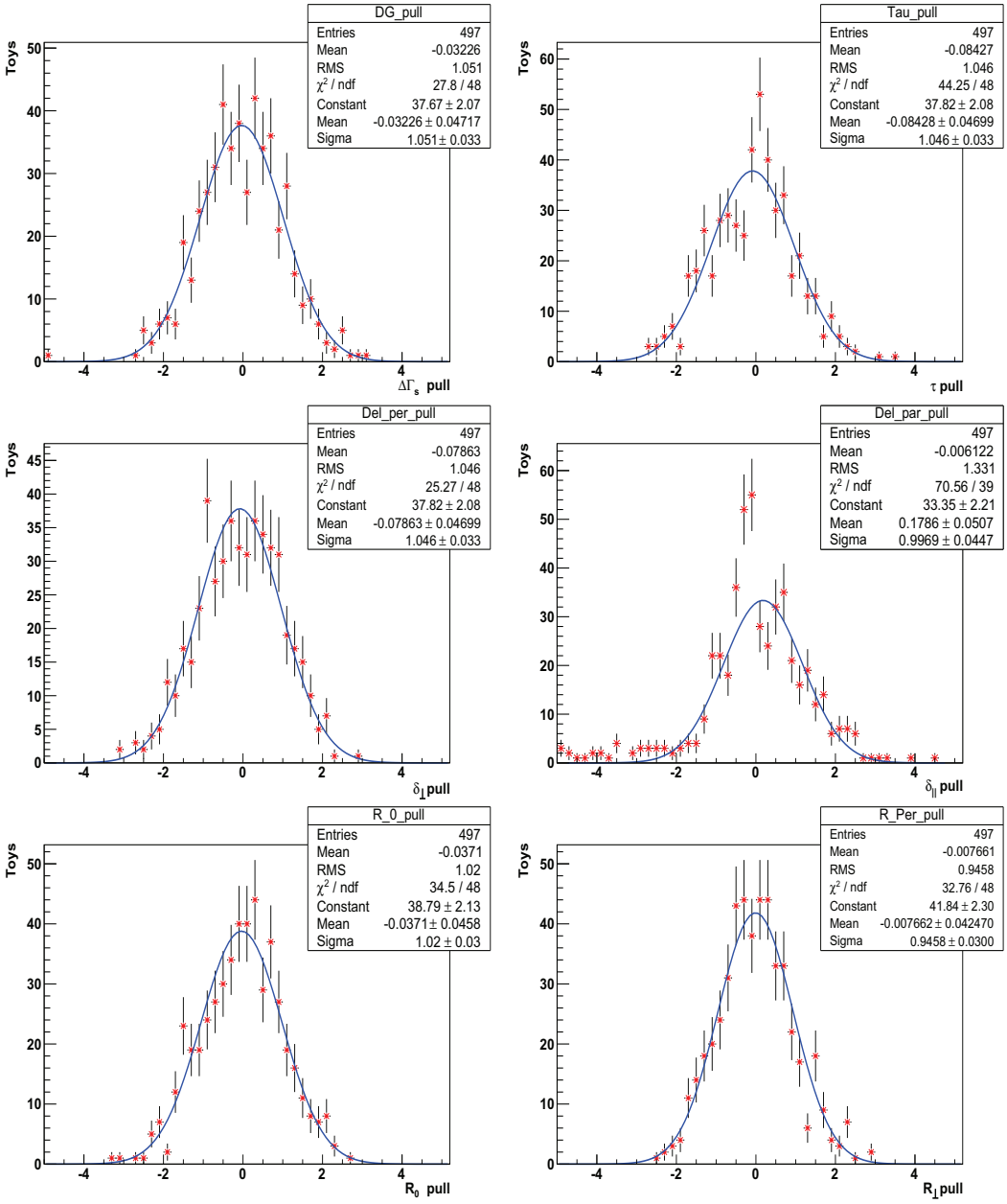

Figure 5.5: Pull distributions for fitted parameters ($\Delta\Gamma_s, \tau_s, R_\perp, R_0, \delta_\perp, \delta_{||}$) with the unbiased configuration ($\sim$ 500 toys).

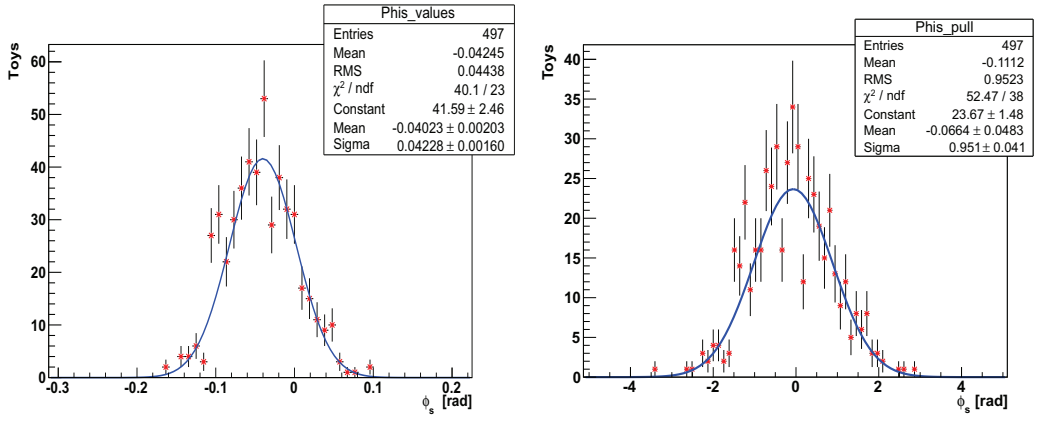

Figure 5.6: Left: distribution for ϕ_s parameter with the unbiased configuration. Right: pull distribution for ϕ_s parameter with the unbiased configuration ($\sim$ 500 Toy).

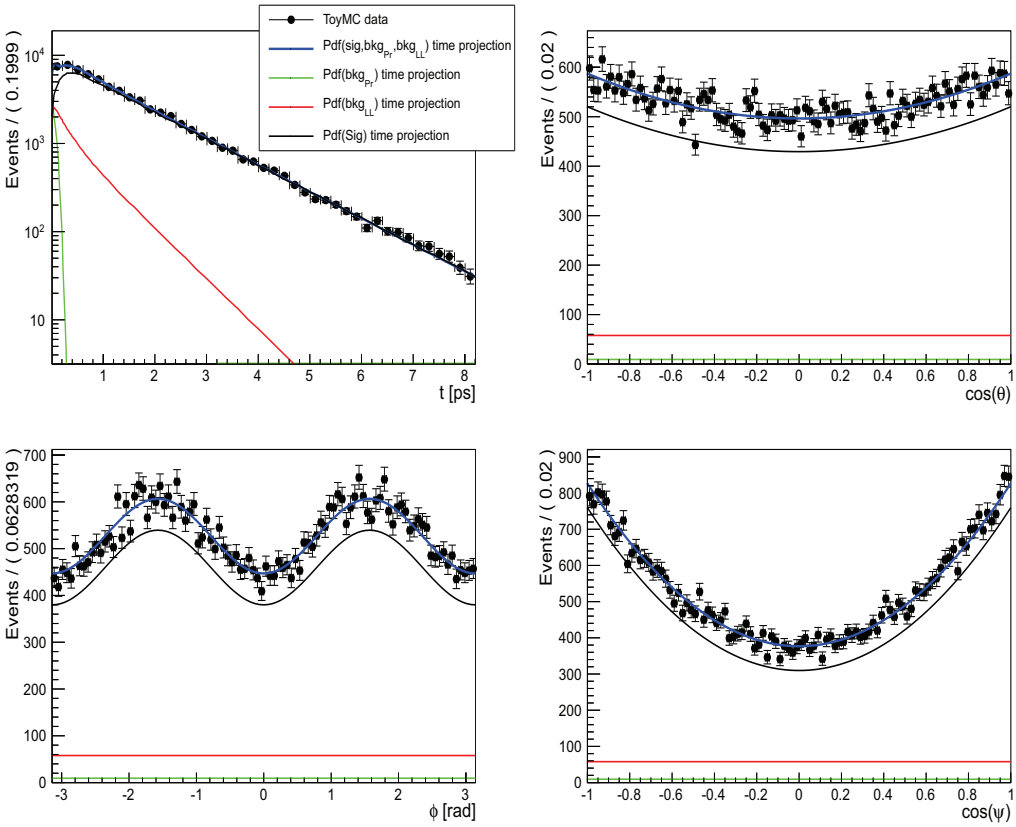

Figure 5.7: Left: pdf projections (biased scenario) onto various planes: proper time (Top Left), $cos\theta$ (Top Right), ϕ (Bottom Left) and $cos\psi$ (Bottom Right), the black line is the signal component, the green is for the prompt component, the red is for the long-lived component.

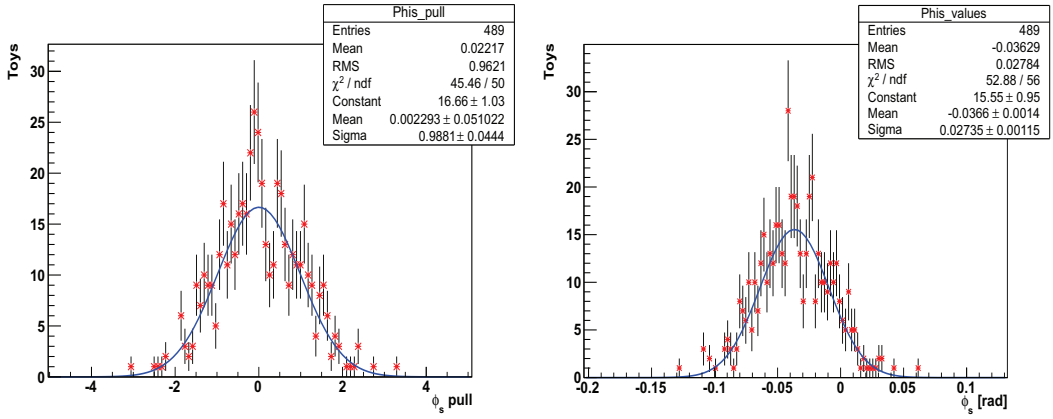

Figure 5.8: Left: distribution for ϕ_s parameter with the unbiased configuration. Right: pull distribution for ϕ_s parameter with the unbiased configuration ($\sim$ 500 toys).

Parameter	Generator value
τ_s ps^{-1}	1.47
$\Delta\Gamma_s$ ps^{-1}	0.049
$\lvert A_\perp\rvert^2$	0.233
$\lvert A_0\rvert^2$	0.56
$\delta_\parallel$ rad	+2.91
$\delta_\perp$ rad	+2.93
ϕ_s	-0.0368

(a) Generation parameters

	Sensitivity	Pull mean	Pull width
τ_s ps^{-1}	0.0135 ± 0.0005	-0.08 ± 0.05	1.05 ± 0.03
$\Delta\Gamma_s$ ps^{-1}	0.0128 ± 0.0005	-0.03 ± 0.05	1.05 ± 0.03
$\lvert A_\perp\rvert^2$	0.0045 ± 0.0002	0.00 ± 0.04	0.95 ± 0.03
$\lvert A_0\rvert^2$	0.0034 ± 0.0001	-0.04 ± 0.05	1.02 ± 0.03
$\delta_\parallel$ rad	0.088 ± 0.0004	0.17 ± 0.05	0.99 ± 0.05
$\delta_\perp$ rad	0.119 ± 0.005	-0.07 ± 0.05	1.05 ± 0.03
ϕ_s rad	0.042 ± 0.002	-0.07 ± 0.05	0.95 ± 0.04

(b) Parameter sensitivity and pull mean and width (unbiased scenario)

	Sensitivity	Pull mean	Pull width
τ_s ps^{-1}	0.0081 ± 0.0002	0.03 ± 0.04	0.99 ± 0.03
$\Delta\Gamma_s$ ps^{-1}	0.0080 ± 0.0003	0.06 ± 0.04	0.99 ± 0.04
$\lvert A_\perp\rvert^2$	0.0021 ± 0.0001	-0.09 ± 0.04	0.96 ± 0.03
$\lvert A_0\rvert^2$	0.0021 ± 0.0000	0.02 ± 0.05	1.01 ± 0.04
$\delta_\parallel$ rad	0.086 ± 0.002	0.14 ± 0.04	1.08 ± 0.03
$\delta_\perp$ rad	0.075 ± 0.002	-0.02 ± 0.05	1.03 ± 0.03
ϕ_s rad	0.028 ± 0.001	0.00 ± 0.05	0.99 ± 0.04

(c) Parameter sensitivity and pull mean and width (biased scenario)

Table 5.2: Results from toy Monte Carlo study with ~ 500 toys. Table 5.2a shows the physics parameters used to produce the toy data. Table 5.2b shows the sensitivity on the parameters and the pull mean and width using the unbiased configuration. Table 5.2c shows the sensitivity on the parameters and the pull mean and width using the biased configuration.

5.3.2 Low statistics studies

As seen in the previous section, our fit estimates the parameters and their errors correctly at 2 fb^{-1} of integrated luminosity. The study, carried out in this section, aims at testing the likelihood estimator for a low signal yield. Scanning ranges of integrated luminosity will provide a threshold beyond which likelihood estimator is proved biased.

We repeat this study for two values of ϕ_s: a small $\phi_s \sim -0.0368$ rad that corresponded to Standard Model expectation and higher $\phi_s \sim -0.6$ rad corresponding to a New Physics scenarios. The fit failure criterion is the status of the error covariance matrix, where a the fit is considered successful only when this matrix is calculated accurately by the fitter. The configuration of the Toy Monte carlo is the same as the one used in the previous section, where the unbiased configuration is used in the generation.

$\mathcal{L}_{int}$ Signal events	100 pb^{-1} 3000	200 pb^{-1} 6000	400 pb^{-1} 12 000	1 fb^{-1} 30 000
ϕ_s pull mean	0.03 ± 0.05	0.05 ± 0.06	0.01 ± 0.05	0.04 ± 0.06
ϕ_s pull width	1.00 ± 0.01	0.9 ± 0.04	0.92 ± 0.04	0.94 ± 0.04
Fit failure	2%	1%	no failure	no failure
Global correlation	0.29 ± 0.02	0.23 ± 0.01	0.23 ± 0.01	0.18 ± 0.01

Table 5.3: Summary of low statistics study in the case where $\phi_s = -0.04$ rad.

$\mathcal{L}_{int}$ Signal event	100 pb^{-1} 3000	200 pb^{-1} 6000	400 pb^{-1} 12 000	1 fb^{-1} 30 000
ϕ_s pull mean	0.24 ± 0.07	0.14 ± 0.07	0.03 ± 0.05	0.08 ± 0.06
ϕ_s pull width	0.92 ± 0.01	0.95 ± 0.07	0.95 ± 0.04	0.94 ± 0.05
Fit failure	3%	1%	no failure	no failure
Global correlation	0.33 ± 0.01	0.32 ± 0.01	0.27 ± 0.01	0.20 ± 0.01

Table 5.4: Summary of low statistics study in the case where $\phi_s = -0.6$ rad.

Tables 5.3 and 5.4 present the results of this study on ϕ_s parameter and status of the fit with a range of luminosity for two different values of ϕ_s. It should be noted here that the yields used in the toys Monte Carlo generation is scaled according to our findings in [5].

The outcome of the study points to the fact that the ϕ_s value is biased when signal yield is lower than 6 000 events for high values of ϕ_s. This

bias, though, is rather small. In addition, for both New Physics and Standard Model values of ϕ_s, we notice a failure rate of $\sim$ 2% under 6 000 events. For other parameters, we find that errors on strong phases are found to be underestimated and the $|A_{||}|^2$ is biased for the same range of luminosity.

The conclusion is that the likelihood estimator when fitted to less than $\sim$ 6000 events is not reliable. An interval estimate rather than a point estimate should be used to determine the ϕ_s phase at low signal statistics.

5.3.3 Systematic studies

Sources of systematic uncertainties on the ϕ_s measurement are studied in detail using Monte Carlo in [113], [107] and [105] and summarized in [5].

In this section, we present an ensemble of studies we carried out in the context of the biased selection developed in Chapter 3 at $\sqrt{s} = 7\,\text{TeV}$ and integrated luminosity of $2\,\text{fb}^{-1}$. The proper time acceptance determination is based on either Monte Carlo simulation or on data itself. Wrong determination of the proper time acceptance function is a potential source for systematic error.

Here we consider three cases of systematic error:

- neglecting to correct for the proper time acceptance effect;
- miscalculation of the slope of the proper time acceptance;
- neglecting possible differences between B_s^0 proper time acceptance and that of $\overline{B}_s^0$.

For all these three cases we use the biased selection configuration described in Table 3.10.

At first we try to account for the absence of the acceptance function in the pdf. In this study, we generate $\sim$ 500 toys with the proper time acceptance function and we fit using a pdf that neglect this function. In Table 5.5, we quote the results of this study. It is clear that systematic error in the case we discard the acceptance function in the fit is small in the case of tiny value of ϕ_s.

The second case of systematic study accounts for any ill-determination of the slope of the proper time acceptance. In Chapter 3, we presented a method to extract the proper time acceptance directly from the data. The function used is:

$$\text{Acc}_{\text{fit}} = \frac{(s \times t_{\text{reco}})^3}{1 + (s \times t_{\text{reco}})^3} \tag{5.14}$$

ϕ_s generated (rad)	ϕ_s fitted (rad)	ϕ_s pull mean	systematic error [rad]
-0.0368	-0.037 ± 0.001	-0.01 ± 0.05	$-$
-0.6	-0.607 ± 0.001	-0.17 ± 0.05	-0.007

Table 5.5: Table showing the values, pull and systematic error for ϕ_s parameter in the case of total discard of the proper time acceptance in the fit (Standard Model and New Physics values of ϕ_s are considered).

The slope parameter in the function is crucial for describing the bias of the proper time distribution. The slope is calculated using sPlot technique under the hypothesis that background and signal behave the same inside and outside the mass window. Any discrepancies of the background proper time behavior between events inside the signal mass window and events in the mass side bands can cause a wrong calculation of the slope.

To study this effect we fit using a fixed slope that differs from the input value by 10% off in the pdf, our results are given in Tables 5.6 .

ϕ_s generated (rad)	ϕ_s fitted (rad)	ϕ_s pull mean	systematic error [rad]
-0.0368	-0.035 ± 0.001	-0.06 ± 0.06	$-$
-0.6	-0.602 ± 0.001	-0.10 ± 0.05	-0.002

Table 5.6: Table showing the values, pull and systematic error for ϕ_s parameter in the case of ill-determination (10%) of the slope of proper time acceptance in the fit (Standard Model and New Physics values of ϕ_s are considered).

We find no large systematic effect, where in the worst case ($\phi_s = -0.6\,\text{rad}$) the systematic error is less than 10% of the statistical error.

The third and last case is where differences between B_s^0 and $\overline{B}_s^0$ acceptance effects are neglected in the fit. To study this case, we generate the B_s^0 events using a proper time acceptance that is different from the one used in simulating the $\overline{B}_s^0$ events (10% and 20% difference in the slope parameter). The fit is performed using a proper time acceptance with an average slope parameter. Tables 5.7 and 5.8 present our results for this case.

The systematic error, in case of different acceptance for $\overline{B}_s^0$ and B_s^0 events, is only dominant for Standard Model value of ϕ_s and the B_s^0, $\overline{B}_s^0$ acceptance slope difference is 20%.

the systematic error in the context of biased selection is only significant in later case, which is an extreme one. This systematic effect can be

ϕ_s generated (rad)	ϕ_s fitted (rad)	ϕ_s pull mean	systematic error [rad]
-0.0368	-0.032 ± 0.001	0.13 ± 0.05	-0.005
-0.6	-0.601 ± 0.001	-0.03 ± 0.05	$-$

Table 5.7: Table showing the values, pull and systematic error for ϕ_s parameter in the case 10% different acceptance for $\overline{B}_s^0$ and B_s^0 events while using an average acceptance in the fit (Standard Model and New Physics values for ϕ_s are considered).

ϕ_s generated (rad)	ϕ_s fitted (rad)	ϕ_s pull mean	systematic error [rad]
-0.0368	-0.027 ± 0.001	0.28 ± 0.05	-0.06
-0.6	-0.595 ± 0.002	0.12 ± 0.05	-0.005

Table 5.8: Table showing the values, pull and systematic error for ϕ_s parameter in the case 20% different acceptance for $\overline{B}_s^0$ and B_s^0 events while using an average acceptance in the fit (Standard Model and New Physics values for ϕ_s are considered).

avoided by extracting the proper time acceptance function for $\overline{B}_s^0$ and B_s^0 events separately.

5.4 ϕ_s measurement with 2010 data

In this section we present the determination of the ϕ_s parameter in the $B_s^0 \to J/\psi\phi$ channel using the data sample collected during 2010. The results presented here are published in [104]. The main differences between our fitter and the one used by the collaboration for the publication are:

- our fitter only uses a fixed average mistag rate whereas the fitter used for the publication is equipped to take into account an event-by-event mistag rate;
- our fitter uses a 3D histogram to account for the angular acceptances, the fitter used for the publication one parametrize it using Legendre polynomial.

Next we provide a review of the study performed using the LHCb fitter with the 2010 data. This fit yielded the first determination of the ϕ_s at LHCb.

The integrated luminosity of the data collected and fully reconstructed and analyzed during 2010 is $\sim 36\,\text{pb}^{-1}$ at $\sqrt{s} = 7\,\text{TeV}$. The number of events corresponding to this luminosity is shown in the Table 5.9. In the sample we distinguish between the:

- unbiased sample of events passing the unbiased selection set of cuts and the unbiased trigger lines;
- biased sample of events passing the unbiased selection set of cuts but passed the *biased* trigger lines (see Chapter 2 for details).

The *biased* sample represents 30% of the tagged events. Enhancing the statistical significance of the measurement requires considering this part of the sample too. Therefore, the analysis comprises two different approaches (unbiased and biased) with two different proper time acceptance functions.

The unbiased analysis is done with the cut on the proper time $t > 0.3\,\text{ps}$, in order to reduce the prompt contribution in the data sample, simplify the fit model. This cut reduces the yield as observed in Table 5.9, but does not affect the ϕ_s sensitivity.

A per-event mistag probability is used. Only opposite-side taggers are considered to get the mistag combination. The estimated per-event mistag probability is calibrated using the $B^+ \to J/\psi K^+$ channel where a linear dependence is assumed between the estimated mistag probability and the

	All	($t > 0.3$ ps)	Signal yield	Signal yield ($t > 0.3$)
unbiased-only	38 225	250	230 ± 53	161 ± 13
biased-only	653	345	208 ± 16	196 ± 15
both	1 123	521	398 ± 22	400 ± 20
total	40 001	1116	836 ± 60	757 ± 28

Table 5.9: Number of $B_s^0 \to J/\psi\phi$ selected events and fitted signal yields for all events with invariant mass in $[5200, 5550]$ GeV/c^2 and proper time in $[-1, 14]$ ps. This is from a mass only fit, hence relatively large errors on the yields for the full time range are obtained.

σ_1 [fs]	σ_2 [fs]	σ_3 [fs]	f_2	f_3
33.7 ± 1.0	64.6 ± 1.9	184 ± 14	0.46 ± 0.04	0.017 ± 0.004

Table 5.10: Resolution parameters extracted from the fit explained in the text. The uncertainties are statistical only and highly correlated [86].

actual one. The parameterization of this dependence is presented in Chapter 4. The tagging power calculated in this sample is $(2.2 \pm 0.4)\%$

The resolution model used in the 2010 data fit uses three Gaussian with the same mean, the different resolutions are calculated when fitting the prompt background (as explained in Chapter 3), the parameters of the proper time resolution models are presented in Table 5.10. A dilution factor between the prompt and the signal model exists. This leads to a dilution on the oscillation amplitude $\mathcal{D}_{\text{eff}} = 0.68 \pm 0.04\%$ corresponding to an effective decay time resolution of 50 fs. No significant differences exists between the resolution model for the signal and that of the background. This have been checked by comparing the per-event time error for signal and prompt event using sPlots technique to separate signal and background.

Two proper time acceptances are needed to simulate the different proper time deformations caused by two different trigger. We distinguish between the proper time acceptance for events passing the unbiased trigger lines, this acceptance function simulates the inefficiency experienced at high proper time values and explained in Chapter 3. The decay time acceptances applied to the signal component are analogously applied to the background decay time distributions. The second is a non trivial shape of the proper time resolution of the signal events passing the biased trigger lines. For these events, effects appears at low proper time values in the proper time distribution due to cuts on the impact parameter used

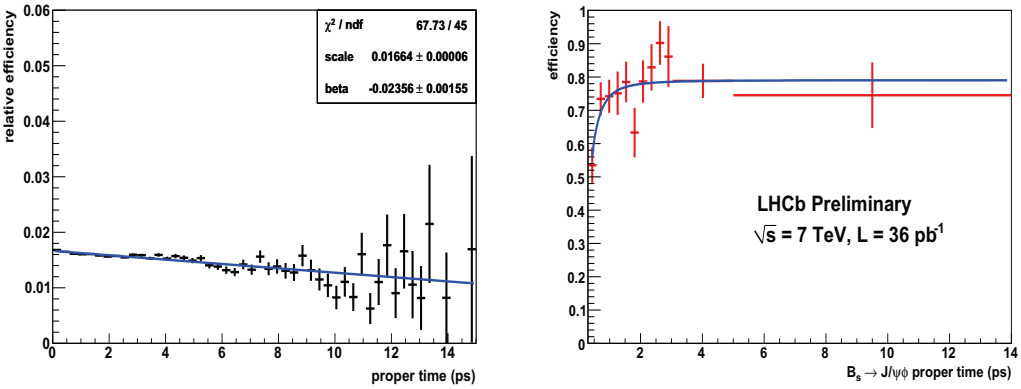

Figure 5.9: Left: proper time acceptance function for events passing the unbiased trigger lines (extracted from Monte Carlo). Right: proper time acceptance function for events passing the biased trigger line (extracted form data using sPlots techniques).

in these trigger lines. The acceptance function accounting for this biased lines is extracted from data using the overlap between the biased and the unbiased triggers. Using sPlots technique the acceptance function is computed by dividing the proper time distribution of the events passing the biased triggers by those passing both biased and unbiased trigger lines, Figure 5.9 shows the resulting acceptance function for events passing the biased trigger. An empirical function is used in order to fit the acceptance histogram:

$$\epsilon(t;a,c) = n\frac{(a\cdot t)^c}{1+(a\cdot t)^c}\,, \tag{5.15}$$

where t denotes proper time, a and c are shape parameters of the model, and n represents an absolute scale which is only needed here for the normalization purpose in the maximum likelihood fit described below. Angular resolution functions is ignored (having a negligible effect on fitted parameters). The angular acceptance corrections are calculated using the Monte Carlo simulation as explained in Chapter 3. The modeling of the 3-D acceptance corrections uses Legendre polynomial.

The background contribution to the 2010 data is small after applying the proper time cut. No peaking background was found in the signal mass region. Similar behavior of angular background distributions is observed between the left side and the right side of the mass distribution. This validate the extraction of the angular distributions of the background from the mass side bands. The angular distributions of the background are de-

scribed using the Legendre polynomial.

Results

Due to the small size of the data sample, a point estimte is not used to quote the ϕ_s value with standard error. Constraits in the ϕ_s in $B_s^0 \to J/\psi\phi$ channel with only 757 events is performed through Feldman and Cousins's prescription [114].

The Figure 5.10 shows the projection of the pdf onto proper time and angular variables on the biased and unbiased 2010 data. The Figure 5.11 shows the 68.3%, 90% and 95% confidence interval contour in the $\phi_s - \Delta\Gamma_s$ plane. This corresponds to a fluctuation from the Standard Model expectation of 21.5% (1.2σ). The symmetry in the plot is due to the two-fold ambiguity explained in Chapter 1

When projecting the confidence level contours onto ϕ_s dimension:

$$\phi_s \in [-2.7, -0.5] \text{ rad at 68\% CL}$$
$$\phi_s \in [-3.5,\ 0.2] \text{ rad at 95\% CL}$$

The systematic errors on the $\phi_s - \Delta\Gamma_s$ confidence is estimated by performing log likelihood scans with different fitting conditions (mass, proper time and background models) and then compared to the contour obtained with the nominal fitting condition. The main systematic sources are:

- Uncertainty in the tagging dilution: statistical and systematic uncertainties in the tagging calibration from the $B^+ \to J/\psi K^+$ channel. The error on the dilution is dominated by the statistical error and leads to a relative 7% on ϕ_s. This systematic error is included in the fit as the tagging calibration parameters are floated with Gaussian constraint for their errors.

- Proper time resolution: the proper time resolution is increased by 10% and results are compared to the nominal fit, the relative systematic error is estimated to be 6%.

- Ignoring the S-wave contribution: The minimal fit does not include the KK S-wave component in the signal pdf. Based on the work in [41], the result of neglecting the 6.7% S-wave [42] is a bias of 11% on ϕ_s value toward zero.

Other sources of systematics like: background description, angular acceptance and mass model are considered also in the study but are found to have a small systematic effect on the fit result [115].

Systematic variations on the $\phi_s - \Delta\Gamma_s$ confidence contours have a negligible effect. The 68% confidence level is practically not affected.

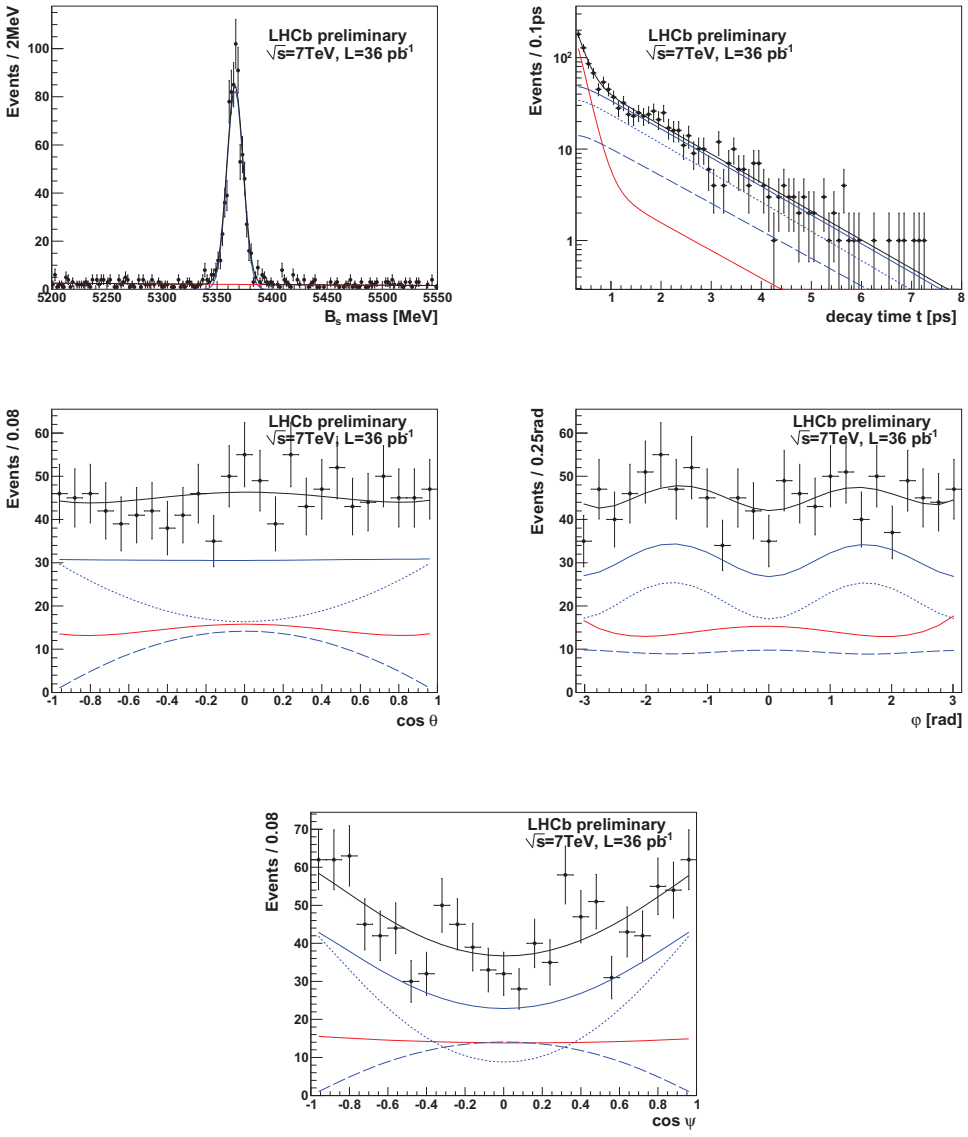

Figure 5.10: Projections for the biased and unbiased data sample after the tagged fit assuming $\phi_s = 0$. The total fit result is represented by the black line. The signal component is represented by the solid blue line; the dashed and dotted blue lines show the *CP*-odd and *CP*-even signal components respectively. The background component is given by the red line [104].

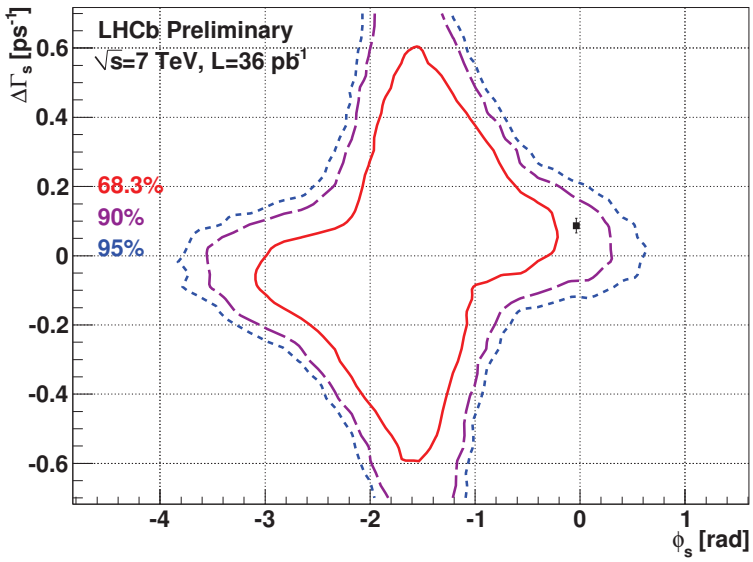

Figure 5.11: Feldman-Cousins confidence regions in the $\phi_s - \Delta\Gamma_s$ plane. The CL at the Standard Model point (blue square) is 0.785 which corresponds to a deviation of 1.2σ. Projected in one dimension, $\phi_s \in [-2.7, -0.5]$ rad at 68% CL [104].

5.5 Summary

In this Chapter we presented a variety of studies of the fit of physics parameters in the $B_s^0 \to J/\psi\phi$ channel, mainly the ϕ_s phase. We developed a fit program that handles the complexities in this channel. We validate this program with full Monte Carlo simulation and toy Monte Carlo.

We determine the sensitivity of the LHCb experiment to the ϕ_s phase. Using unbiased selection performance developed in Chapter 3, the expected statistical uncertainty on ϕ_s after $2\,fb^{-1}$ at 7 TeV is: $\sigma_{\phi_s} = (0.042 \pm 0.002)$ rad with the unbiased selection configuration. The sensitivity with biased selection is significantly higher and it could get up to $\sigma_{\phi_s} = (0.028 \pm 0.002)$ rad. This result depends strongly on assumptions made in this chapter in particular on the trigger efficiency.

In 2010, the integrated luminosity is $\sim 36\,pb^{-1}$ corresponding to 836 $B_s^0 \to J/\psi\phi$ events. Hence a low signal yield was accumulated. The reliability of the likelihood estimator is studied at low signal yield. We find that, under 6 000 signal events, interval confidence must be used for ϕ_s determination instead of the point estimate, a result obtained with the nominal detector performance presented in Chapter 3.

Data accumulation will accelerate in the coming years. The long term strategy for ϕ_s measurement should rely on a biased strategy, where the fit input is taken from a biased selection line and the proper time acceptance and resolution model are extracted from a dedicated unbiased line. We developed a biased scenarios in Chapter 3. One of the extra complications of such selection is the non trivial proper time acceptance. We studied in this Chapter the systematic errors induced by wrong determination of this function. After scanning different scenarios, we find it negligible in most of the cases.

Finally we review the first published ϕ_s analysis [104]. It uses the unbiased selection developed in this thesis and slightly modified fitting program. Tagged and untagged events selected by both biased and unbiased set of trigger lines are the input of the fit. Because of the small number of signal events, the result is presented in a 2D confidence level in the $\phi_s - \Delta\Gamma_s$ plane. The probability of a fluctuation from the Standard Model expectation to the observed result of ϕ_s and $\Delta\Gamma_s$ is 22%. Projected to one dimension:

$$\phi_s \in [-2.7, -0.5] \text{ rad at } 68\% \text{ CL}$$

A thorough study for systematic errors found small systematic effect on the confidence region.

Data accumulation continues with great pace at LHCb. We expected to give a results competitive to those of CDF and D0 very soon.

Chapter 6

Conclusion

LHCb experiment was dedicated to the search for New Physics in CP violation and rare decays in the beauty and charm sectors. The experiment inaugurated end of 2009 and continue data accumulation during 2011.

The ϕ_s phase is a key measurement at LHCb. While the Standard Model predicts an almost vanishing value of ϕ_s with high accuracy, many New Physics models are expecting large values of this phase. The $B_s^0 \rightarrow J/\psi\phi$ channel is considered by far the golden channel for this measurement.

The ϕ_s measurement requires a good proper time resolution in order to resolve the fast $B_s^0 - \overline{B}_s^0$ oscillation, angular analysis to separate statistically the mixed final CP states and a calibrated tagging of the initial B-meson flavour. It is imperative that these challenges are confronted with a robust strategy that provides a reliable measurement during the different data taking phases of the LHC. The steps toward making this measurement are:

- trigger and select the $B_s^0 \rightarrow J/\psi\phi$ candidates;
- measure the proper time of the candidates;
- measure the tranversity angles of the decay products of the candidates;
- tag the initial flavor of the selected B_s^0 in the candidates ;
- fit the phase ϕ_s.

The main concern of our thesis was to contribute to the selection and fit of $B_s^0 \rightarrow J/\psi\phi$ events. In addition, a modest contribution in the flavor tagging was provided. The analysis published in this thesis was performed

on data collected at LHCb during 2010 run at 7 TeV, corresponding to an integrated luminosity of $36\,\mathrm{pb}^{-1}$.

The first part of this work is the development of the selection for the $B_s^0 \to J/\psi\phi$ channel. To minimize the systematic error and simplifying the analysis in its earliest stage, we avoided any bias on proper time distribution and unified the selection among the signal and the control channels. Signal and background properties are studied thoroughly using Monte Carlo full simulation.

With the 2010 data, 570 $B_s^0 \to J/\psi\phi$ candidates pass the proper time "unbiased" selection. The average proper time resolution is 50 fs and the mass resolution of B_s^0 is $7\,\mathrm{MeV}/c^2$.

We developed an alternative selection which increases ϕ_s sensitivity and reduces the bandwidth occupancy caused by prompt background component. Those two objectives are indeed accomplished by using proper time biasing cuts. The downside of this selection is the non-trivial deformation in the proper time distribution. We developed a data driven method in order to determine this deformation and studied the systematic induced by it.

The second part of the thesis tackles the flavor tagging. In particular, the estimation of the tagging performance in the $B_s^0 \to J/\psi\phi$ channel on both Monte Carlo and real data. We obtain an opposite-side tagging power $\epsilon_{\mathrm{eff}} = (2.2 \pm 0.4)\%$ using the 2010 dataset. We also validate the portability of the tagging properties from the control channels to the signal one on 2010 data.

In 2010, the LHC running conditions changed with respect to those of the initial LHCb design. Higher pile-up rate increases the number of tracks and vertexes per event. We observed that the tagging power and signal efficiency tend to decrease with the increase of pile-up in the event, affecting the ϕ_s statistical sensitivity.

The third part of the thesis deals the fit procedure. We construct and test a fitter program to extract the physical parameter in the $B_s^0 \to J/\psi\phi$ channel. Using fast Monte Carlo simulation we estimate the ϕ_s sensitivity with the unbiased and biased selection configuration. We study the systematic error induced by the non-trivial proper time acceptance in the context of the biased selection. All considered cases allude to a negligible systematic error on ϕ_s with $2\,\mathrm{fb}^{-1}$. We studied the effect of low number of signal events on the reliability of the likelihood estimator. We found that the likelihood estimator is only reliable after the accumulation of $\sim 6\,000$ signal events.

We finally summarize the collective effort leading to the first determination of ϕ_s phase at LHCb [104]. The analysis is performed using 2010

data corresponding to $\sim$ 836 signal events, which are selected by both biased and unbiased trigger lines. The tagged time-dependent angular analysis carried out on these samples provides a two-dimensional $\phi_s - \Delta\Gamma_s$ confidence level. The probability of the fluctuation from the Standard Modle to the observed values of ϕ_s and $\Delta\Gamma_s$ is 22% (1.2σ). The projection of the $\phi_s - \Delta\Gamma_s$ confidence level onto ϕ_s dimension gives:

$$\phi_s \in [-2.7, -0.5] \text{ rad at } 68\% \text{ CL} ,$$

Different sources of systematic error are considered: background, proper time resolution, acceptance function mis-modeling. Within the available statistics, systematic error sources are found to be negligible. The LHCb result is not yet competitive with those of CDF and D0. CDF and D0 are scheduled to shut down by the end of September 2011 with total integrated luminosity of $\sim 10\,\text{fb}^{-1}$ each. It is interesting to note that LHCb, CDF and D0 all observe a preferred central value of ϕ_s 1σ away from the Standard Model expectation, in the same direction. Furthermore, hints of New Physics are found in the A_{sl} parameter which is related to the ϕ_s phase. A 3.9σ disagreement with respect to the Standard Model has been reported by D0 [44].

At LHCb, the design instantaneous luminosity was surpassed in May 2011, more data will be accumulated. Flavour tagging performance will soon improve by the inclusion of the same-side kaon tagger. Analysis strategy in the following stage of data taking should move to biased strategy which gives a better sensitivity to ϕ_s. A more refined analysis includes the effects of CP violation in the decay and in the mixing. The fit can also accommodates the production asymmetry between the B_s^0 and $\overline{B}_s^0$ and the different mistag rates between B_s^0 and $\overline{B}_s^0$ tagged events. In addition, ϕ_s sensitivity can be enhanced using other $\overline{b} \to \overline{c}c\overline{s}$ related modes. These aspects, among other developments in reconstruction and detector performance, will increase the sensitivity on ϕ_s parameter. The exploration of the New Physics horizon in the few coming years is closer than ever before.

Epilogue

In 2011, LHCb used $337\,\mathrm{pb}^{-1}$ to publish the most precise estimation on ϕ_s in the $B_s^0 \to J/\psi\phi$ channel.

The selection of the 2011 data stayed mainly unchanged with respect to the one used in 2010. However, a cut was added to remove clone candidates. For the calculation of the angular acceptances, comparisons between the data and Monte Carlo showed a significant difference in the Kaon momentum distributions. This difference leads to an effect on $\Delta\Gamma_s$ and polarization amplitudes. A systematic error has been assigned to account for this effect. The proper time acceptance for the biased events is determined in the fit while the proper time acceptance for the unbiased selection is extracted from Monte Carlo samples. The proper time resolution is found to be 50 fs. The overall tagging performance for the opposite-side taggers is similar to the 2010 one, it is found to be $2.1 \pm 0.4\%$. The same-side kaon tagger was not calibrated, therefore it was not used for the 2011 analysis. One of the novelties of the analysis is the addition of the S-wave component to the likelihood formalism. This helps to remove the two-fold ambiguity over the ϕ_s parameter.

Using 8276 ± 94 $B_s^0 \to J/\psi\phi$ events, the following results are obtained:

$$\begin{aligned} \phi_s &= 0.13 \pm 0.18 \pm 0.07\,\mathrm{rad} \\ \Gamma_s &= 0.656 \pm 0.0009 \pm 0.008\,\mathrm{ps}^{-1} \\ \Delta\Gamma_s &= 0.13 \pm 0.029 \pm 0.011\,\mathrm{ps}^{-1} \end{aligned}$$

A dissimilarity test was performed to asses the overall agreement of the probability density function used with the data. The p-value obtained is 0.44. A comprehensive study for the systematic uncertainties shows that systematic errors are inferior to the statistical ones.

LHCb provided a confidence level estimation for ϕ_s for comparison with the results published by CDF and D0 experiments. Figure 6 shows a superposition of the confidence levels in the $\phi_s - \Delta\Gamma_s$ plane which are obtained from LHCb, CDF and D0. The contour of LHCb favors two regions corresponding to two mirror solutions.

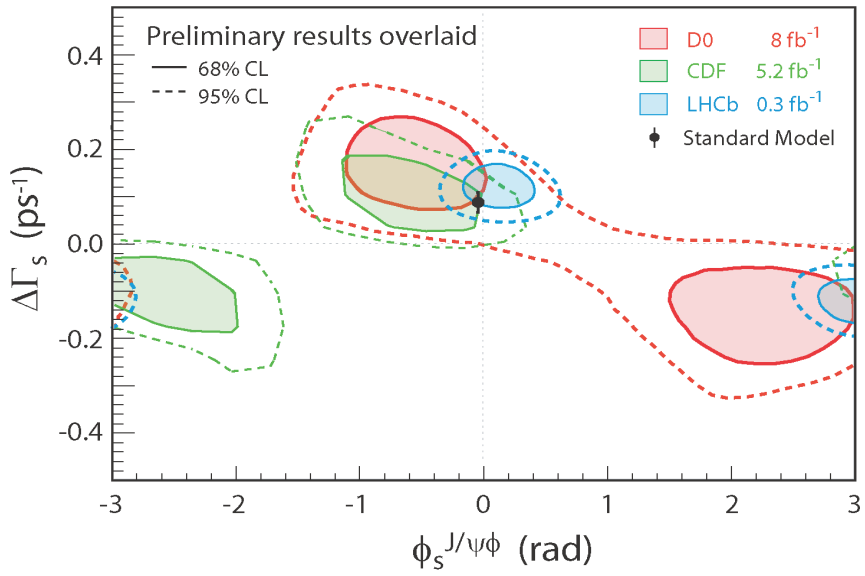

Figure 6.1: Feldman-Cousins confidence regions in the $\phi_s - \Delta\Gamma_s$ plane at LHCb (blue), CDF (green) and D0 (red).

The LHCb measurement is in agreement with the Standard Model expectation. Nonetheless, the shaded area of the LHCb contour implies that there is still a room to account for New Physics effects.

Conclusion

LHCb est dédié à la recherche de la Nouvelle Physique dans la violation de la symmetrie CP et de désintégrations rares dans les secteurs de la beauté et du charme. La prise de données a debuté fin 2009.

La phase ϕ_s est une mesure clé dans LHCb. Le Modèle Standard prédit une valeur quasi-nulle de ϕ_s avec une grande précision, alors que de nombreux modèles de Nouvelle Physique prèdise des valeurs beacoup plus grandes. Le canal $B_s^0 \to J/\psi\phi$ est considéré comme la voie royalle pour effectuer cette mesure.

La mesure de la phase ϕ_s nécessite une bonne résolution temporelle en vue de résoudre l'oscillation $B_s^0\,\overline{B}_s^0$, une analyse angulaire pour séparer statistiquement les états finaux de CP et un étiquetage calibré de la saveur initiale du méson B_s^0. Les étapes de cette mesure sont :

- déclencher et sélectionner les candidats $B_s^0 \to J/\psi\phi$;
- mesure leur temps propre;
- measure leurs variables angulaires;
- étiqueter leur saveure initiale;
- ajuster la phase ϕ_s.

Dans cette thèse, nous avons développé la sélection et l'ajustement des événements $B_s^0 \to J/\psi\phi$. En outre, une modeste contribution dans l'étiquetage des saveurs a été fournie. Nous avons utilisé les données recueillies par LHCb à 7 TeV au cours de l'année 2010, correspondant à une luminosité intégrée de $36\,pb^{-1}$.

La première partie de ce travail a consisté à développer la sélection pour le canal $B_s^0 \to J/\psi\phi$. Afin de minimiser l'erreur systématique et de simplifier l'analyse dans son premier stade, nous avons évité tout biais sur la distribution des temps propre et unifier la sélection entre le signal et les deux canaux de contrôle $B_d^0 \to J/\psi K^{*0}$ et $B^+ \to J/\psi K^+$. Les propriétés

du signal et le bruit du fond ont été étudiées a l'aide d'une simulation Monte-Carlo complète.

Avec les données de 2010, 570 $B_s^0 \to J/\psi\phi$ passent la sélection non-biasée. La résolution temporelle moyenne est de 50 fs et la résolution de masse de B_s^0 est de 7 MeV/c^2.

Nous avons développé une sélection alternative qui augmente la sensibilité sur ϕ_s et réduit le taux d'occupation de la bande passante causée par le bruit du fond à temps de vie nul. Ces deux objectifs sont accompli en utilisant des coupures qui déforme de façon non triviale de la distribution en temps propre. Nous avons développé une méthode utilisante les données réelles afin de déterminer cette déformation et d'étudié les effets systématiques.

La deuxième partie de la thèse aborde l'étiquetage de saveur. En particulier, l'estimation de la performance d'étiquetage dans le canal $B_s^0 \to J/\psi\phi$ sur les données Monte-Carlo et les données réelles. Nous obtenons une puissance d'étiquetage $\epsilon_{\text{eff}} = (2,2 \pm 0,4)\%$. Nous avons également validé la portabilité d'étiquetage des canaux de contrôle à celle du signal.

En 2010, les conditions de prise de donnée en LHC ont changé par rapport à celles pévue au moment de la conception de LHCb. Le taux supérieur d'empilement proton-proton augmente le nombre de vertexes pimaires et de traces reconstruites par événement. Nous avons observé que la puissance d'étiquetage du signal diminue avec l'augmentation du taux d'empilement, affectant la sensibilité statistique de la phase ϕ_s.

La troisième partie de cette thèse traite de la procédure d'ajustement. Nous construisons et testons un programme d'ajustement pour extraire les paramètres physiques dans le canal $B_s^0 \to J/\psi\phi$. A l'aide de simulation Monte-Carlo rapides, nous estimons la sensibilité sur ϕ_s avec les configurations de la sélections non-biaisées et biaisées. Nous étudions l'erreur systématique induite par l'acceptance non-triviale du temps dans le contexte de la sélection biaisée. Nous avons étudié l'effet du faible nombre d'événements de signal sur la fiabilité de l'estimateur de vraisemblance. Nous avons constaté que l'estimateur est fiable seulement après l'accumulation de $\sim 6\,000$ événements de signal.

Nous avons finalement résumé l'effort collectif menant à la première détermination de la phase ϕ_s dans LHCb [104]. L'analyse est effectuée en utilisant les données 2010, correspondant à ~ 836 événements de signal, qui sont selectionnés par les deux lignes de déclenchement biaisée et non-biaisée. L'analyse angulaire dependante du temps réalisée sur ces échantillons fournit un niveau de confiance à deux dimensions dans le plan $\phi_s - \Delta\Gamma$. La probabilité d'une fluctuation des valeurs de ϕ_s, $\Delta\Gamma$ du Modèle Standard à celles observées dans les données est de 22%$(1,2\sigma)$,

$$\phi_s \in [-2.7, -0.5]\,\text{rad}\ \ 68\%\,\text{CL}.$$

Des différentes sources d'erreurs systématiques considérées sont: le bruit du fond, la résolution en temps propre, la modélisation de fonction d'acceptance. Au vue de l'erreur statistique actuelle, les erreurs systématiques sont négligeables. Avec la statistiques de 2010, le résultat de LHCb n'est pas encore concurrentiels avec celui du CDF et D0.

CDF et D0 arrêteront definitivement leur prise de données la fin de Septembre 2011 avec une luminosité intégrée totale de $\sim 10\,\text{fb}^{-1}$ pour chacune des experiences. Il est intéressant de noter que LHCb, CDF et D0 observent tous une valeur central de ϕ_s à -1σ de la valeur attendue dans le Modèle Standard, dans la même direction. Par ailleurs, D0 observe une deviation de 3.9σ par rapport au Modèle Standard dans la mesure de A_{sl}, paramètre sensible à la même phase de Nouvelle Physique que ϕ_s.

À LHCb, la luminosité instantanée de conception a été dépassé en mai 2011 et la prise de données continue. La performances d'étiquetage des saveurs seront bientôt améliorées par l'inclusion du kaon accomponiant le signal. La future analyse de ϕ_s utilise de plus en plus la stratégie biaisée. Une analyse plus fine pour comprende les effets de la violation de CP dans la désintégration et dans le mélange se développe. L'ajustement tiendra compte également de l'asymétrie de production entre les B_s^0 et $\overline{B}_s^0$ et la fraction de mauvaise étiquetage différentes entre B_s^0 et $\overline{B}_s^0$. De plus, la sensibilité sur ϕ_s sera améliorée en utilisant d'autres mode de transistions $\overline{b} \to \bar{c}c\bar{s}$. Ces aspects, parmi d'autres développements dans les performances de reconstruction et du détecteur, augmenteront la sensibilité sur le paramètre ϕ_s. L'exploration de la Nouvelle Physique dans les quelques années à venir est plus proche que jamais.

Chapter 7

List of publications

LHCb internal note :

1. E. Maurice, O. Leroy, B. Khanji and S. Poss, "Study of angular acceptance in $B_s^0 \to J/\psi\phi$", CERN-LHCb-INT-2009-031" (2009).

2. R. Aaij et al, "b-hadron lifetimes measurement with exclusive $b \to J/\psi X$ decays reconstructed in the 2010 data", LHCb-ANA-001-2011, (2011).

3. T.Brambach et al, "Optimization and calibration of the LHCb tagging performance using 2010 data", LHCb-ANA-003-2011, (2011).

4. K. Akiba et al, "Measurement of ΔM_d and calibration of the combined opposite side taggers in the decay $B_d \to D^-(K^+\pi^-\pi^-)\pi^+$" , LHCb-ANA-2011-010. (2011).

5. T.Brambach et al, "Search of CP violation in $B_d \to J/\psi K_S$ decay with first LHCb data", LHCb-ANA-004-2011, (2011).

6. K. Akiba et al, "Measurement of ΔM_s in the decay $B_s \to D_s^-(K^+K^-\pi^-)(3)\pi$", LHCb-ANA-005-2011, (2011).

7. R. Aaij et al, "Measurement of CP violating parameters in the tagged time-dependent angular analysis of $B_s \to J/\psi\phi$ decays with the 2010 data sample", LHCb-ANA-006-2011, (2011).

Public notes :

1. M. Calvi and B. Khanji and G. Lanfranchi and O. Leroy and S. Poss, "Lifetime Unbiased Selection of $B_s \to J/\psi\phi$ and related control channels: $B_d \to J/\psi K*$ and $B^+ \to J/\psi K+$", CERN-LHCb-2009-025, (2009).

2. B. Adeva, et al. "Roadmap for selected key measurements of LHCb", LHCb-PUB-2009-029, (2009).

3. The LHCb Collaboration, R. Aaij et al, "b-hadron lifetimes measurement with exclusive $b \to J/\psi X$ decays reconstructed in the 2010 data", LHCb-CONF-001-2011, (2011).

4. The LHCb Collaboration, R. Aaij et al, "Optimization and caliberation of the LHCb tagging performance using 2010 data", LHCb-CONF-003-2011, (2011).

5. The LHCb Collaboration, R. Aaij et al, "search of CP violation in $B_d \to J/\psi K_S$ decay with first LHCb data", LHCb-CONF-004-2011, (2011).

6. The LHCb Collaboration, R. Aaij et al, "Measuremnt of ΔM_s in the decay $B_s^- \to D_s^-(K^+K^-\pi^-)(3)\pi$", LHCb-CONF-005-2011, (2011).

7. The LHCb Collaboration, R. Aaij et al, "Measurement of CP violating parameters in the tagged time-dependent angular analysis of $B_s \to J/\psi\phi$ decaysdecays with the 2010 data sample", LHCb-CONF-006-2011, (2011).

8. The LHCb Collaboration, Measurement of ΔM_d and calibration of the combined opposite side taggers in the decay $B_d^0 \to D^-(K^+\pi^-\pi^-)\pi^+$, LHCb-CONF-2011-010. (2010).

9. The LHCb Collaboration, R. Aaij et al, " First observation of $\bar{B_s^0} \to D_{s2}^{*+} X\mu^-\bar{\nu}$ decays", Physics Letters B 698, 14-20, (2011).

10. The LHCb Collaboration, R. Aaij et al, "First observation of $B_s^0 \to J/\psi f_0(980)$ decays", Physics Letters B 698, 115-122, (2011).

11. The LHCb Collaboration, R. Aaij et al, "Measurement of J/ψ production in pp collisions at $\sqrt{s} = 7\,\text{TeV}$", Eur.Phys.J.C71, 1645, (2011).

12. The LHCb Collaboration, R. Aaij et al, "Search for the rare decays $B_s^0 \to \mu^+\mu^-$ and $B^0 \to \mu^+\mu^-$ ", Physics Letters B 699, 330-340, (2011).

13. The LHCb Collaboration, R. Aaij et al, "Prompt K_S^0 production in pp collisions at $\sqrt{s} = 0.9\,\text{TeV}$", Physics Letters B 693, 69 (2010).

14. The LHCb Collaboration, R. Aaij et al, "Measurement of $\sigma(pp \to b\bar{b}X)$ at $\sqrt{s} = 7\,\text{TeV}$ in the forward region", Physics Letters B 694 (2010) 209.

15. The LHCb Collaboration, B. Adeva et al, "Roadmap for selected key measurements of LHCb", arXiv:0912.4179v2 [hep-ex], (2009).

16. The LHCb Collaboration, A. A. Alves Jr. et al, "The LHCb Detector at the LHC", 2008 JINST 3 S08005 (2008).

Conference note :

1. B. Khanji, "Prospects of CP violation in $B_s \to J/\psi\phi$ channel with first LHCb data", PoS(Kruger 2010)040, Workshop on discovery physics at LHC, Kruger National Park, Mpumalanga, South Africa, (2010).

Bibliography

[1] The CDF Collaboration, "An Updated Measurement of the CP Violating Phase β_s in the $B_s \to J/\psi\phi$ Decays using 5.2 fb^{-1} of Integrated Luminosity", public note CDF/ANAL/BOTTOM/PUBLIC/10206 (2010).

[2] The D0 Collaboration, D0 Conference Note 6098-CONF, July 2010, Updated Measurement of the CP-Violating Phase ϕ_s Using the Flavor-tagged Decay $B_s \to J/\psi\phi$ decays, (2010).

[3] G. C. Branco, L. Lavoura, and J. P. Silva. CP violation. International series of monographs on physics. Oxford universoty press (1999).

[4] M. Beyere et al. CP violation in particle, nuclear and astrophysics. Proceedings, Summer School, Preow, Germaney, Octobre 1-8 2000 (2000).

[5] B. Adeva, et al. "Roadmap for selected key measurements of LHCb", LHCb-PUB-2009-029, (2009).

[6] A. D. Sakharov, Pisma Zh. Eksp. Teor. Fiz. 5:32 (1967).

[7] C. S. Wu, et al, Experimental test of parity consrevation in beta decay, phys. Rev., 105:1413-1414, (1975).

[8] J. H. Christenson et al, Phys., Rev., Lett., 13 (1964).

[9] M. Kobayashi and T. Maskawa. CP-violation in the normalizable theory of weak interaction. Prog. Theor. Phys., 49: 652-657, (1973).

[10] N. Cabibo, "Unitary symmetry and leptonic decays", Phys. Rev. Lett., 10:531-532, (1963).

[11] S. L. Glashow, J. Iliopoulos and L. Maiani, Phys. Rev. D2 (1970) 1285.

[12] V. Fanti et al. (1999). "A new measurement of direct CP violation in two pion decays of the neutral kaon". Physics Letters B 465(1-4):335-348, (1999).

[13] BaBar Collaboration : B. Aubert et al, "observation of CP violation in the B^0_d meson system". Phys. Rev. Lett., 87:91801, (2001).

[14] Belle Collaboration : K. Abe et al. "observation of large CP violation in the neutral B meson system". Phys. Rev. Lett., 87:91802, (2001).

[15] C. Jarlksog. "Commutator of the quark mass matrices in the Standard Model electroweak model and a measure of maximal CP nonconservation". Phys. Rev. Lett., 55:1039, (1985).

[16] C. Jarlksog. "A basis independent formulation of the conection between quark mass matrices, CP violation and experiment". Zeitschrift fur Physics, C66:491, (1985).

[17] K. Nakamura et al. (Particle Data Group), J. Phys. G 37, 075021 (2010).

[18] L. Wolfenstein, Phys. Rev. Lett., 51, (1983).

[19] V. F. Weisskopdf and E. P. Wigner, "Calculation of the brightness of spectral lines on the basis od Dirac theory". Z. Phys., 63:45-73, (1930).

[20] G. Lüders. "On the Equivalence of Invariance under Time Reversal and under Particle-Antiparticle Conjugation for Relativistic Field Theories", Dan. Mat. Phys. Medd., 28:5, (1954).

[21] R. Fleischer, "Flavour physics and CP violation", hep-ph/0405091, (2004).

[22] A. Lenz et al, "Anatomy of New Physics in B-Bbar mixing", arXiv:1008.1593v3 [hep-ph], (2011).

[23] R. Fleischer, "Extracting from $B_{s(d)} \to J/\psi K^0_S$ and $B_{d(s)} \to D^+_{d(s)} D^-_{d(s)}$" , Eur. Phys. J. C 10, 299-306 (1999).

[24] H. Boos, T. Mannel and J. Reuter, "The gold-plated mode revisited: $\sin(2\beta)$ and $B_{s(d)} \to J/\psi K^0_S$ in the Standard Model", Phys. Rev. D 70, 036006 (2004); H. N. Li and S. Mishima, "Penguin pollution in the $B_{s(d)} \to J/\psi K^0_S$ decay", JHEP 0703, 009 (2007).

[25] H. Boos et al. "The Effect of Penguins in the $B_d \to J/\psi K^0_S$ CP asymmetry", Phys, Rev, D70, 0036006, (2004).

[26] S. Faller et al. arxiv:0810.4248v1.

[27] The CDF collaboration, "Observation of new supressed B_s decays and measurement of their branching ratio", CDF Note 10240, (2010).

[28] The LHCb Collaboration, "Evidence for the decay $B_s \rightarrow J/\psi \bar{K}^{*0}$", LHCb-CONF-025-2011, (2011).

[29] A. J. Lenz, A simple relation for B_s mixing, arXiv:1106.3200v2 (2011).

[30] Brook, N et al, "LHCb's Potential to Measure Flavour-Specific CP-Asymmetry in Semileptonic and hadronic B_s^0 Decays", CERN, LHCb-2007-054. CERN-LHCb-2007-054, (2008).

[31] The D0 Collaboration, V. Abazov, et al, "Measurement of the anomalous like-sign dimuon charge asymmetry with 9 fb^{-1} of $p\bar{p}$ collisions", arXiv:1106.6308v1, (2011).

[32] A. Digger *et al.*, "Angular distribution and lifetime difference in $B_s \rightarrow J/\psi\phi$ decays", arxiv:hep-Ph/951136v1, (1995).

[33] C. G Branco and L. Lavoura. "Wolfenstien-type parametrization of the quark mixing matrix" . Phys. Rev. D., 38:2295, (1988).

[34] CKMfitter group, J. Charles *et al.*, Eur. Phys. J. C41, 1-131 (2005).

[35] Official web page of the CKM fitter groupe : `http://ckmfitter.in2p3.fr/`

[36] A. Abulencia et al. [CDF collaboration], Phys. Rev. Lett. 97, 242003, arxiv:hep-ex/0609040. (2006).

[37] A. Dighe et al., "Angular distribution and lifetime dierence in $B_s \rightarrow J/\psi\phi$ decays", Phys. Lett. B 369, 144 (1996).

[38] S. Stone and L. Zhang, S-waves and the Measurement of CP Violating Phases in Bs Decays, Phys. Rev. D 79 (2009) 074024 [arXiv:0812.2832].

[39] E. Barberio et al. [Heavy Flavour Averaging Group], arxiv:0808.1297 [hep-ex] and online update at `http://www.slac.stanford.edu/xorg/hfag`, updated PDG 2009.

[40] S. Faller, R. Fleischer and T. Mannel, "Precision physics with $B_s \rightarrow J/\psi\phi$ at the LHC: The quest for New Physics", arXiv:0810.4248v1 [hep-ph] (2008).

[41] Y. Xie et al, "Determination of $2\beta_s$ in $B_s \to J/\psi K^+K^-$ Decays in the Presence of a K^+K^- S-Wave Contribution", arXiv:0908.3627 (2009).

[42] The CDF Collaboration, public note `CDF/ANAL/BOTTOM/PUBLIC/10206` (2010).

[43] F. Azfar et al. " Formulae for the Analysis of the Flavor-Tagged Decay $B_s \to J/\psi\phi$" JHEP 1011, 158. (2010).

[44] V. M. Abazov et al. (D0 Collaboration), Evidence for an Anomalous Like-Sign Dimuon Charge Asymmetry, arXiv.org:1005.2757, accepted for publication in Phys. Rev. D.

[45] V. M. Abazov et al. (D0 Collaboration) Phys. Rev. Lett. 102, 091801 [arXiv.org:0811.2173], (2009).

[46] The D0 Collaboration, Combined D0 Measurements Constraining the CP-violating Phase and Width Difference in the B_s^0 System ,D0 Conference note 6098-CONF, arXiv:hep-ex/0702030v1, (2010).

[47] R. Lambert and F. Muheim, "LHCb Hybrid Photon Detectors and Sensitivity to Flavour Specific Asymmetry in Neutral B-Meson Mixing", Edinburgh U., oai:cds.cern.ch:1154988 (2009).

[48] S. Stone, M. Artuso, and Z. Liming, "Measuring the semileptonic CP asymmetry A_{sl} using a time integrated method", LHCb-INT-2011-016. CERN-LHCb-INT-2011-016, (2011).

[49] The CDF collaboration, Angular analysis of $B_s \to J/\psi\phi$ and $B_d \to J/\psi K^*$ decays and measurement of $\Delta\Gamma_s$ and ϕ_s, CDF note 8950 (2007).

[50] The D0 collaboration, Measurement of the angular and lifetime parameters of the decays $B_d \to J/\psi K^*$ and $B_s \to J/\psi\phi$, Phys. Rev. Lett. 102, 032001 (2009).

[51] The LHCb Collaboration, "Measurement of Δm_d and calibration of the combined opposite side taggers in the decay $B_d^0 \to D^-(K^+\pi^-\pi^-)\pi^+$, LHCb-CONF-2011-010. (2010).

[52] The LHCb Collaboration , Measurement of CP violation in the time-dependent analysis of $B_d^0 \to J/\psi K_S^0$ decays with the 2010 data, LHCb-CONF-2011-004 (2010).

[53] The LHCb Collaboration, Measurement of Δm_s in the decay $B_s^0 \to D_s(K^+K^-\pi^-)\pi^+$ and $B_s^0 \to D_s(K^+K^-\pi^-)\pi^+\pi^+\pi^-$, LHCb-CONF-2011-005. (2011).

[54] The LHCb Collaboration, First observation of $B_s^0 \to J/\psi f_0(980)$ decays, arXiv:1102.0206v2, CERN-PH-EP-2011-008. (2011).

[55] The LHCb Collaboration, First observation of the decay $B_s^0 \to K^*\bar{K}^*$, LHCb-CONF-019-2011, (2011).

[56] T. Sjostrand, L. Lonnblad, S. Marenna, and P. Skands. Pythia 6.3 physics and annual. (2003) .

[57] LHCb collaboration. LHCb VELO Technical Design Report. CERN-LHCC-2001-011, 2001.

[58] LHCb collaboration, Vertex locator technical design report, CERN-LHCC-2001-011 (2001).

[59] LHCb collaboration, S. Amato et al., "LHCb magnet technical design report", CERN-LHCC-2000-007, (2000).

[60] J. Gassner, M. Needham and O. Steinkamp, "Layout and expected performance of the LHCb TT station", Note LHCb-2003-140 (2003).

[61] LHCb collaboration, P. R. Barbosa-Marinho et al., LHCb inner tracker technical design report, CERN-LHCC-2002-029 (2002).

[62] LHCb collaboration, P. R. Barbosa-Marinho et al., Outer tracker technical design report, CERN-LHCC-2001-024 (2001).

[63] Web page for the BRUNEL reconstruction project, `http://lhcb-release-area.web.cern.ch/LHCb-release-area/DOC/brunel/`.

[64] J. V. Tilburg, "Matching VELO tracks with seeding tracks", Note LHCb-2001-103, `http://cdsweb.cern.ch/record/691686`, (2001).

[65] R. Forty, "Track seeding", Note LHCb-2001-109, `http://cdsweb.cern.ch/record/691473`, (2001).

[66] R. Hierck, "Track following in LHCb", Note LHCb-2001-112, `http://cdsweb.cern.ch/record/691752`, (2001).

[67] E. Rodrigues, The LHCb track Kalman fit, Note LHCb-2007-014, (2007).

[68] https://lhcb-phys.web.cern.ch/lhcb-phys/Data_2010/default.htm.

[69] P. Cherenkov, Phys.Rev. 52 (1937), 378.

[70] S. Amato et al, "LHCb Rich", Technical design report, LHCC-2000-037 (2000).

[71] S. Amato et al, "LHCb Calorimeter", Technical design report, LHCC-2000-036 (2000).

[72] S. Amato et al, "LHCb Muon system", Technical design report, LHCC-2001-010 (2001).

[73] R. Forty and O. Schneider, RICH pattern recognition, Note LHCb-98-040, http://cdsweb.cern.ch/record/684714. (1998).

[74] S. Amato et al, "LHCb Trigger system", Technical design report, LHCC-2003-010 (2003).

[75] LHCb twiki page describing the MC10 data samples, https://twiki.cern.ch/twiki/bin/view/LHCbPhysics/BetasWGMonteCarloMC10.

[76] LHCb link to DaVinci related class: "BackgroundCategory", http://lhcb-release-area.web.cern.ch/LHCb-release-area/DOC/davinci/releases/latest/doxygen/db/d23/class_background_category.html

[77] D. J. Lange. "The EvtGen particle decay simulation package", Nucl.Instr.Meth., A(2001)462.

[78] C. Amsler et al. Review of particle physics, Phys. Lett.B 667(2009).

[79] P. Koppenburg, "Dealing with Multiple Candidates", CERN-LHCb-INT-2011-009, (2011).

[80] O. Callot and S. Hansmann-Menzemer, "The forward tracking, Algorithm and performance studies", Tech. Rep. LHCb-2007-015. CERN-LHCb-2007-015, CERN, Geneva, May, 2007.

[81] X. C. Vidal et al. A Muon Identification procedure for LHCb with Kalman Filter, LHCb-INT-2010-052 (LHCb internal note).

[82] M. Calvi, et al. "Lifetime Unbiased Selection of $B_s \to J/\psi\phi$ and related control channels: $B_d \to J/\psi K^*$ and $B^+ \to J/\psi K^+$",CERN , Geneva,LHCb-2009-025. CERN-LHCb-2009-025, May 2009.

[83] S. Poss, and R. Le Gac, Etalonnage de l'algorithme de l'étiquetage par la mesure de sin(2β) dans LHCb. Marseille, Université d'Aix - Marseille II. (2009).

[84] M. Needham, "Identification of Ghost Tracks using a Likelihood Method", LHCb-2008-026. CERN-LHCb-2008-026. LPHE-2008-004.(May 2008).

[85] E. Maurice, et al. "Study of angular acceptance in $B_s^0 \to J/\psi\phi$", CERN-LHCb-INT-2009-031, Dec 2009.

[86] The LHCb Collaboration, "b-hadron lifetimes measurement with exclusive $b \to J/\psi X$ decays reconstructed in the 2010 data", LHCb-CONF-001-2011, (2011).

[87] Twiki page explains the PVRefit algorithm. `https://twiki.cern.ch/twiki/bin/view/LHCb/RefitPV`

[88] The LHCb Collaboration, R. Aaij et al, "Measurement of sigma($pp \to b\bar{b}$ X) at $\sqrt(s) = 7$ TeV in the forward region",Physics Letters B 694 (2010) 209.

[89] P. Avery, "Applied Fitting Theory VI Formulas for Kinematic Fitting", `http://www.phys.ufl.edu/~avery/fitting/kinematic.pdf`.

[90] Twiki page describing DecayTreeFitter, `https://twiki.cern.ch/twiki/bin/view/LHCb/DecayTreeFitter`.

[91] Private communication with Tomas Ruf and Yuehong Xie.

[92] E. Rodrigues, "Dealing with clones in the tracking", LHCb-2006-057. CERN-LHCb-2006-057,(2006).

[93] Private communication with Wouter Hulsbergen.

[94] Web page for DaVinci project, `http://lhcb-release-area.web.cern.ch/LHCb-release-area/DOC/davinci/`.

[95] Y. Xie, "Review and optimization of $B_s \to J/\psi$X event selection",`https://indico.cern.ch/getFile.py/access?contribId=1&resId=1&materialId=slides&confId=110968` (2010).

[96] K. Nakamura et al. (Particle Data Group), Review of particle physics", J. Phys. G124 37, 075021 (2010).

[97] The LHCb Collaboration, "b-hadron lifetimes measurement with exclusive $b \to J/\psi X$ decays reconstructed in the 2010 data", LHCb-ANA-001-2011, (2011).

[98] B. Khanji and O. Leroy, "Status of Biased Selection for $B_s \to J/\psi\phi$", https://indico.cern.ch/getFile.py/access?contribId=9&resId=0&materialId=slides&confId=61342. (2009).

[99] T. du Pree, and M. H. M. Merk, and G. H. Raven,"Search for a Strange Phase in Beautiful Oscillations", Amsterdam, Vrije Universiteit, Amsterdam 2010.

[100] M. Pivk, F. R. Le Diberder. "sPlot: a statistical tool to unfold data distributions", arXiv:physics/0402083v3, Nucl, Instrum, Meth., Vol. A555 , pp. 356-369.(2005).

[101] The LHCb Collaboration, "Optimization and caliberation of the LHCb tagging performance using 2010 data", LHCb-CONF-003-2011, (2011).

[102] M. Calvi et al., "Flavour Tagging Algorithms and Performances in LHCb", LHCb note 2007-058, (2007).

[103] M. Calvi, M. Grabalosa, M. Musy, "Combination of same-side with opposite-side flavour tagging", LHCb-PUB-2009-027.

[104] The LHCb Collaboration, "Measurement of CP violating parameters in the tagged time-dependent angular analysis of $B_s \to J/\psi\phi$ decays-decays with the 2010 data sample", LHCb-CONF-006-2011, (2011).

[105] T. Du Pree and G. Raven, "Methods for Angular Analyses of $B \to J/\psi X$", LHCb-2009-024, CERN-LHCb-2009-024, (2009).

[106] G. Conti and T. Nakada, "LHCb detector momentum calibration with the first year data and a performance study of CP violation measurement with the $B_s^0 \to J/\psi\phi$ decays", Lausanne, EPFL (2010).

[107] C. Langenbruch *et al.*, "An unbinned likelihood fit for the measurement of ϕ_s in the decay $B_s \to J/\psi\phi$", LHCb-PUB-2009-028 (2009).

[108] Y. Xie et al, "Data-driven correction of angular acceptance in the analysis of the decay $B_s^0 \to J/\psi\phi$", LHCb-INT-2010-025. CERN-LHCb-INT-2010-025, (2010).

[109] R. Brun, F. Rademakers et al., "ROOT An Object Oriented Data Analysis Framework", Proceedings AIHENP, vol. 96, pp. 81-86, (1997). Root analysis programe web page : `http://root.cern.ch/drupal/`.

[110] D. Kirkby and W. Verkeke, "The RooFit Toolkit for Data Modeling", arXiv:physics/0306116v1 (2003). RootFit analysis programe web page : `http://root.cern.ch/drupal/content/roofit`.

[111] F. James et al., "MINUIT Function Minimization and Error Analysis", CERN Program Library Long Writeup D, vol. 506, (1998). Reference to documentation page on Minuit fitting program : `http://lcgapp.cern.ch/project/cls/work-packages/mathlibs/minuit/`.

[112] P. Clarke, C. McLean and O. Oliveros," A Sensitivity studies to betas and $\Delta\Gamma_s$ using the full $B_s \rightarrow J/\psi\phi$ angular analysis at the LHCb", CERN Geneva,LHCb-2007-101, CERN-LHCb-2007-101 (2007).

[113] S. Vecchi et al., "Systematic studies on the B_s proper time measurement for the determination of the mixing phase ϕ_s in the channel $B_s \rightarrow J/\psi\phi$", LHCb-PUB-2009-021 (2009).

[114] G. J. Feldman, R.D. Cousins, A Unified Approach to the Classical Statistical Analysis of Small Signals, Phys. Rev. D 57, 3873-3889(1998).

[115] The LHCb Collaboration,"Measurement of CP violating parameters in the tagged time-dependent angular analysis of $B_s \rightarrow J/\psi\phi$ decays with the 2010 data sample", LHCb-ANA-006-2011, (2011).

Recherche de nouvelle physique dans le canal $B_s^0 \to J/\psi\phi$ auprès de l'expérience LHCb

Dans le Modèle Standard, la différence de phase apparaissant dans la désintégration $B_s^0 \to J/\psi\phi$ est prèdite avec une grande précision. Cette observable est une sonde pour mettre en évidence de la Nouvelle Physique car l'oscillation B_s^0-$\overline{B}_s^0$ s'effectue via un diagramme en boucles sensible à la nouvelles particules. Nous avons développé une sélection simplifiée pour les données de 2010. Elle évite tous biais sur la distribution en temps propre afin de réduire l'incertitude systématique. De plus, nous contrôlons les performances d'étiquetage pour les événements $B_s^0 \to J/\psi\phi$ en utilisant les canaux similaires $B_d^0 \to J/\psi K^{*0}$ et $B^+ \to J/\psi K^+$. Avec les données de 2010, nous obtenons 570 événements de signal avec une luminosité intégré de $36\,pb^{-1}$, une puissance de d'étiquetage de $(2,2 \pm 0,4)\%$ et une résolution temporelle de 50 fs. Nous avons étudié une sélection alternative, qui maximise la sensibilité à la phase ϕ_s en utilisant des coupures biasant le temp propre. Nous avons proposé une méthode pour corriger la déformation de temps propre à partir des données. Nous avons développé un programme d'ajustement pour déterminer la phase ϕ_s. Avec les données 2010, la valeur touveé est $\phi_s \in [-2,7, -0,5]$ rad à 68% de confiance. Ce résultat est compatible avec la prédiction du Modèle Standard.

Mots-clés: la violation de CP, le mélange B_s^0-$\overline{B}_s^0$, LHCb, le canal $B_s^0 \to J/\psi\phi$, ϕ_s, l'estimateur maximum de vraisemblance.

Search for New Physics in the $B_s^0 \to J/\psi\phi$ decay channel at LHCb

In the $B_s^0 \to J/\psi\phi$ channel, the phase ϕ_s is predicted to be significantly small in the Standard Model. This observable is an excellent probe for New Physics because the B_s^0-$\overline{B}_s^0$ mixing takes place via a loop diagram where new particles is expected to intervene. These two reasons makes the ϕ_s parameter an excellent probe for New Physics processes. We developed a simplified selection for the 2010 data. It avoids any bias on the proper time distribution in order to reduce systematic uncertainty. In addition, we control the tagging performance for $B_s^0 \to J/\psi\phi$ events using the similar $B_d^0 \to J/\psi K^{*0}$ and $B^+ \to J/\psi K^+$ channels. With the 2010 data, we obtain 570 signal events in $36\,pb^{-1}$ of integrated luminosity, a tagging power of $(2.2 \pm 0.4)\%$ and a proper time resolution of 50 fs. We investigated an alternative selection which maximizes the ϕ_s sensitivity using a proper time biasing cuts. We proposed a data-driven method to correct the proper time acceptance. We designed a fitting program to determine the ϕ_s phase. With the 2010 data, It is found to be: $\phi_s \in [-2.7, -0.5]$ rad at 68% of confidance. This result is compatible with the Standard Model prediction.

Keywords: CP violation, B_s^0-$\overline{B}_s^0$ Mixing, LHCb, $B_s^0 \to J/\psi\phi$, ϕ_s, Likelihood fit.